



UNIVERSITY OF LEEDS

Fast Frequency Containment in Power Systems with Volatile Inertia



Jesus Sanchez Cortes

The University of Leeds

School of Electronic and Electrical Engineering

Submitted in accordance with the requirements for the degree of

Doctor of Philosophy

December, 2023

To my beloved parents and siblings,

*I feel incredibly fortunate and blessed for having you in my life. I
appreciate and love you more than words can express.*

Life is so brief and time is a thief when you are undecided.

–Rod Stewart

Intellectual Property Statement

The candidate confirms that the work submitted is their own, except where work which has formed part of jointly authored publications has been included. The contribution of the candidate and the other authors to this work has been explicitly indicated below. The candidate confirms that appropriate credit has been given within the thesis where reference has been made to the work of others.

The work in Chapter 3 of the thesis has appeared in the following publication:

1. **J. Sánchez Cortés**, M. Rezaei Jegarluei, P. Aristidou, K. Li, and S. Azizi, “Size/location estimation for loss of generation events in power systems with high penetration of renewables,” *Electric Power Systems Research*, vol. 219, 2023.
J. Sánchez Cortés: Conceptualisation, Methodology, Writing-original draft.
M. Rezaei Jegarluei: Software, Validation, Data curation.
P. Aristidou: Resources, Investigation, Validation.
K. Li: Resources, Writing-review and editing.
S. Azizi: Conceptualisation, Supervision, Formal analysis, Validation, Writing-review and editing.

The work in Chapter 4 of the thesis has appeared in the following publications:

1. **J. Sánchez Cortés**, M. Rezaei Jegarluei, and S. Azizi, “Targeted fast frequency response by decomposing frequency into transient and steady-state deviations,” *2023 International Conference on Energy Technologies for Future Grids (IEEE ETFG)*, Wollongong, Australia, 2023.

J. Sánchez Cortés: Conceptualisation, Methodology, Software, Data curation, Writing-original draft.

M. Rezaei Jegarluei: Conceptualisation, Validation, Writing-review and editing.

S. Azizi: Conceptualisation, Supervision, Formal analysis, Validation, Writing-review and editing.

2. **J. Sánchez Cortés**, M. Rezaei Jegarluei, and S. Azizi, “Optimal frequency containment in power systems with volatile inertia: The future is now with a new paradigm,” To be submitted to *IEEE Transactions in Industry Applications*, 2023.

J. Sánchez Cortés: Conceptualisation, Methodology, Software, Data curation, Writing-original draft.

M. Rezaei Jegarluei: Conceptualisation, Validation, Writing-review and editing.

S. Azizi: Conceptualisation, Supervision, Formal analysis, Validation, Writing-review and editing.

This copy has been supplied on the understanding that it is copyright material and that no quotation from the thesis may be published without proper acknowledgement.

The right of Jesus Sanchez Cortes to be identified as Author of this work has been asserted by him in accordance with the Copyright, Designs and Patents Act 1988.

© 2023 The University of Leeds and Jesus Sanchez Cortes.

Acknowledgements

I would like to express my sincere gratitude to my supervisor, Dr Sadegh Azizi, for being my mentor. His invaluable support, guidance, insightful comments, constructive feedback, patience, unwavering encouragement, and passion for research have been instrumental throughout my PhD. Thank you for everything, Sadegh! I also extend my gratitude to Dr Petros Aristidou and Prof Kang Li for their valuable suggestions to improve my research.

My heartfelt appreciation to Mohammad Rezaei Jegarluei for his great and continuous support. His knowledge, expertise, and guidance have been essential in my research. Thank you for all the experiences throughout this journey, where the most valuable outcome is undoubtedly our friendship.

To my beloved friends David Suárez Escamilla and Rocío I. Ordoñez Jarillo. I will always be grateful to you for pushing me forward. You were the first ones who knew about my dreams and encouraged me to pursue them as if they were yours. Thank you!

My deepest gratitude to Guadalupe Martínez Ramírez for her invaluable help and guidance in my life. I am truly grateful for helping me find the sun on the foggiest days and wisely helping me get my feet back on the ground.

To my parents, Federico Sánchez Ramírez and Gloria Luz Cortés Ríos. Your sacrifices, guidance, and wisdom have helped me overcome challenges and achieve my goals. Your love, support, and unwavering belief in me have been a constant source of motivation. Thanks for giving me wings to soar!

To Centro Nacional de Control de Energía (CENACE) of Mexico for giving me practical experience in power systems and for the working permission during my PhD. Special thanks to Aureliano Sánchez Hernández, Nahúm Román Vargas, and my colleagues in the Operating Support Unit.

This research has been carried out under the sponsorship of Consejo Nacional de Ciencia y Tecnología (CONACyT) of Mexico and the University of Leeds.

Last but not least, thank you to all my beloved ones I could not mention here. Those who are and are no longer by my side, thank you! All of you contributed in different ways to go through this journey.

Jesús

Abstract

This doctoral thesis addresses the critical challenges posed by the integration of renewable energy sources (RESs) into modern power systems, focusing on the impact on frequency stability in the face of volatile inertia. With RESs rapidly penetrating into power grids to achieve global decarbonisation goals, the intermittent nature of these sources introduces operational complexities that demand novel strategies for preserving the active power balance. Traditional frequency control practices, built upon stable inertia contributions, face significant disruptions due to the reduced or absent inertia inherent to RESs. Consequently, the system frequency dynamics become swift and unpredictable, rendering conventional methods of frequency protection and control obsolete.

This research unveils a comprehensive methodology for detecting, locating, and estimating the magnitude of loss of generation (LoG) events in power systems characterised by substantial RES integration. Using the superimposed circuit methodology, nodal current injections from RESs are estimated, forming a system of linear equations that pinpoint LoG events by changes in the nodal currents with unparalleled accuracy. This method transcends traditional reliance on frequency measurements and knowledge of system inertia, making it robust and versatile in real-world applications.

Central to this research is the exploration of optimal fast frequency containment (OFFC), which consists of active power injections from RESs to swiftly arrest frequency deviations resulting from LoG events. A new paradigm emerges for OFFC, strategically decomposing the frequency response into transient and steady-state deviations. This approach yields an optimal allocation of power resources to effectively counteract LoG events. Contrary to conventional step-function injections, the proposed methodology ensures that transient deviations are prioritised, thereby conserving energy resources and minimising the time required for frequency to be recovered within statutory limits. The allocation of resources for correcting steady-state deviations subsequently follows if resources are available after mitigating the transient deviation, promoting the preservation of steam tur-

bines' lifespan.

In conclusion, this research highlights the critical intersections between RES integration, frequency stability, and LoG event dynamics. By introducing pioneering methodologies and challenging established assumptions, this thesis contributes to the evolution of power grid management strategies in an era of escalating renewable energy adoption. The insights derived bridge theoretical discourse with practical implications, empowering power systems to effectively navigate the complexities of renewable energy integration while ensuring resilience and stability.

CONTENTS

1	Introduction	1
1.1	Overview of frequency control in power systems	2
1.2	Research motivation	5
1.3	Literature review	6
1.3.1	Wide-area generation outage identification	6
1.3.2	Fast frequency containment	9
1.4	Research objectives	10
1.5	Methodology	10
1.6	Thesis contributions	13
1.7	Publications	15
1.8	Thesis outline	15
2	Legacy practices and state-of-the-art methodologies in frequency control	17
2.1	Overview	18
2.2	The swing equation	19
2.3	Under-frequency load shedding (UFLS)	22
2.3.1	Loss of generation	23
2.3.2	Maximum overload	23
2.3.3	Permissible frequency nadir	24
2.3.4	Frequency thresholds	24
2.3.5	Number of steps	25
2.3.6	Load to be shed by step	25
2.3.7	Time delays	26

2.3.8	Practical UFLS scheme: UK case	26
2.4	System frequency response (SFR) model	27
2.5	Impact of under-frequency operation on steam turbines	31
2.6	Fast frequency containment methodologies	34
2.6.1	Battery energy storage system (BESS)	35
2.6.2	High-voltage direct current (HVDC) links	35
2.6.3	Wind turbines	36
2.6.4	Synthetic inertia	37
2.6.5	Demand-side response (DSR)	38
2.6.6	Super-capacitors	38
2.7	Dynamic containment capability of RESs	39
2.8	Chapter conclusions	41
3	Detection, location, and size estimation of loss of generation events	43
3.1	Overview	44
3.2	Identification of loss of generation events	44
3.2.1	System of equations for each candidate LoG location	45
3.2.2	LoG location and size estimation	47
3.2.3	Discrimination between faults and LoG events	48
3.3	Accounting for the presence of RESs	48
3.3.1	Initial estimations ignoring non-monitored RESs	49
3.3.2	Modelling non-monitored RESs	50
3.3.3	Algorithm for the implementation of the proposed method	51
3.4	Study cases	53
3.4.1	General evaluation of the proposed method	54
3.4.2	Comparison with existing methods	58
3.4.3	Sensitivity to measurement, parameter, and topology errors	60
3.4.4	Observability and PMU coverage	63
3.4.5	Sensitivity to the number and locations of RESs	64
3.4.6	Practical application: Under-frequency load shedding	64
3.5	Chapter conclusions	66
4	Optimal fast frequency containment	69
4.1	Overview	70

4.2	A new paradigm for optimal fast frequency containment	70
4.2.1	Decomposition of the frequency response	71
4.2.2	Optimality of the flattened frequency response	72
4.3	Targeted active power injection	75
4.3.1	Extra power injection profile	75
4.3.2	Individual RESs contribution to the injection profile	78
4.4	Optimal fast frequency containment strategy	80
4.5	Study cases	81
4.5.1	System frequency response model derivation	81
4.5.2	General performance analysis	82
4.5.3	Comparison of the proposed OFFC with CFFC	85
4.6	Chapter conclusions	86
5	Conclusions and final remarks for future work	87
5.1	Overview	88
5.2	Research conclusions	88
5.3	Remarks for future work	90
5.4	Chapter conclusions	91
A	Worked example for LoG detection, location and size estimation on the IEEE 9-bus test system	93
A.1	Overview	94
A.2	System under study and initial assumptions	94
A.3	Identification, location, and size estimation of the LoG event	94
B	RES modelling	101
B.1	Overview	102
B.2	Voltage source converter	102
B.3	dq-frame transformation	103
B.4	Inner current control	107
B.5	Outer current control	110
B.5.1	Positive sequence outer control in steady-state conditions	110
B.5.2	Negative sequence outer control in steady-state conditions	111
B.5.3	Positive sequence outer control in transient conditions	112
B.5.4	Negative sequence outer control in transient conditions	112

Contents

B.6 Suppress negative sequence current	114
B.7 Imitate synchronous machine behaviour in the negative sequence	114
B.8 RES model in DIgSILENT PowerFactory	116
References	120

LIST OF FIGURES

1.1	Load-generation active power balance.	3
1.2	Regulation control loops [3].	3
1.3	Time frame of frequency regulation in response to an LoG event.	5
2.1	Plant diagram of the SFR model [52].	28
2.2	Sensitivity of the SFR model to different LoG sizes [52].	30
2.3	Sensitivity of the SFR model to different governor regulations [52].	30
2.4	Sensitivity of the SFR model to different inertias [52].	31
2.5	Sensitivity of the SFR model to different reheat times [52].	31
2.6	a) Heightened stress within the turbine resulting from operation at abnormal frequencies. b) Fatigue resistance curve of the blades in a steam turbine [72].	33
2.7	Frequency limits for the operation of a steam turbine [72, 73].	34
2.8	RES capability curve.	40
3.1	Superimposed circuit corresponding to an LoG event [90].	45
3.2	Flow chart of the proposed method [90].	52
3.3	<i>SoSR</i> of all candidate LoG locations after the SG outage at bus 33 [90].	55
3.4	<i>SoSR</i> of all candidate LoG locations after the RES outage at bus 24 [90].	55
3.5	LoG size estimation following outages at buses 24 and 33 [90].	56
3.6	<i>SoSR</i> of the tripped generation at bus 36 using different methods [90].	59
3.7	Impact of measurement errors on the minimum detectable LoG size [90].	63
3.8	Impact of the number of PMUs on the minimum detectable LoG size [90].	63
3.9	Possible RESs locations in the IEEE 39-bus test system.	65
3.10	Frequency response following UFLS based on different schemes [90].	66

4.1	Frequency containment by decomposing frequency response into transient and steady-state deviations [101].	71
4.2	Extra injection needed for removing transient frequency deviation [101].	77
4.3	Impact of (a) Simplified injections on the (b) Correction extent of the frequency response.	77
4.4	Conceptual diagram of the proposed OFFC strategy.	81
4.5	Impact of different correction extents on (a) Enhanced frequency response achieved, and (b) Extra power injections required for a 930 MW LoG event [101].	83
4.6	Frequency containment following an LoG event of 700 MW [101].	84
4.7	Optimal deployment of RES resources for the complete removal of the transient frequency deviation of a 700 MW LoG event.	84
4.8	Frequency nadir for different injections following a 1000 MW LoG [101].	85
A.1	IEEE 9-bus test system with RES penetration.	95
A.2	Superimposed circuit for an LoG event at bus 1.	95
B.1	Generic model for the RES [104].	102
B.2	Space phasor in the stationary dq-frame [104].	103
B.3	Space phasor in the rotatory dq-frame [104].	104
B.4	Decomposition of positive and negative sequences [104].	106
B.5	Decomposition of a time domain three-phase signal into positive and negative sequence d- and q-component [106].	106
B.6	Block diagram of the control plant describing the dynamics of the AC-side current in a dq-frame [104].	108
B.7	Block diagram of the inner current controller for control plant of Figure B.6 [104].	108
B.8	The whole inner current control process in the dq-frame [106].	109
B.9	Equivalent decoupled d- and q-axis current control loops [104].	109
B.10	Active power regulator [104].	110
B.11	Reactive power regulator [104].	111
B.12	AC voltage regulator [104].	111
B.13	Increment of the reactive current defined by the Tennet Grid Code [93].	113
B.14	RES control system (Modified from [106]).	117

B.15 Positive sequence outer controller (Modified from [106]). 119

List of Figures

LIST OF TABLES

2.1	UFLS Settings Implemented in the GB System [54].	27
3.1	Settings and Locations of RESs [90].	54
3.2	TVE in (%) of the Estimated Superimposed Current of RESs [90].	56
3.3	LoG Size Estimation Errors in (%) for SG Outages [90].	57
3.4	LoG Size Estimation Errors in (%) for RES Outages [90].	57
3.5	Comparison of the Proposed Method with Existing Methods [90].	59
3.6	General Performance of the Proposed Method [90].	60
3.7	Sensitivity to Measurement Errors [90].	61
3.8	Sensitivity to Measurement Noise.	61
3.9	Sensitivity to Generator/Line Parameter Errors [90].	62
3.10	LoG Location and Size Estimation Sensitivity to Topology Errors [90].	62
3.11	Sensitivity to the Number of PMUs [90].	64
3.12	Sensitivity to Settings, Number, and Locations of RESs [90].	65
4.1	SFR Models for the IEEE 39-Bus Test System [101].	82
4.2	Sensitivity of Frequency Nadir to Settings, Number, and Locations of RESs Following a 600 MW LoG Event [101].	85
4.3	Energy Needed to Contain Frequency within Statutory Limits [101].	86

Abbreviations

AGC	Automatic Generation Control	OFFC	Optimal Fast Frequency Containment
ALFC	Automatic Load-Frequency Control	OLS	Ordinary Least-Squares
AVR	Automatic Voltage Regulator	PCC	Point of Common Coupling
BESS	Battery Energy Storage System	PE	Power Electronics
CFFC	Conventional Fast Frequency Containment	PI	Proportional-Integral
CoI	Centre of Inertia	PLL	Phase-Locked Loop
DSR	Demand-Side Response	PMU	Phasor Measurement Unit
EMS	Energy Management System	RES	Renewable Energy Source
FDR	Frequency Disturbance Recorder	RoCoF	Rate of Change of Frequency
FFC	Fast Frequency Containment	SCADA	Supervisory Control and Data Acquisition
FPS	Frequency Propagation Speed	SFR	System Frequency Response
GB	Great Britain	SG	Synchronous Generator
HVDC	High-Voltage Direct Current	SHETL	Scottish Hydro Electric Transmission Limited
IEEE	Institute of Electrical and Electronics Engineers	SNR	Signal-to-Noise Ratio
KCL	Kirchhoff's Current Law	SoSR	Sum of Squared Residuals
KVL	Kirchhoff's Voltage Law	SPT	Scottish Power Transmission
LoG	Loss of Generation	TVE	Total Vector Error
LVRT	Low-Voltage Ride Through	UFLS	Under-Frequency Load Shedding
NGET	National Grid Electricity Transmission	VSC	Voltage Source Converter

CHAPTER 1

Introduction

1.1 Overview of frequency control in power systems

In order to address frequency control in power systems, it is essential to establish a comprehensive definition of frequency. Frequency denotes the quantification of complete cycles observed in a periodic waveform over the course of a second. In power generation, the frequency of the generated current and voltage signals is directly related to the speed of synchronous generators (SGs) [1]. This makes the frequency a unique parameter across the power system when operating in a steady-state condition, as all SGs are rotating at synchronous speed. However, power systems are subjected to different events, such as generation outages, abrupt changes in load, line outages, and faults, that affect the output power of either a specific SG when directly impacted or neighbouring SGs to the event. As a consequence, the remaining generators naturally respond by accelerating or decelerating their rotors, giving rise to frequency deviations from the nominal value.

The constancy in frequency indicates a balance between the active power generated and active power consumed by the loads, including transmission losses. Consequently, any perturbation to that balance is experienced as a frequency deviation by the power system. Specifically, under-frequency deviations result from consumption surpassing generation and vice versa, as shown in Figure 1.1. Frequency control aims to preserve the frequency stability in power systems, which refers to the ability of the power system to maintain the frequency nearly constant in a state of operating equilibrium after experiencing a significant active power imbalance [2].

Frequency control is carried out by the automatic load-frequency control (ALFC) loops implemented in each SG. Figure 1.2 shows how the ALFC loops control the speed of an SG to maintain its frequency at the nominal value by correcting any frequency deviation resulting from changes in the demand and generation. ALFC loops are described below [3]

- **Primary control loop.** This is a local control action that recovers the frequency from deviations by sending the speed signal to the governor. The turbine power output is then modified as a result of that change in speed (frequency). The primary control response is characterised by a persistent frequency deviation in

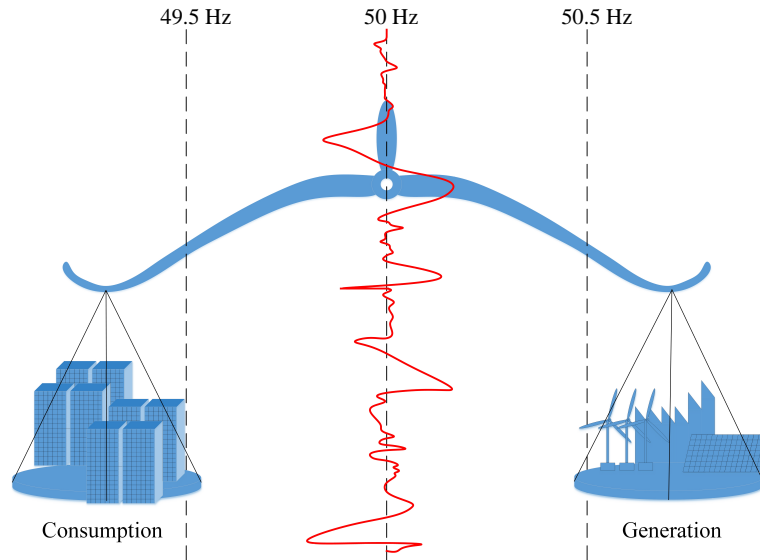


Figure 1.1: Load-generation active power balance.

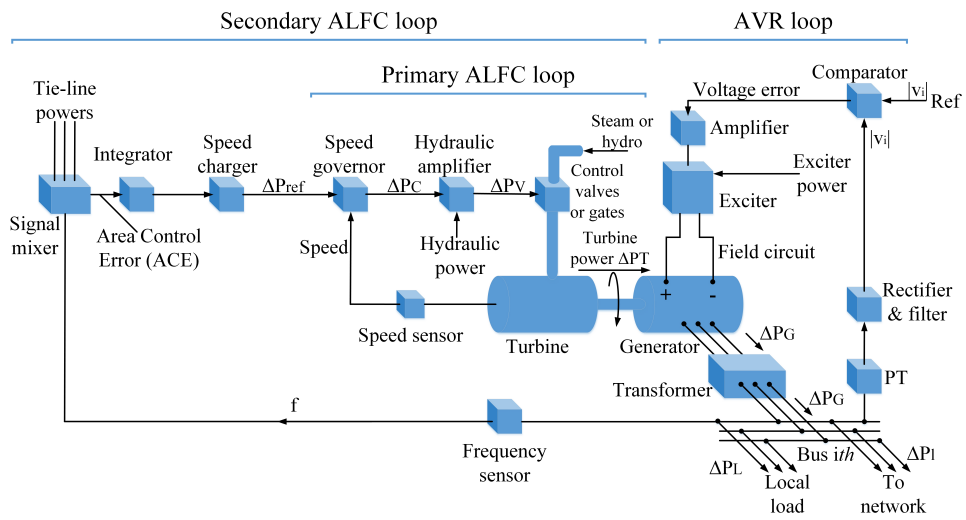


Figure 1.2: Regulation control loops [3].

steady-state. Frequency recovery can be achieved for variations of roughly 3 Hz within a time frame from 5 to 30 seconds.

- **Secondary control loop.** This control implements a proportional-integral (PI) controller to correct the steady-state frequency deviation resulting from the operation of the primary control loop. This is a centralised control action that adjusts the reference power of generators and is frequently carried out through automatic generation control (AGC). Typically, the operation time ranges from 30 seconds to a few minutes.
- **Tertiary control loop.** While this control loop is not universally adopted across all power systems, it is noteworthy that the tertiary control loop plays a pivotal role in facilitating primary and secondary regulations. By restoring primary and secondary reserves, this controller ensures that power systems are equipped with sufficient spinning and non-spinning reserves. These reserves can be effectively utilised over more extensive time intervals, ranging from approximately 15 minutes to well beyond an hour [4], [5].

As explained above, primary regulation requires approximately 5 seconds to change the frequency trajectory following an active power imbalance, with loss of generation (LoG) events being the most predominant and critical contributors to these imbalances. This delay is attributed to the inherent nature of the speed control, which relies on mechanical components for its operation. As a consequence, the rate of change of frequency (RoCoF) will solely depend on the system inertia and the LoG size during the initial seconds following an LoG event. In this context, system inertia can be understood as the system stiffness against LoG events. Figure 1.3 illustrates the frequency response in the time frame of the frequency regulation control loops following an LoG event.

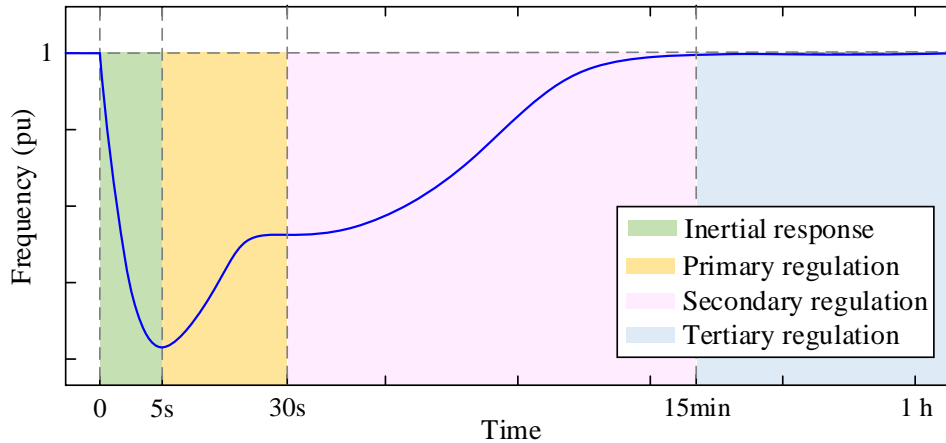


Figure 1.3: Time frame of frequency regulation in response to an LoG event.

1.2 Research motivation

The adoption of a predominantly renewable generation mix has emerged as a prominent trend in modern power systems, driven by the ambitious decarbonisation objectives established by numerous countries worldwide. As a result, there is an increasing number of renewable energy sources (RESs) that are steadily integrating into the power grid. This transition brings about new operational complexities attributed to the intermittent nature of RESs, which renders some important grid characteristics volatile. RESs are electrically decoupled from the power system by inverter-based interfaces, thereby providing little or no inertia to the system. Therefore, the growing penetration of RESs makes the system inertia variable in a wide range. This volatility in power system inertia, characterised by a substantially reduced lower limit, poses a pressing challenge for modern power systems, as inertia plays a crucial role in maintaining system stability against frequency deviations caused by LoG events. Consequently, these fundamental changes amplify the unpredictability and fluctuations in the frequency response, making the assumptions of traditional frequency protection and control practices increasingly invalid.

Large frequency deviations caused by LoG events are conventionally arrested by resorting to under-frequency load shedding (UFLS) schemes, which disconnect appropriate amounts of load to recover the balance between generation and consumption. Conventional UFLS relays are set such that they disconnect a predefined amount of

load every time the locally measured frequency violates a frequency/RoCoF threshold. This is essentially a trial-and-error process which is continued until the total amount of load shed by the relays becomes almost equal to the size of the LoG event. Variants of conventional UFLS schemes are slow in nature and take much longer to deal with larger LoG events. This becomes quite problematic in systems with highly reduced inertia as it results in low-frequency nadirs (the minimum frequency experienced following frequency deviations). Compacting frequency thresholds to avoid low-frequency nadirs is not considered an effective solution to this problem as it will result in over-shedding for small and medium-sized LoG events.

A solution to arrest large and fast frequency deviations in modern power systems is appealing to communication-based centralised approaches. This is to determine the size of LoG events in the control centre based on measurements gathered from across the grid. The knowledge of the LoG size can be used to inform the available RESs how much power they must inject to support the frequency response and, if needed, inform the UFLS relays how much load each must shed. Nonetheless, the latency of system-wide communication, system observability, errors in measurements, parameters, and topology, and the speed of calculations make existing approaches not reliable for real-time applications. This PhD research is aimed at proposing an optimal fast frequency containment (OFFC) strategy against LoG events that can guarantee the frequency stability of power systems with volatile inertia. The proposed OFFC will optimally deploy active power from available RESs to avoid resorting to UFLS where possible or shedding a minimal amount of load for a given LoG event by coordinating its operation with UFLS.

1.3 Literature review

1.3.1 Wide-area generation outage identification

RESs are progressively integrated into power systems globally as a result of significant efforts to meet the carbon reduction targets imposed by environmental policies concerning climate change [6, 7]. This integration makes the inertia of the power system volatile with a highly reduced lower boundary [8]. As a result, the inherent

unpredictability of system inertia is seen as a pressing challenge for modern power systems, as inertia relates to the power system's stiffness against frequency deviations caused by LoG events [9–11]. Frequency nadir, on the other hand, depends on how fast the remedial action is adopted to arrest the frequency decline. LoG events may lead to excessively low-frequency nadirs if the active power mismatch is not compensated promptly enough. This might trigger cascading trips of other generating units [12], thus jeopardizing system stability.

UFLS is a well-established remedial action against large LoG events [9]. The key aim of UFLS is to recover the active power balance by disconnecting an appropriate amount of load from the power system. In conventional UFLS schemes, a certain amount of load is shed if the local frequency falls below a pre-specified threshold on its decaying trajectory following an LoG event [12]. Conventional UFLS is inherently slow, and thus, some adaptive UFLS schemes have been introduced over the past two decades to expedite the load shedding process. Relying upon the swing equation of the centre of inertia (CoI), these methods assume relatively constant inertia for the system to estimate the size of LoG events [13]. In power systems with high penetration of renewables, however, inertia is highly volatile. This makes the underlying assumptions of adaptive methods invalid [14]. For instance, a high RoCoF does not necessarily indicate a large LoG size. As a result, these methods might fail to prevent frequency from reaching extremely low-frequency nadirs or may lead to over-shedding [15].

Most methods for locating and estimating the size of LoG events are based on frequency measurements. The assumption of [11] and [16] is the availability of specific sets of frequency measurements to estimate the LoG size at any location by directly relating the RoCoF to the lost power assuming a constant inertia in the power system. The recorded dynamic data of past events obtained from frequency disturbance recorders (FDRs) are used to classify the frequency characteristics of specific events into decision trees. These frequency characteristics are compared to frequency deviations to approximate the size of LoG events in [17–19]. The patterns described by LoG events in the system frequency can also be determined using the frequency propagation speed (FPS) [20]. When a generating unit is suddenly disconnected from the system, electromechanical waves are propagated from the event location to different directions in

the grid [21]. In [11], the FPS is employed to calculate the electrical distance between the LoG location and FDRs. References [22] and [23] incorporate a trigger algorithm based on the RoCoF for identifying LoG events. These methods assume the frequencies of all generating units are reliably collected at the control centre, which is not always possible [24]. Furthermore, due to the measurement noise and the variation in the rotational speed of the remaining generation, RoCoF calculation loses accuracy for a couple of hundreds of milliseconds after the LoG event [25]. Therefore, there is an unavoidable time delay between the LoG event and a reliable RoCoF measurement [25, 26].

Another promising research avenue is using phasor measurement units (PMUs) to monitor frequency variations in real-time at different locations in the power system. In [27] and [28], the disturbance arrival time is utilised to estimate the FPS of LoG events, and then the location and size of the tripped generator are calculated. The complexity in the electrical distance calculation compromises the accuracy of the LoG localisation by this approach. On the other hand, [29] and [30] use the aggregate inertia and the swing equation to detect the LoG event and estimate its size. In these methods, however, all generator frequencies should be monitored. This requirement contradicts the purpose because having measurements and communication infrastructure at all generating units would enable direct identification of the tripped generation using its circuit breaker status. To avoid using frequency measurements, [31] detects significant changes in the generation through active power measurements by relying on the SCADA/EMS. These methods are computationally expensive and can provide accurate results only if a fixed set of measurements is available. Any method relying upon a fixed set of data is highly prone to maloperation if any data is missed, e.g., caused by communication latencies and partial communication failures.

Reference [32] uses the impedance matrix with sparse PMU measurements to identify the change in the nodal current injection at the LoG location. The application of voltage and current data taken from one or two cycles following the event makes the method faster than those using frequency measurements. This method, however, does not account for RESs, which introduces inaccuracies in modelling the system, thus reducing its accuracy in systems with high penetration of renewables.

1.3.2 Fast frequency containment

Fast frequency containment (FFC) has become a critical requirement in power systems characterised by volatile inertia. Its primary purpose is to provide frequency support to counteract significant frequency deviations. In cases where the frequency decline following an LoG event is not promptly arrested, local protective systems will disconnect generators. The intention behind this is to prevent the frequency from reaching the resonant frequencies of steam turbine blades [12]. Therefore, failure to timely arrest the frequency decline will result in further LoG events and eventually a blackout.

To preserve the power system integrity against LoG events, fast recovery of the active power balance stands as a requisite objective. This can be achieved by resorting to UFLS or fast active power injection. As mentioned earlier, UFLS schemes regain the power balance by disconnecting an appropriate amount of load from the system [12]. Although load shedding is not a desirable solution, UFLS occasionally becomes the last resort against system collapse, given the inherent limitations of conventional generation units, which lack the capability of fast-acting power injections, contrary to what is observed in RESs.

The ability to quickly adjust the output power of generating units is essential for effectively counteracting frequency deviations following LoG events. RESs are not inherently responsive to frequency deviations because they are connected to the power grid through power electronics (PE) interfaces. This, along with the limited capacity of RESs to inject extra power, makes frequency containment challenging in the short time frame available before frequency drops significantly. Despite these challenges, RESs offer great potential that can resolve the foregoing shortcomings if used properly. Conventional fast frequency containment (CFFC) refers to injecting the extra power of RESs to mitigate frequency deviations. CFFC is faster than the primary control of SGs. This is because controlling the output of PE-based devices is typically much faster than the response time of SGs [33, 34].

CFFC has been traditionally designed to imitate the frequency response of SGs or to act as a step-function-shaped injection counteracting the LoG event. In this context, the extra power injection by RESs should have a fast ramp-up rate with a small

delay and be sustained for enough time to mitigate frequency deviations [33]. References [35–37] propose a controller that mimics the frequency regulation capability of SGs. Other researchers in [38–42] investigate approaches to deliver extra active power from batteries, super-capacitors, and high-voltage direct current (HVDC) links.

Some CFFC techniques focus on the kinetic energy stored in wind turbine rotors to slow the frequency decline following an LoG event. The primary challenge these methods try to address is the fact that the rotor speed of wind turbines is only allowed to decelerate to a limited extent [43, 44]. If not appropriately moderated, this may give rise to a frequency second dip, which in turn may lead to even a lower frequency nadir [45]. References [38, 39, 45–51] focus on preventing the frequency second dip while improving the frequency nadir using energy storage systems. However, these solutions are less attractive for practical applications due to the high cost and large-scale capacity requirements [47]. CFFC solutions, in principle, strive to shift the entire frequency response upward uniformly. This is not an optimal solution, for it does not lead to the highest frequency nadir. Therefore, CFFC may even unnecessarily increase the duration required for the frequency to return within statutory limits.

1.4 Research objectives

The objectives of this research are summarised below:

1. To estimate the size and location of loss of generation events in power systems with a high share of RESs.
2. To propose an optimal active power injection that leverages grid-forming RESs in achieving the maximum attainable frequency nadir.
3. To develop an optimal fast frequency containment strategy that guarantees the frequency stability of power systems with volatile inertia.

1.5 Methodology

To successfully achieve the proposed objectives, the following research methodology has been adopted.

1. To determine the size and location of LoG events using the superimposed circuit methodology.
 - 1.1 In order to facilitate the utilisation of the superimposed circuit methodology, it is imperative to ensure the availability of essential data. These crucial data sets consist of the bus impedance matrix, PMU data, as well as the active and reactive power setpoints associated with the RESs.
 - 1.2 The candidate tripped generation is substituted by a nodal current source in the superimposed circuit. Similarly, all RESs equipped with PMU measurements undergo this replacement procedure.
 - 1.3 The nodal current injection for each RES lacking PMU measurements is determined by considering its active and reactive power setpoints in conjunction with the terminal voltage.
 - 1.4 The actual tripped generation is identified by means of an index obtained through the application of the ordinary least-squares (OLS) method.
2. To maximise the effectiveness of available fast-acting resources to obtain the highest possible frequency nadir.
 - 2.1 Decomposition of the frequency response following an LoG event into transient and steady-state frequency deviations. This decomposition allows for the separation of the frequency depth into two components, one arising from transient effects that are short-lived and the other originating from steady-state effects that are permanent in nature.
 - 2.2 To establish a correlation between the accessible fast-acting resources from RESs and the portion of the frequency deviation that can be effectively mitigated by these injections. This relationship is established through the system frequency response (SFR) model [52].
 - 2.3 Formulation of the extra power injection profile as a function of the LoG size, correction extent based on the availability of fast-acting resources, and SFR model. Complete mitigation of the transient frequency deviation is achieved when sufficient active power is delivered within a brief period of time. In cases where the magnitude of the extra injection is insufficient, it is optimally allocated to rectify the transient frequency deviation to the

maximum possible extent. In the event of an excess of available power following the removal of the transient frequency deviation, the surplus is employed to mitigate the steady-state frequency deviation.

2.4 Formulation of the optimal coordination of power deployment of individual RES injections. This optimal coordination ensures that the SFR extra power injection profile is attained considering the technical and operational constraints of RESs. These injections maximise the utilisation of available fast-acting resources, resulting in the highest attainable frequency nadir for the given injection amount.

3. To develop an optimal fast frequency containment strategy.

3.1 Gather essential inputs for the OFFC strategy at the control centre. These data sets are the LoG size, the available amount of active power from each RES for extra injection, RESs ramp-up and ramp-down rates, and the SFR model. The latter is determined based on the system parameters and is maintained constant for a given power system and specific operating conditions.

3.2 Calculation of the SFR extra injection profile based on the availability of fast-acting resources to effectively mitigate the frequency deviation to the greatest extent possible, thereby achieving the highest possible frequency nadir.

3.3 In the event that the calculated optimal frequency nadir falls below the first frequency threshold to initiate load shedding, all fast-acting resources are deployed in accordance with the guidelines outlined in the Grid Code regulations [53]. Otherwise, optimal calculation and deployment of triangular injections are determined for each RES in the system.

1.6 Thesis contributions

The present research has made the following contributions to the field of electrical power engineering:

A method for estimating the size and location of LoG events in power systems with high penetration of RESs. The method uses the superimposed circuit methodology to account for the contribution of RESs using available PMU measurements. An overdetermined system of linear equations is obtained by manipulating the bus impedance matrix with reference to active and reactive power setpoints of RESs and available PMU data. The solvability concerns of the system of equations are hugely reduced by estimating the contribution of non-monitored RESs. The solution of this system provides the superimposed current injection of the tripped generation. The proposed method relies merely on rigorous Kirchhoff's voltage law (KVL) and Kirchhoff's current law (KCL) equations. Thus, it is faster than existing methods based on frequency measurements and more accurate than those requiring the knowledge of system inertia.

The presence of RESs is not considered by existing methods, which introduces significant errors if the penetration level is high. The proposed method is able to locate and estimate the size of LoG events with high accuracy regardless of whether the tripped generation is a synchronous generator or an RES. More importantly, there are no rigid constraints on the number and location of PMUs to obtain reliable estimations. Hence, if any PMU data is temporarily lost, the accuracy of the results is not noticeably affected. The proposed method demonstrates robustness against measurement, parameter, and topology errors. It is also shown that different numbers, locations, and penetration levels of RESs do not have a meaningful impact on the performance of the proposed method.

Another contribution that this research has set forth is a new paradigm for OFFC by decomposing the frequency response into transient and steady-state deviations. This lays the foundation for deriving the optimal size, shape, and time for extra power injections upon an LoG event. The foundational principle reinforcing OFFC is the removal or substantial reduction of transient frequency deviations while maintaining the system's settling frequency unchanged. This strategy serves to drastically minimise the

temporal and energetic investments required to restore the frequency to within statutory limits while concurrently preserving the steam turbines' lifespan.

In a groundbreaking departure from conventional practices, the paradigm stipulates the allocation of resources solely for the mitigation of transient frequency deviations, reserving the deployment of any remaining power resources for the mitigation of steady-state frequency deviations if necessary. It is shown that, contrary to common belief, the extra injection should not be a step-function counteracting the event unless the amount of power resources available is as large as the LoG size. A smaller yet well-timed triangular injection is shown to be the optimal injection for maximising the frequency nadir, as justified mathematically, and supported by extensive simulations. Targeting the extra injection at the removal of transient frequency deviations increases the extent of improvement made by a given amount of energy. This contribution serves as a testament to the efficacy, reliability, and transformative potential encapsulated within the proposed OFFC methodology.

The final contribution of this research lies in the optimal coordination of all accessible RESs to establish the targeted injection that produces the maximum achievable frequency nadir. The introduced optimisation algorithm takes into consideration system parameters, LoG detection and size estimation, and technical constraints of RESs, such as ramp-up/-down rates and maximum attainable power. Leveraging these input data, the algorithm facilitates the calculation of the optimal deployment of individual extra injections from RESs to build up the SFR extra injection that maximises the frequency nadir and contains the frequency in accordance with the stipulated requirements outlined in the Grid Code. The proposed targeted injection and coordinated deployment of resources prove to yield the highest possible frequency nadir for various LoG events for different numbers, locations, and penetration levels of RESs compared to existing FFC methods.

1.7 Publications

Under preparation

- **J. Sánchez Cortés**, M. Rezaei Jegarluei, and S. Azizi, “Optimal frequency containment in power systems with volatile inertia: The future is now with a new paradigm,” To be submitted to *IEEE Transactions in Industry Applications*, 2023.

Published

- **J. Sánchez Cortés**, M. Rezaei Jegarluei, P. Aristidou, K. Li, and S. Azizi, “Size/location estimation for loss of generation events in power systems with high penetration of renewables,” *Electric Power Systems Research*, vol. 219, 2023.
- **J. Sánchez Cortés**, M. Rezaei Jegarluei, and S. Azizi, “Targeted fast frequency response by decomposing frequency into transient and steady-state deviations,” *2023 International Conference on Energy Technologies for Future Grids (IEEE ETFG)*, Wollongong, Australia, 2023.

1.8 Thesis outline

The remainder of this thesis is structured as follows

Chapter 2 presents a comprehensive exploration of frequency control methodologies, encompassing both legacy practices and state-of-the-art strategies. Delving into the complicated dynamics of contemporary frequency control using RESs.

Chapter 3 introduces a pioneering method for the detection, localisation, and estimation of LoG events in power systems characterised by a substantial integration of RESs.

Chapter 4 introduces an innovative paradigm that redefines OFFC through a short yet targeted active power injection. This concept pivots around the novel approach of decomposing the system frequency response into transient and steady-state deviations.

Chapter 5 provides a comprehensive summary of the findings and conclusions derived from the present research. Additionally, it offers recommendations and suggestions pertaining to potential avenues for future research.

CHAPTER 2

Legacy practices and state-of-the-art
methodologies in frequency control

2.1 Overview

As briefly mentioned in Section 1.1, ALFC aims to contain any frequency deviations within permissible ranges to ensure the continuous operation of the power system. These ranges, namely operational and statutory limits, serve as crucial references for the system's integrity. The operational limits permit the frequency to fluctuate within a neighbourhood of ± 0.2 Hz from the nominal value, while the statutory limits impose a broader tolerance of $\pm 1\%$ deviation from the nominal value [54]. Power systems are designed to withstand the most credible events while ensuring that the frequency remains within statutory limits. Nonetheless, the reduction and variability in system inertia accelerate frequency dynamics, causing deviations from credible events to breach the statutory limits.

Following large LoG events, the frequency drops sharply, challenging the capability of ALFC to confine these deviations within the specified limits. Every time the frequency falls below the statutory limit, steam turbines are vulnerable to experiencing and accumulating irreversible damage, leading to a substantial reduction in their operational lifespan. Furthermore, in case the frequency decline is not promptly mitigated, local protection systems will initiate the disconnection of SGs to prevent the frequency from surpassing the blade resonant frequencies of steam turbines [12]. Failing to promptly arrest the frequency decline will inevitably result in the formation of electrical islands, leading to partial or complete blackouts caused by generator trips. To make matters worse, the frequency decline is accelerated even more in modern power systems due to the inherent volatility of system inertia. This reduces the time frame for system operators to react against LoG events before compromising the system's integrity, highlighting the urgency of promptly detecting and countering LoG events.

This chapter provides a thorough examination of frequency control methodologies, covering both legacy practices and cutting-edge strategies. In this context, a legacy practice refers to a traditional or established method that has been in use for a significant period and continues to be utilised, even as newer alternatives or technologies become available. It also can imply an outdated or conventional way of frequency control that might be replaced or updated in light of advancements or changing circumstances.

2.2 The swing equation

The swing equation is a fundamental equation used to model the dynamic behaviour of SGs in power systems. It describes the rotational motion of a generator's rotor as it responds to changes in mechanical and electrical conditions within the system through Newton's second law of motion. The swing equation is stated below [55]

$$J \frac{d^2 \theta_m}{dt^2} = T_a = T_m - T_e \quad (2.1)$$

where

J moment of inertia of the rotatory masses in kgm^2

θ_m rotor's angular shift in rad

T_a accelerating torque in Nm

T_m mechanical torque in Nm

T_e electrical torque in Nm

As can be seen in (2.1), the accelerating torque T_a emerges as the difference between the mechanical (T_m) and electrical (T_e) torques. In the scenario where the SG works at synchronous speed, a state of equilibrium prevails between the mechanical and electrical torques. In this state, the magnitudes of both torques are identical, leading to the nullification of T_a . Consequently, any perturbation in either T_m or T_e gives rise to a non-zero value for T_a , thereby inducing either acceleration or deceleration in the SG's rotor depending on the sign of T_a . The SG's rotor accelerates if T_a is positive and decelerates if T_a is negative [56]. It is worth pointing out the inherent correlation between speed and frequency in SGs. This intrinsic connection enables frequency control of SGs by controlling their speed.

The rotor angle θ_m in (2.1) is measured regarding a stationary axis. Nonetheless, it is more appropriate to express the rotor's angle shift with respect to a rotatory axis,

as below [55]

$$\theta_m = \omega_{sm}t + \delta_m \quad (2.2)$$

where ω_{sm} and δ_m are the synchronous speed and rotor's angle shift, respectively. Taking the second derivative of (2.2), equation (2.1) can be rewritten as follows

$$J \frac{d^2 \delta_m}{dt^2} = T_a = T_m - T_e \quad (2.3)$$

T_m and T_e correspond to the mechanical torque on the generator's shaft and the air-gap power between the stator and rotor of the SG. Therefore, these two torques account for the mechanical power impressed by the prime mover on the generator's shaft and the electrical output power of the SG, respectively.

Let $\omega_m = \frac{d\theta_m}{dt}$ be the angular velocity of the rotor. By multiplying this angular velocity by (2.3), the swing equation can be expressed in terms of powers [12, 57]

$$M \frac{d^2 \delta_m}{dt^2} = P_a = P_m - P_e \quad (2.4)$$

where P_a , P_m , and P_e stand respectively for the accelerating power, mechanical power, and electrical power of the SG, each expressed in watts (W). Moreover, M represents the momentum of inertia or simply called the inertia of the rotor when the SG is working at synchronous speed. This means that M is a measure of the distribution of mass around the axis of rotation. It quantifies the system's resistance to changes in angular velocity, i.e., $M = J\omega_m$ at $\omega_m = \omega_{sm}$ [57].

The inertia constant, denoted by H , is usually provided by machine manufacturers using the kinetic energy formulation as

$$H = \frac{\frac{1}{2}J\omega_{sm}^2}{S_{mach}} = \frac{\frac{1}{2}M\omega_{sm}}{S_{mach}} \quad (2.5)$$

where H is quantified in megajoules per megavolt-ampere (MJ/MVA) and indicates the ratio of the stored kinetic energy in the rotatory masses at synchronous speed to the rated power S_{mach} of the SG. H reflects the ability of the generator to resist changes in speed (frequency) and is a crucial factor in determining the system's transient stability. Let us now write the momentum of inertia M in terms of the inertia constant H

$$M = \frac{2H}{\omega_{sm}} S_{\text{mach}} \quad (2.6)$$

Substituting (2.6) into (2.4), the swing equation can be written as

$$\frac{2H}{\omega_{sm}} \frac{d^2 \delta_m}{dt^2} = P_a = P_m - P_e \quad (2.7)$$

Equation (2.7) is expressed in pu due to all powers being divided by S_{mach} . It is worth noting that both δ_m and ω_{sm} are expressed in mechanical radians and mechanical radians per second, respectively. This implies that both δ_m and ω_{sm} are consistent in units regardless of whether they are denominated in mechanical or electrical degrees or radians. Consequently, δ_m and ω_{sm} can simply be written as δ and ω_s , respectively, to indicate that the quantities are expressed in electrical degrees or radians.

Let us consider the SG works in steady-state conditions, i.e., the SG operates at synchronous speed ($\omega_s = \omega_{sm} = 1.0 pu$). The swing equation can finally be written as

$$2H \frac{df}{dt} = P_a = P_m - P_e \quad (2.8)$$

As can be seen in (2.8), the rotor angular acceleration $\frac{d^2 \delta_m}{dt^2}$ is presented as $\frac{df}{dt}$. This is because the rotor angular acceleration can be written as either the second derivative of the rotor's angle shift or the first derivative of the rotor's angular velocity. Recalling the speed-frequency relationship of SGs, the rotor's angular velocity can be written as the generator's frequency. Therefore, the rotor angular acceleration equals the first derivative of the generator's frequency, also referred to as RoCoF.

Equation (2.8) is referred to as the swing equation and models the dynamic behaviour of the inertial response of SGs. The complete modelling of the whole dynamic behaviour following an active power imbalance is achieved by introducing the frequency-dependent load damping, which serves as a stabilising property of the power system, as shown below [58]

$$2H \frac{df}{dt} + D \Delta f = P_a = P_m - P_e \quad (2.9)$$

where D is the frequency-dependent load damping factor and Δf is the frequency deviation from the nominal value [58]. It is worth pointing out that in frequency protection

applications, the time frame of interest ranges within the first few milliseconds following the event inception. During this time frame, Δf is almost zero so that $D\Delta f$ can be safely ignored [59]. This means that both expressions (2.8) and (2.9) can provide accurate results in the first instants following the LoG event. For this reason, either (2.8) or (2.9) can be used as the core to several conventional approaches for frequency control and protection schemes [58, 60].

2.3 Under-frequency load shedding (UFLS)

UFLS is a remedial action implemented to maintain the frequency stability of power systems by disconnecting blocks of load. Specifically, UFLS safeguards against drastic frequency deviations caused by LoG events [61]. This abrupt imbalance between power generation and demand leads to a rapid decline in frequency, which depends on the LoG size and system inertia [52]. Unfortunately, the response time of control mechanisms in other generators might not be swift enough to prevent system collapse or separation into multiple islands. Moreover, operating steam turbines at low frequencies will result in irreversible damage [62].

UFLS operation is carried out in stages, each defined by a frequency/RoCoF threshold, the amount of load to be shed, and a time delay [63]. Following an LoG event, the UFLS scheme operation is triggered when the system frequency violates the first frequency threshold. If frequency continues to decrease, the scheme disconnects a predetermined amount of load. Successful restoration of frequency, ensuring it is within statutory limits, depends on the amount of load shed. If the total load shed is not enough to regain the active power balance, the frequency will be recovered to a certain extent. The resultant frequency deviation from the UFLS operation can be recovered to the nominal value if the frequency is within the operational range of primary regulation. Thus, load shedding reduces the connected load to a level safely manageable by available generation.

The following considerations must be taken into account to design a UFLS program

- Ensuring the expeditious activation of the UFLS scheme prior to the frequency

stability is at risk.

- Disconnecting only the essential loads required for frequency recovery.
- Priority should be given to initiating load shedding among loads that would be least affected by an electrical power disruption.
- Preferentially disconnecting loads that can be readily restored before those requiring substantial investments for restarting their operations is recommended.
- Thermal power plants hold a higher order of importance within the power system's hierarchy due to they are highly sensitive to frequency variations. The operation of steam turbines outside their continuous operating region reduces their lifespan.
- Effective communication between thermal systems and UFLS relays is essential to initiate the process of load shedding promptly.
- Safeguarding the operability of critical safety-related infrastructure for maintaining the system's integrity and security is paramount. Therefore, their disconnection should be avoided.

2.3.1 Loss of generation

An LoG event is experienced by the system as a step reduction in the active power generated. Following an LoG event, there is a reduction in generation, and voltage and frequency levels immediately drop. Notably, frequency remains the prominent indicator signalling the occurrence of the LoG event, differentiating it from other occurrences, such as system faults, where voltage fluctuations can arise [64]. The LoG size is formally characterised as an overload and is intricately linked with the inherent inertia of the system [52].

2.3.2 Maximum overload

Load shedding strategies are meticulously designed to address worst-case scenarios, typically involving overloads of 30% to 50% [65]. The paramount objective is to disconnect an appropriate load magnitude that would effectively restore frequency to acceptable levels. However, due to the unpredictability of the LoG size, there remains

an inherent uncertainty regarding the scheme's reliability and its capability to successfully arrest the frequency decline for a given LoG event [63]. Consequently, the foremost design step is to determine the maximum load that should be shed by the UFLS scheme, which can be quantified using the subsequent expression [62]

$$\% \text{ overload} = \frac{\text{Load} - \text{Remaining Generation}}{\text{Remaining Generation}} 100 \quad (2.10)$$

where the LoG size is Load-Remaining Generation. The extent of overload in the system following the LoG event can be derived using (2.10). Importantly, frequency can be rectified by disconnecting a load volume equivalent to the LoG percentage.

2.3.3 Permissible frequency nadir

Efficient coordination between load shedding protocols and equipment limitations during low-frequency operational scenarios is essential. These constraints primarily concern the functionality of auxiliary systems in power plants. Based on empirical assessments, the effectiveness of these auxiliary systems diminishes, and the overall power plant output reduces as the operational frequency falls 1 Hz from the nominal value. To account for safety margins, the largest frequency nadir is usually confined to remain within the vicinity of 0.95 pu, i.e., 47.5 Hz for a 50 Hz system or 57 Hz for a 60 Hz system.

2.3.4 Frequency thresholds

Choosing an initial frequency value situated near the operational limit can lead to the scheme's activation during dynamic events when the frequency temporarily dips to lower values, prompting unwarranted load shedding. To avert unnecessary load shedding, the initial frequency threshold is commonly placed at the continuous operational limit of turbines, i.e., at the statutory limits [66]. Moreover, a time delay between the UFLS relay and the circuit breaker exists, typically spanning 10 to 15 cycles, in addition to the inherent delay in the scheme itself [65].

It is advisable for subsequent step frequencies to exhibit a separation of 0.2 Hz in the initial stages and between 0.3 Hz and 0.4 Hz in the following stages [62, 65]. This approach gives enough time to the scheme for the operation of following steps if needed

without reaching excessively low-frequency nadirs. In practice, the initial frequency threshold for load shedding is normally established below the statutory limits. This is to allow other frequency control strategies, such as ALFC and FFC, to arrest the frequency decline before resorting to load shedding.

2.3.5 Number of steps

As a common practice, UFLS schemes generally encompass a range of three to six steps, though the scope of disconnection scenarios is not constrained by a set number [62, 65]. The underlying aim involves a gradual load shedding approach aimed at preventing the shedding of significant amounts of load for relatively less severe LoG events. Consequently, designs embracing a higher number of steps are more frequently favoured. However, the pivotal challenge during load shedding scheme formulation lies in the ambiguity surrounding the optimal quantity of steps and the load amount to be shed at each step. This ambiguity arises from the risk of overshooting or undershooting the required load shedding, consequently failing to restore the frequency to an acceptable level [65].

The number of steps of a UFLS scheme is closely tethered to its maximum overload capacity. Hence, adopting designs featuring multiple disconnection stages affords more benefits as it facilitates a judicious distribution of load shedding across these steps [67].

2.3.6 Load to be shed by step

The determination of the amount of load to be shed at each step of the UFLS scheme is typically achieved through a trial-and-error methodology. This approach depends on various factors intrinsic to the power system's characteristics. Consequently, devising a specific criterion as a universally applicable strategy for load shedding proves problematic. The success of such a criterion depends upon the maximum overload that the UFLS scheme can handle and the power system's characteristics.

Outlined below are three distinct methodologies for implementing load shedding on the UFLS scheme. The effectiveness of each approach varies based on the particular power system and operational conditions in which it is deployed [65]. The first criterion entails initiating load disconnection with a significant load reduction in the initial stages

and subsequently decreasing the load as the steps progress. Conversely, the second criterion involves commencing with a modest load disconnection in the initial phases and progressively increasing the load disconnection until reaching the final step. Lastly, the third criterion calls for a consistent load disconnection magnitude across all steps.

The determination of the optimal load to disconnect in each step relies on the maximum overload that the scheme can accommodate. A commonly adopted strategy is to shed approximately 10% of the total system load during the first step, with subsequent steps carefully chosen to ensure the total amount of load shed aligns with the maximum overload for which the UFLS scheme has been designed [67]. Additionally, the application of optimisation algorithms can help establish the load to be shed per step. Certain algorithms also facilitate the identification of the optimal zone for implementing the disconnection strategy [68].

2.3.7 Time delays

The time delay in each step of the UFLS scheme is employed as a selectivity measure to prevent unnecessary scheme activation during frequency oscillations. The typically utilised time delay ranges from 0.3 to 0.4 seconds. Nonetheless, it is not feasible to universally apply this time frame to all systems [62]. The time delay can be adjusted either higher or lower, depending upon establishing effective coordination with the turbo-generator [65].

2.3.8 Practical UFLS scheme: UK case

UFLS programs are designed and implemented in real power systems following the previous criteria and engineering judgments. In the Great Britain (GB) power system, UFLS is initiated when the system frequency descends below the threshold of 48.8 Hz. UFLS is implemented to prevent the frequency from declining to 47.5 Hz, thereby maintaining the system's integrity. Upon activation, low-frequency relays send a trip command to open circuit breakers in distribution networks effecting a controlled disconnection of demand within the range of 5% to 60% of the total national demand, depending on the transmission area. There are three different transmission operators in the GB power system, which are National Grid Electricity Transmission (NGET),

Table 2.1: UFLS Settings Implemented in the GB System [54].

Frequency (Hz)	% Demand disconnection for Network Operator		
	NGET	SPT	SHETL
48.8	5		
48.75	5		
48.7	10		
48.6	7.5		10
48.5	7.5	10	
48.4	7.5	10	10
48.2	7.5	10	10
48.0	5	10	10
47.8	5		
Total % Demand	60	40	40

Scottish Power Transmission (SPT), and Scottish Hydro Electric Transmission Limited (SHETL). The UFLS program consists of nine stages, each one associated with a block of load to be shed of 5%, 7.5%, and 10% of the total demand, as shown in Table 2.1. Load shedding in the GB system is designed to occur within a duration not exceeding 200 milliseconds whenever feasible [54, 69].

2.4 System frequency response (SFR) model

This section aims to provide a comprehensive insight into the derivation of the SFR model. Should readers wish to delve deeper into this process, a more detailed explanation can be found in [52]. The main purpose of this section is to elucidate the relevance of the SFR model within the proposed methodologies.

The SFR model, characterised as a second-order minimal-phase transfer function, plays a pivotal role in capturing the resulting CoI frequency deviation following a sudden perturbation in the active power balance of a large-scale power system. This model is a simplified representation of the essential dynamic characteristics of a power system dominated by reheat steam turbines. To derive the reduced model, non-linearities are

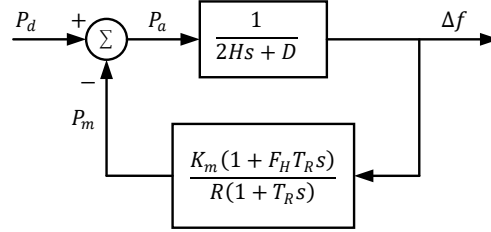


Figure 2.1: Plant diagram of the SFR model [52].

excluded from the formulation, as well as slower thermal dynamics of the boiler and the rapid response of the generator due to their distinct temporal characteristics. The SFR model then only focuses on intermediate frequencies, i.e., those frequencies closely linked to fluctuations in the shaft velocity. This makes the derived model retain only the core dynamics intrinsic to the overall power system.

The SFR model averages the most representative frequency dynamics across various generating units into a singular coherent representation. In essence, the SFR model transforms all generating units in a power system into a singular equivalent generating unit. The parameters of this equivalent unit are derived through the CoI calculation, incorporating the parameters of all machines in the power system. Consequently, the frequency response generated by the SFR model harmoniously aligns with the CoI frequency deviation, which is defined as the weighted average of all local frequency deviations in the system. Key parameters that define the SFR model include the reheat time constant (T_R), which significantly influences turbine power output, system inertia (H), and droop characteristic, represented as the inverse of the governor's regulation constant ($\frac{1}{R}$). Note that the SFR model is general and is used to represent the whole frequency dynamics over any time frame, i.e., it can be used to represent the frequency behaviour during the inertial, primary, and secondary responses. For this reason, the modelling includes the frequency-dependent load damping (D). This leads to the reduced plant model shown in Figure 2.1 whose parameters are detailed below

P_d disturbance power in pu , where $P_d < 0$ for LoG events and $P_d > 0$ for generating increments

P_m turbine mechanical power in pu

P_a accelerating power in *pu*

H inertia constant in *sec*

D frequency dependence of load

K_m mechanical power gain factor

F_H fraction of the total power generated by the high-pressure turbine

T_R reheat time constant in *sec*

R governor regulation

Δf frequency deviation in *pu*

From the plant diagram shown in Figure 2.1, we can establish an expression for the frequency deviation as a function of the magnitude of disturbance P_d and system parameters, as below

$$\Delta f(s) = \left(\frac{R\omega_n^2}{DR + K_m} \right) \left(\frac{(1 + T_R s) P_d}{s^2 + 2\zeta\omega_n s + \omega_n^2} \right) \quad (2.11)$$

where parameters ζ and ω_n represent the damping factor and natural frequency of the system, respectively. These parameters are mathematically defined using the corresponding parameters in Figure 2.1 to express the transfer function (2.11) in its canonical form.

The time domain expression for the frequency deviation can be readily obtained by computing the inverse Laplace transform of (2.11). It is noteworthy that LoG events can be modelled as negative step functions in the Laplace domain. This is because the lost power is experienced by the power system as a sudden step change in the active power injection. Therefore, the time domain expression for the frequency deviation following an LoG event is as follows

$$\Delta f(t) = \frac{RP_d}{DR + K_m} \left[1 + \alpha e^{-\zeta\omega_n t} \sin(\omega_r t + \phi) \right] \quad (2.12)$$

where α , ω_r , and ϕ are constants composed by the system parameters. Likewise (2.11),

these constants are defined to simplify the presentation of the expression. Let us now examine the sensitivity of the SFR model to the variation of the dominant parameters and LoG sizes. In doing so, equation (2.12) is computed for different values of T_R , H , R , and P_d . Results are presented from Figure 2.2 to Figure 2.5.

The derived SFR model is very practical since it can approximate the CoI frequency behaviour following LoG events for any power system as long as the system parameters are known. In control centres, fortunately, most of these parameters are accessible, and the rest can be estimated by simulation studies of the operating condition(s) of interest.

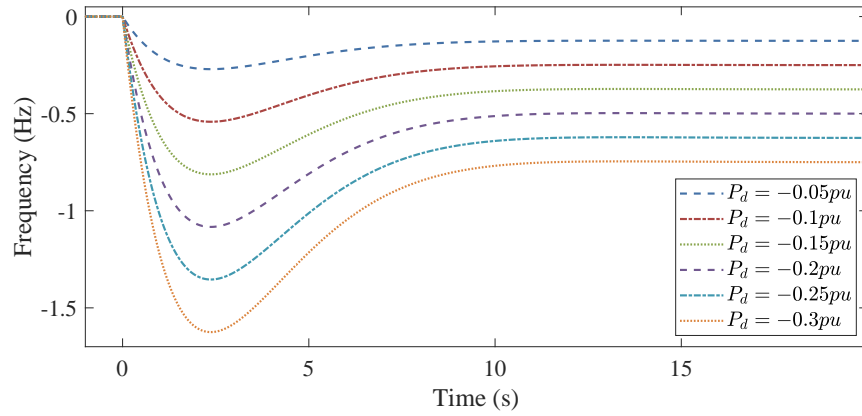


Figure 2.2: Sensitivity of the SFR model to different LoG sizes [52].

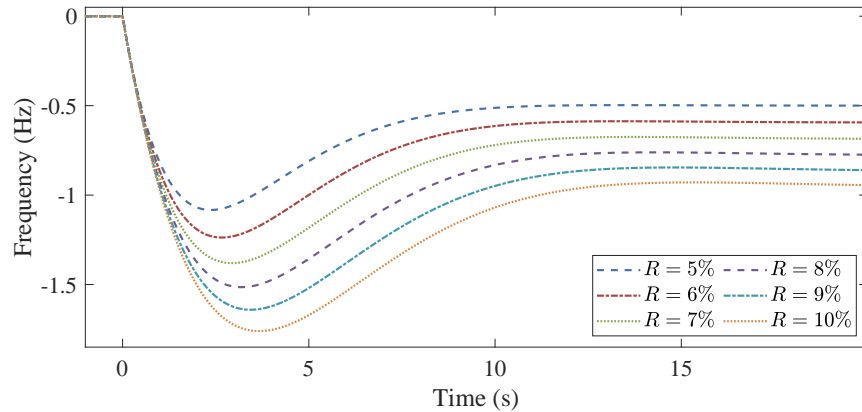


Figure 2.3: Sensitivity of the SFR model to different governor regulations [52].

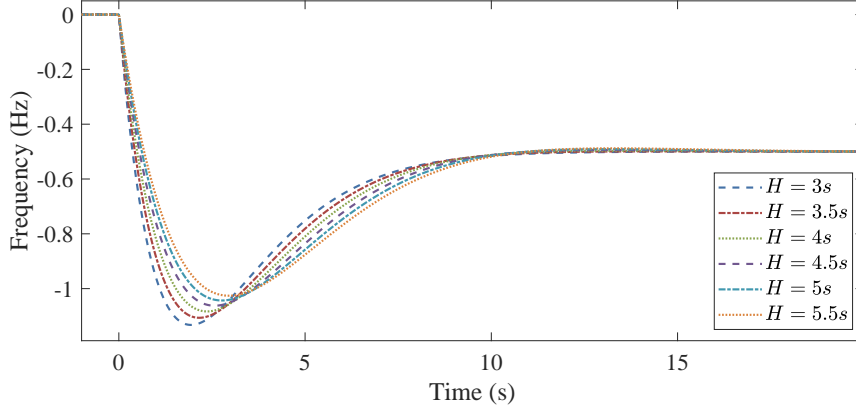


Figure 2.4: Sensitivity of the SFR model to different inertias [52].

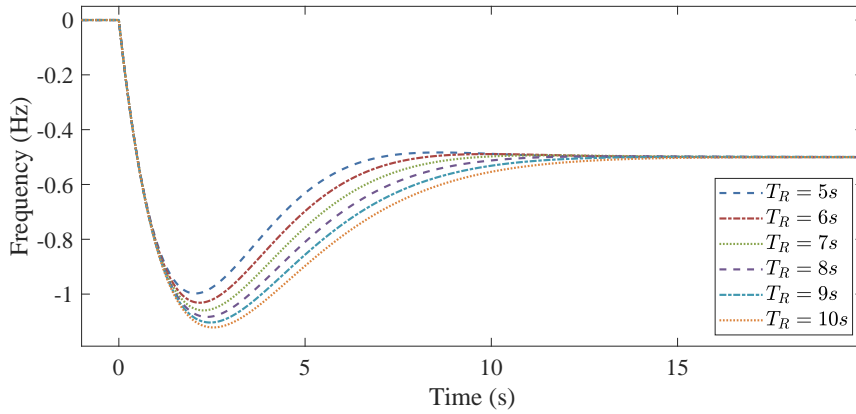


Figure 2.5: Sensitivity of the SFR model to different reheat times [52].

2.5 Impact of under-frequency operation on steam turbines

Owing to the heightened sensitivity of steam turbines to frequency variations, the protection strategies for these types of equipment aim to shield them against substantial damage that may arise from extended operation at either low or high frequencies [62, 65]. In doing so, UFLS programs are implemented in all power systems. These programs serve the purpose of disconnecting an appropriate amount of load to facilitate the restoration of the active power balance, thereby containing the system's frequency to a value closely aligned with the nominal frequency. In practice, however, UFLS operation reveals that achieving an absolute equilibrium between generated and demanded

power via load shedding remains elusive. This stems from the uncertainty inherent in estimating the magnitude of LoG events and their distribution among system loads. As a consequence, overshooting or deficits in load shedding during the operational execution of these schemes become nearly unavoidable [62, 67].

The combined operation of UFLS and the speed governor permits the attainment of an adequate frequency response against most LoG events in conventional power systems. This action is effective since the primary regulation assists in mitigating potential over-frequency or under-frequency conditions resulting from UFLS activation. This holds true as long as the system frequency remains within the continuous operating region of steam turbines. Deviations beyond this region trigger the protection scheme of the steam turbine, leading to the disconnection of the equipment from the grid. Such an action could potentially initiate a cascade tripping of generating units, ultimately leading to a blackout [9, 12]. In power systems with high penetration of RESs, this problem becomes more significant. This is due to the volatility in the system's frequency dynamics, coupled with the limited availability of primary regulation resources. Furthermore, the fluctuating system inertia contradicts the assumption of constant inertia upon which the foundation of UFLS is built [70].

Steam turbines are comprised of various sections containing multiple rows of blades of differing lengths. Distinctive design attributes are assigned to each blade segment to guarantee that they are propelled adequately by a precise steam volume at different pressure levels. As a result, every blade segment showcases its own unique mechanical resonance frequencies. Consequently, insufficient steam intake into the turbine can lead to blade distortion, culminating in an unintended turbine rotation and persistent structural deficiencies [62, 71].

When a steam turbine is operated at low frequencies or frequencies that are in close proximity to blade resonance frequencies, it experiences and accumulates a certain degree of damage. In essence, the stress within the turbine undergoes exponential growth during such conditions [65, 71]. This phenomenon is clearly illustrated in Figure 2.6a, where the stress levels denoted as A, B, and C remain non-destructive to the turbine when it functions within the permissible frequency range. Conversely, the

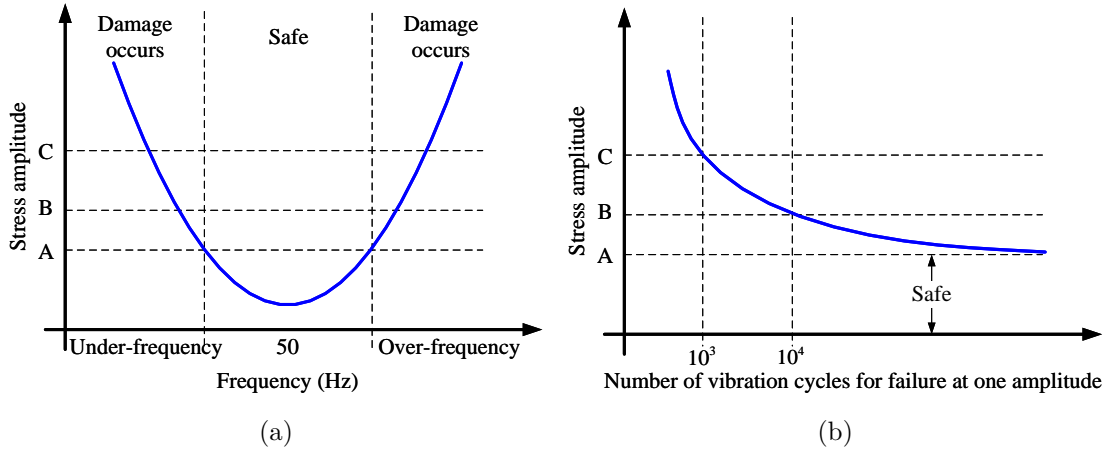


Figure 2.6: a) Heightened stress within the turbine resulting from operation at abnormal frequencies. b) Fatigue resistance curve of the blades in a steam turbine [72].

graph demonstrates how stress levels within the turbine escalate when it operates beyond its continuous operational boundaries. Figure 2.6b shows a fatigue resistance curve with the same stress levels A, B, and C of the blades of the turbine. As can be seen, stress amplitudes falling below level A ensure safe turbine operation without incurring damage. However, operation at stress level B potentially triggers failure after approximately 10,000 vibration cycles, while operation at stress level C elevates the risk of failure, occurring after approximately 1,000 vibration cycles [62].

Based on an extensive investigation into frequency vibrations across various blade blocks within steam turbines, the depicted time limits in Figure 2.7 are recommended for operations involving abnormal frequencies. These prescribed limits signify the estimated minimum time until failure of the most vulnerable turbine blades, both in instances of under-frequency and over-frequency operation. It is evident that when the frequency deviates by 5% or more, the operational time frames become notably brief. Thus, the possibility of operation for 1 second at 0.94 pu becomes apparent. Similarly, the damage-free operation can be sustained at 0.95 pu or 1.05 pu, which are the statutory limits highlighting that a 1% variation from the nominal frequency does not significantly impact the steam turbine’s lifespan [72, 73].

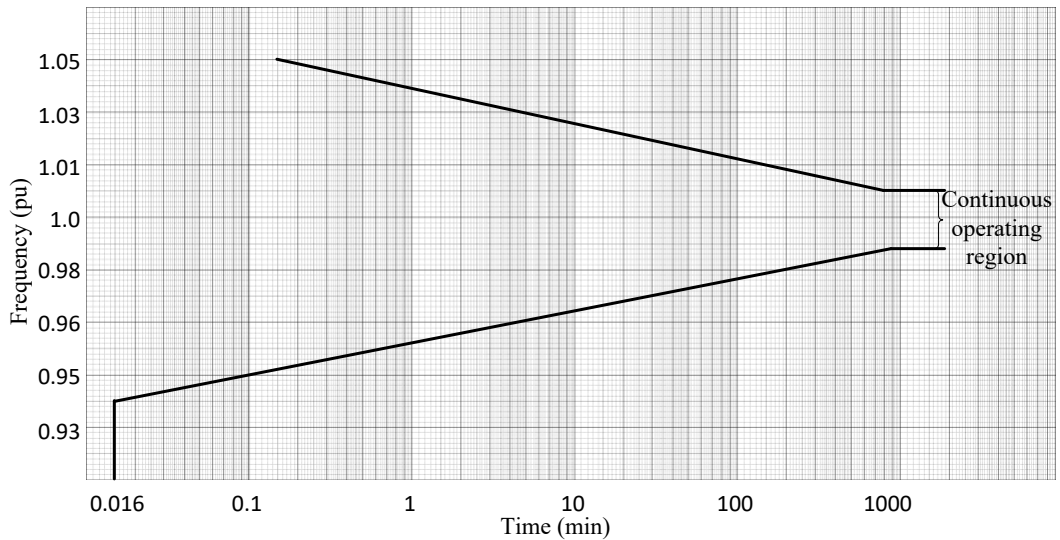


Figure 2.7: Frequency limits for the operation of a steam turbine [72, 73].

2.6 Fast frequency containment methodologies

RESs play a vital role in the net-zero transition. Nonetheless, the reduced or null inertia provided by these sources of generation presents significant technical obstacles in maintaining system frequency stability [34]. Furthermore, RESs do not possess a natural response to frequency fluctuations due to their connection to the grid via PE-based interfaces. This, coupled with the limited extra injection that they can deliver, adds complexity to containing frequency deviations before the frequency reaches dangerous values. RESs, however, also have the ability to change their power setpoints rapidly and, consequently, their output power faster than SGs. For this reason, various methods have been proposed in the literature to exploit this benefit from RESs to contribute to frequency containment. In doing so, RESs are ideally required to mimic the characteristics exhibited by SGs or inject active power in the form of a step-function to neutralise the effects of LoG events. Although a step-function injection is not practical in reality, this shape of response is defined in the literature as the ideal injection. The reason is that a step-function injection can fully mitigate the effects of the LoG event before the frequency drops if applied at the LoG inception time with the same magnitude but in the opposite direction of the LoG event [33]. In the following subsections, the existing methodologies to provide FCC response are described.

2.6.1 Battery energy storage system (BESS)

BESSs have emerged as crucial tools for frequency containment in modern power systems. BESSs step in as a rapid-response solution. By virtue of their ability to swiftly charge and discharge energy, BESSs can instantaneously inject or absorb power into the grid, effectively dampening frequency deviations. When the system frequency drops due to an increase in demand or an LoG event, BESSs can immediately discharge stored energy to raise the frequency back within statutory limits [74]. Conversely, when the system frequency rises due to reduced demand or excess in generation, BESSs can absorb the energy surplus. This dynamic response capability of BESSs aligns with the specifications of the dynamic containment service [53].

In addition to their rapid response, BESSs also excel at providing inertial response, a characteristic traditionally associated with SGs. BESSs can emulate this inertia by modulating their power output changes over time. This inertial emulation becomes essential during LoG events, as it helps mitigate frequency deviations that might otherwise lead to instability. As renewable penetration continues to rise, BESSs' ability to provide both rapid and inertial responses positions them as indispensable assets in frequency containment. BESSs, however, are considerably costly to be adopted at large-scale in modern power systems [47].

2.6.2 High-voltage direct current (HVDC) links

HVDC links can provide support to frequency containment against LoG events through their ability to rapidly control power flow and facilitate dynamic adjustments between interconnected grids. Following an LoG event, HVDC links can respond swiftly by adjusting power flow to transfer surplus power from regions with higher frequency to those with lower frequency [39]. The rapid power transfer helps mitigate the frequency decline and prevent it from falling below the statutory limits. Additionally, some advanced HVDC systems are designed to mimic the inertial response of SGs. They can emulate the rapid power adjustments that SGs provide during LoG events, further contributing to stabilising the system frequency [41].

2.6.3 Wind turbines

Modern wind turbines are equipped with sophisticated control systems that allow them to respond rapidly to changes in the system frequency. By either injecting or absorbing power into the grid, wind turbines help counteract frequency deviations when the system frequency deviates from the nominal value [75]. This capability is particularly valuable in scenarios where a large active power imbalance takes place, as is the case of LoG events. Thus, wind turbines actively participate in frequency containment by deploying fast active power injections. In what follows, the classification of frequency response techniques of wind turbines is detailed [76].

2.6.3.1 Droop control

Droop control constitutes a decentralised strategy that endows wind turbines with the capability to modify their power output in response to frequency deviations. The implementation of droop control allows wind turbines to actively contribute to frequency containment, effectively simulating the primary regulation function exhibited by SGs [77]. Frequency deviations caused by active power imbalances are effectively counteracted by wind turbines employing the droop control approach, which dynamically adjusts their power output in proportion to the extent of the frequency deviation. This adjustment mechanism is guided by a pre-established droop characteristic, a parameter governing the correlation between frequency deviations and corresponding changes in power output [78].

A notable benefit of the droop control strategy resides in its inherent decentralisation. This design confers upon individual wind turbines the capacity to promptly modify their power output based on locally observed frequency deviations, thereby operating autonomously. Such a control strategy does not require coordination mechanisms and robust communication infrastructure. However, it should be acknowledged that this decentralisation comes at the expense of precision when contrasted with centralised methodologies [79]. Furthermore, the optimal deployment of active power becomes challenging within this framework. It is noteworthy that during the wind turbine's engagement in providing frequency support, the rotor's speed might decelerate, potentially culminating in a frequency second dip [34].

2.6.3.2 De-loading control

Wind turbines can contribute to frequency containment through de-loading control. This strategy focuses on adjusting the power output of wind turbines in response to frequency deviations. De-loading control involves deliberately reducing the power output of wind turbines when the system frequency exceeds its nominal value, and vice versa, increasing the power output when the frequency drops below the nominal value. This control strategy is particularly useful to arrest frequency deviations caused by LoG events, thereby providing an effective mechanism to maintain frequency stability. When the system frequency decreases below the nominal value as a result of an active power deficit, wind turbines employing de-loading control respond by increasing their power output to inject additional energy into the grid. By doing so, they alleviate the power deficit in the system, helping restore the frequency to its desired range [34].

De-loading control does not typically require additional equipment or modifications to the wind turbine's hardware, making it a relatively simple and cost-effective method of frequency regulation. Furthermore, de-loading operation aligns with the Grid Code requirements for frequency containment [53]. This control strategy presents a valuable means of providing frequency containment and grid support. However, during de-loading operation, wind turbines intentionally reduce their power output, which may lead to a decrease in energy production. Careful consideration of the trade-offs between grid stability and energy production is necessary to achieve an effective balance between these aspects [80].

2.6.4 Synthetic inertia

Synthetic inertia replicates the stabilising effect of conventional mechanical inertia provided by SGs [81]. The key is to design control strategies that allow RESs to respond rapidly to frequency deviations. In modern power systems with a high penetration of RESs, synthetic inertia can be emulated through control mechanisms in inverters, energy storage systems, and wind turbines [82, 83]. These devices can be programmed to respond rapidly to frequency deviations by adjusting their power output in a way that mimics the inertial response of SGs. When an LoG event occurs in the system, these devices can temporarily reduce their power output, emulating the behaviour of a spinning generator and providing inertial support [84]. Similarly, if frequency rises,

they can increase their power output to counteract the deviation. The control variable to emulate synthetic inertia is normally the RoCoF [85].

2.6.5 Demand-side response (DSR)

DSR involves adjusting and managing electricity consumption patterns on the consumer side to align with the supply and demand dynamics of the power grid. It allows end-users to modify their electricity usage based on factors such as grid conditions, pricing, or environmental considerations. By doing so, DSR helps create a more balanced and efficient energy system [86].

In terms of supporting frequency, DSR plays a vital role in maintaining the stability of the power system. During operating conditions where there might be power imbalances between generation and consumption, DSR offers a mechanism to either reduce or increase power demand in real-time. When there is excess supply and the system frequency is higher than expected, DSR can increase demand by temporarily connecting non-essential loads or activating energy-consuming processes. This way DSR helps balance the system by utilising the surplus electricity. Conversely, when there is a shortage of supply and the system frequency drops, DSR can strategically reduce demand by tripping loads. This active participation in frequency control aids in preventing large frequency deviations, ensuring that the power system remains within statutory limits [62].

2.6.6 Super-capacitors

Super-capacitors offer a unique energy storage solution that can provide frequency support in modern power systems. They possess the ability to store and release energy rapidly in response to changes in the system frequency, making them valuable assets for addressing short-term frequency deviations [87]. Super-capacitors can discharge their stored energy back into the grid almost instantaneously. This injection of energy helps recover the frequency, preventing it from falling below the statutory limit [38]. Similarly, if the frequency rises unexpectedly due to an excess of generation, super-capacitors can absorb the excess of energy by charging rapidly, assisting in lowering the frequency back within statutory limits.

Super-capacitors present extremely rapid charge and discharge times, enabling them to provide swift and accurate frequency response. These devices have a high cycle life compared to batteries, making them suitable for frequent charge-discharge cycles required for frequency support applications. They exhibit minimal energy loss during charge and discharge processes, contributing to overall system efficiency [74]. The main drawback of super-capacitors is the fact that they have lower energy density compared to traditional batteries, making them more suitable for short-duration frequency support rather than extended energy storage. Over time, the voltage across super-capacitors tends to decrease, leading to potential capacity loss and requiring careful system monitoring and maintenance, in addition to the high cost. The decision to use super-capacitors for frequency support depends on thoroughly considering their pros, cons, and compatibility with the power system's specific requirements [38].

2.7 Dynamic containment capability of RESs

The characteristic capability curve of RESs is distinguished by its distinct trapezoidal form. This shape arises due to a three-phase progression: an initial ramp-up phase, followed by a sustained injection phase congruent with the inherent energy reservoir and culminating in a ramp-down phase leading to the cessation of power injection. This does not imply that the RES injection profile must adhere strictly to a trapezoidal shape. In fact, owing to the capacity of RESs to rapidly adjust their output power setpoints, the RES injection can assume any shape within the trapezoidal capability curve.

As stipulated in [53], the prescribed ramp rates are confined to a maximum of 500 ms for both ascent and descent trajectories. This regulation mandates that RES operations adhere to a criterion of maximum transitioning from the pre-LoG event power setpoint to full injection and, conversely, from full injection to the pre-LoG event power setpoint, within a span of 500 ms. It is noteworthy that these are the maximum boundaries for RES injections, which means that more gradual ramp rates can be established.

In other words, if the maximum ramp rates of the trapezoidal capability curve are not exceeded, there are no constraints on the potential variety of injection shapes. This holds true even in scenarios where the injected power remains below the RES capacity.

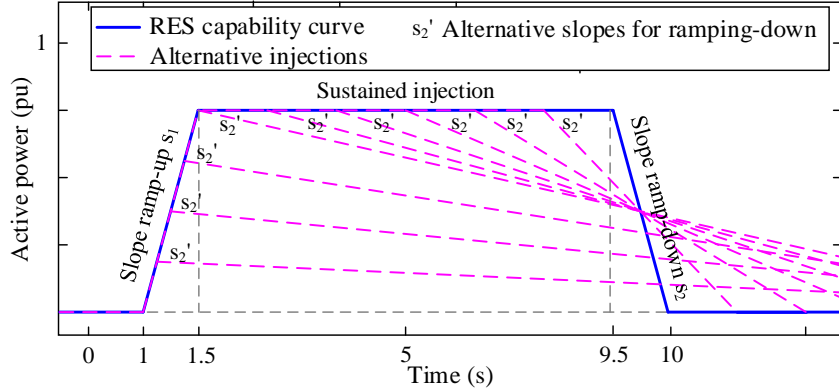


Figure 2.8: RES capability curve.

Adjustments in injection can be made with more gradual ramp rates, enabling power injection that extends well beyond the standard trapezoidal envelope. Figure 2.8 illustrates various alternative injection profiles, with endpoints of injection significantly exceeding the conventional trapezoidal envelope. This is possible due to inherent compliance with ramp-rate constraints, allowing for a gradual decrease in injection until a point of complete attenuation is reached at a pace slower than the specified limit.

Similarly, the ramp-up phase can also be proportionally moderated, thereby furnishing the RES with extended windows for power injection. This dynamic becomes discernible through an examination of the blue trapezoidal form in Figure 2.8. As can be seen, the entirety of the area encompassed under the trapezoidal curve represents the aggregate power delivery potential of the RES across the temporal domain of $t = 1$ to $t = 10$. Consequently, injecting equivalent power quantities through different shapes, without exhaustively covering the entirety of the blue curve’s domain, enables varied power injection intervals. This, in turn, optimises the utilisation of the available RES power.

For illustrative purposes, Figure 2.8 primarily exemplifies distinct ramp-down rates. It is prudent to acknowledge, however, that analogous principles apply to ramp-up rates. The efficacy of such an injection paradigm is presented as the strategic targeting of fast-acting resources in response to LoG events. This operative premise gives rise to the optimal deployment strategy presented in this thesis, where the extra power in-

jection across all RES units contributes to a harmonised and efficient power deployment.

2.8 Chapter conclusions

This chapter bridges the gap between conventional approaches and cutting-edge advancements in frequency control. The chapter introduces the foundations of the SFR model, unravelling the core principles that facilitate accurate calculation and management of frequency deviations following LoG events. Finally, the discourse extends to the study of RESs' capability curves. Through this comprehensive analysis, the chapter not only contextualises the existing practices but also sets the stage for the subsequent elucidation of novel paradigms and transformative strategies in the domain of frequency control.

CHAPTER 3

Detection, location, and size estimation of loss of generation events

3.1 Overview

The increasing penetration of RESs is significantly impacting the performance of traditional control and protection schemes employed in power systems. The early detection and size estimation of LoG events contribute to the timely provision of remedial actions required to preserve the frequency stability of the system. This chapter proposes an effective method for locating and estimating the size of LoG events in power systems with high penetration of RESs. A system of linear equations for every candidate LoG location is formulated based upon KVL and KCL equations. Suitable nodal current sources are employed to model RESs and the candidate tripped generator in the superimposed circuit. The nodal current injections of RESs are estimated based on their power setpoints and available measurements provided by PMUs. The solution of the systems of equations established provides the LoG location and size using the ordinary least-squares (OLS) method. The proposed method is more accurate than existing LoG identification methods that resort to frequency measurements and the knowledge of system inertia. Centralised under-frequency load shedding is presented as a potential application for the proposed method. Extensive simulations conducted on the IEEE 39-bus test system verify the effectiveness and accuracy of the proposed method.

3.2 Identification of loss of generation events

In this section, the formulation for determining the size and location of LoG events in the presence of RESs is put forward. This will be based on the superimposed circuit methodology and requires data routinely available to the control centre, such as the bus impedance matrix of the power system, PMU data, and active and reactive power setpoints of the RESs as input. A system of linear equations is derived for every candidate LoG location and is then solved using the OLS method. The minimum sum of squared residuals (*SoSR*) resulting from the solution of these systems of equations is used to locate the LoG event.

The superimposed circuit methodology essentially concerns disturbances on nodal injections of a circuit with a fixed bus impedance matrix. To be able to apply it, the lost

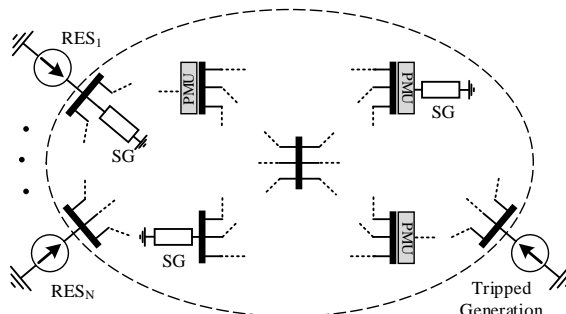


Figure 3.1: Superimposed circuit corresponding to an LoG event [90].

generation is entirely replaced by an unknown current source, as shown in Figure 3.1. This is regardless of whether the lost generation is an SG, an RES, or a combination of both. All other SGs can be safely replaced by their sub-transient impedances in the superimposed circuit within the time frame of interest to this study [88]. The RESs, however, cannot be simply modelled by constant impedances. This is because the equivalent impedance of an RES is not predetermined and depends on many factors. These include pre-LoG voltage and current phasors, which might not be available if there is no PMU at the RES terminal [89]. Therefore, RESs are also replaced by unknown current sources in the superimposed circuit, as depicted in Figure 3.1.

3.2.1 System of equations for each candidate LoG location

Let us consider an LoG event at bus k . The superimposed voltage measured by a PMU at any other bus in the system, e.g., bus w , denoted by ΔV_w^m , satisfies the equation below in each sequence circuit

$$\Delta V_w^m = \sum_{r=1}^N Z_{w,r} \Delta I_r^{RES} + Z_{w,k} \Delta I_k + e_w \quad (3.1)$$

where the superscript “ m ” refers to measured quantities and e_w represents the measurement error. $Z_{w,r}$ is the (w, r) -th entry of the bus impedance matrix, and ΔI_r^{RES} is the superimposed nodal current of the RES at bus r . Besides, ΔI_k denotes the superimposed nodal current of the tripped generation at bus k , and 1 to N are the indices

of the buses to which RESs are connected.

The measured superimposed current of the sending-end of the transmission line $u - w$ in each sequence circuit, denoted by ΔJ_{uw}^m , can be written as a function of the superimposed currents as below

$$\Delta J_{uw}^m = \sum_{r=1}^N C_{uw,r} \Delta I_r^{RES} + C_{uw,k} \Delta I_k + e_{uw} \quad (3.2)$$

where $C_{uw,k}$ is the current transfer coefficient whose derivation is detailed in [88], and e_{uw} is the measurement error. Provided that ΔI_r^{RES} is directly measured by a PMU, the equation below can be established for this measurement

$$\Delta I_r^{m,RES} = \Delta I_r^{RES} + e_r \quad (3.3)$$

Let p denote the number of available synchrophasors provided by PMUs and N be the number of RESs in the power system. For each candidate LoG location, denoted by c , a system of linear equations can be formed in each sequence circuit for the p measurements using their corresponding equations of type (3.1), (3.2), or (3.3) as follows

$$\mathbf{m}_{p \times 1} = \mathbf{H}_{p \times (1+N)}^c \mathbf{x}_{(1+N) \times 1}^c + \mathbf{e}_{p \times 1} \quad (3.4)$$

where \mathbf{m} , \mathbf{H}^c , and \mathbf{e} are the superimposed measurements vector, coefficient matrix corresponding to the location c , and error vector, respectively. The vector of unknowns, denoted by \mathbf{x}^c , contains the superimposed current injections of the candidate tripped generation and all RESs as

$$\mathbf{x}^c = \left[\Delta I_c \quad \Delta I_1^{RES} \quad \dots \quad \Delta I_N^{RES} \right]^T \quad (3.5)$$

The system of equations (3.4) can be solved using the OLS method as follows

$$\hat{\mathbf{x}}^c = \left(\mathbf{H}^{c*} \mathbf{H}^c \right)^{-1} \mathbf{H}^{c*} \mathbf{m} \quad (3.6)$$

where $(\cdot)^*$ denotes the conjugate transpose. The vector $\hat{\mathbf{x}}^c$ contains the estimated un-

knowns corresponding to the location c .

3.2.2 LoG location and size estimation

Identifying the LoG location could be advantageous in preserving the power system's voltage and frequency stabilities. As detailed in [68], the power system's stability can sometimes be preserved only by conducting load shedding in the vicinity of the LoG event. In this subsection, the proposed method for estimating the location and size of LoG events is put forward.

As LoGs are symmetrical events, the system of equations (3.4) is built for the positive-sequence circuit for every candidate LoG location. The objective function of the OLS method is to minimize the *SoSR*. If the measurements were error-free, the *SoSR* would be zero for the tripped generation since all equations in (3.4) hold true with respect to the measurements. In practice, however, the *SoSR* of the tripped generation might be slightly greater than zero due to measurement errors and topology changes [88]. On the contrary, the *SoSR* of other candidates will take non-negligible values as their coefficient matrix does not correspond to the true LoG location. Thus, in this chapter, the candidate LoG location with the smallest *SoSR* is identified as the true LoG location as follows

$$k = \text{Arg} \left\{ \min_{\forall c \in G} \text{SoSR}_c = [\mathbf{m} - \mathbf{H}^c \hat{\mathbf{x}}^c]^* [\mathbf{m} - \mathbf{H}^c \hat{\mathbf{x}}^c] \right\} \quad (3.7)$$

where G is the set of all candidate LoG locations. Once the LoG event has been located, the superimposed current of the tripped generation estimated by (3.6) can be used to estimate the LoG size. The change in the complex power generation at the LoG location, i.e., ΔS_k , can be obtained from

$$\Delta S_k = (V_k^{\text{pre}} + \Delta V_k) (I_k^{\text{pre}} + \Delta I_k)^* - V_k^{\text{pre}} I_k^{\text{pre}} \quad (3.8)$$

Equation (3.8) can be written as

$$\Delta S_k = V_k^{\text{pre}} \Delta I_k^* + \Delta V_k \left(|I_k^{\text{pre}}| e^{-j\varphi} + \Delta I_k^* \right) \quad (3.9)$$

where V_k^{pre} is the pre-LoG voltage at bus k , which is assumed to be known in the control centre through state estimation using existing SCADA and PMU measurements [91]. $|I_k^{\text{pre}}|$ and φ denote the pre-LoG current injection magnitude and power angle at bus k , respectively, which are assumed to be known upon the outage.

3.2.3 Discrimination between faults and LoG events

As explained, the tripped generation is modelled by a nodal current injection at the generation bus. However, a short-circuit fault occurring at that bus can also be represented by a nodal current injection in the same way as was done for the LoG event. Thus, following a short-circuit fault at a generation bus, the minimum *SoSR* calculated by (3.7) will refer to that bus. Therefore, some criteria are needed to differentiate between a fault and an LoG event at a generation bus.

Considering that LoG events only contain positive-sequence components, the presence of considerable negative-sequence quantities in the measurements readily indicates an asymmetrical short-circuit fault in the system. On the other hand, in the case of symmetrical faults at a generation bus, it can be demonstrated that the magnitude of the superimposed nodal current at that bus will always be higher than that of the pre LoG current injection, i.e., $|I_k^{\text{pre}}|$. However, the superimposed nodal current representing an LoG event will always be equal to or less than the pre-LoG current injection. These simple criteria can easily be employed for discriminating faults from LoG events at generation buses.

3.3 Accounting for the presence of RESs

The measured superimposed nodal currents of monitored RESs, i.e., RESs with a PMU at their terminals, can readily be incorporated into the equations of type (3.4) using (3.3). The inclusion of such measured $\Delta I_r^{m,RES}$ in the unknown vector does not create any solvability concerns [92]. This is because every row in the coefficient matrix corresponding to a monitored RES has only one entry equal to one, while all other

entries in that row are zeros. The inclusion of such a row in the coefficient matrix will increase its rank by one [92].

The solution of the system of linear equations (3.4) provides an estimation for the superimposed nodal currents of the candidate tripped generation and all non-monitored RESs (RESs without a PMU at their terminals). However, if the penetration level of RESs is high, the number of unknowns might exceed the number of dependent equations in (3.4), which could make the system unsolvable.

To avoid solvability concerns, the superimposed nodal currents of non-monitored RESs are initially ignored from the unknown vector \mathbf{x}^c . This is to obtain an initial estimation for the superimposed nodal current at each candidate location. This also provides an initial estimate for the superimposed voltages at the terminals of non-monitored RESs based on (3.1). Next, the unknown superimposed current injections of non-monitored RESs can be estimated and included in the corresponding equations. This helps to update the value of the superimposed nodal current representing the candidate tripped generation. This process is continued until the changes resulting from an iteration are negligible, i.e., the changes made in all estimated superimposed nodal current injections are below a pre-specified tolerance of 1×10^{-4} . Finally, the corresponding *SoSR* for each candidate location is calculated to determine the true LoG location. The whole procedure is detailed in the following subsections.

3.3.1 Initial estimations ignoring non-monitored RESs

As described in Section 3.2, every RES is replaced by a suitable current source in the superimposed circuit. The superimposed nodal current of the RES can be directly measured when the RES terminal is equipped with a PMU. However, it may not be possible to have PMUs at certain substations due to budget/infrastructure constraints. Even if all RESs terminals had PMUs, it would not be rational to assume all PMU data are received in time due to the unpredictability of communication latency and the possibility of data losses. Disregarding the superimposed nodal currents of the non-monitored RESs, the system of equations (3.4) is reformed as

$$\mathbf{m}_{p \times 1} = \mathbf{H}_{p \times (1+q)}^{c'} \mathbf{x}_{(1+q) \times 1}^{c'} + \mathbf{e}_{p \times 1} \quad (3.10)$$

where the matrix $\mathbf{H}^{c'}$ contains the coefficients related to the candidate LoG location and the monitored RESs. The vector $\mathbf{x}^{c'}$ is composed of the superimposed nodal current at the candidate location, i.e., ΔI_c , and those of the monitored RESs, respectively. The index q denotes the number of monitored RESs. The system of equations (3.10) can easily be solved using the OLS method as follows

$$\hat{\mathbf{x}}^{c'} = \left(\mathbf{H}^{c'*} \mathbf{H}^{c'} \right)^{-1} \mathbf{H}^{c'*} \mathbf{m} \quad (3.11)$$

where $\hat{\mathbf{x}}^{c'}$ contains the initial estimation of the superimposed nodal current representing the candidate tripped generation and the monitored RESs. Equation (3.10) is solved for every candidate location. Then, using the initial estimation of $\widehat{\Delta I}_c$ and the superimposed currents of the monitored RESs, an initial estimation for the superimposed voltage at all buses can be obtained from (3.1). The superimposed nodal current at the candidate location is updated after incorporating the non-monitored RESs into the formulation, as explained in the following subsection.

3.3.2 Modelling non-monitored RESs

In this subsection, a method is presented to approximate the superimposed nodal currents of the non-monitored RESs. This is accomplished using the pre-LoG active and reactive power of RESs and the estimated superimposed voltages at their terminals. Our assumption in this study is that LoG events do not lead any RES into the low-voltage ride-through (LVRT) operation mode. This means the terminal voltage of none of the RESs drops more than 10% following an LoG event, which is in accordance with the N-1 security criterion. Hence, non-tripped RESs hold the active and reactive power injections equal to the pre-set references according to the relevant grid codes [54, 93].

Let us consider a non-monitored RES connected to bus r . The currents injected by this RES before and after the LoG event can be expressed as follows

$$I_r^{pre} = \frac{(P_{ref} - jQ_{ref})}{(V_r^{pre})^*} \quad (3.12)$$

$$I_r^{post} = \frac{(P_{ref} - jQ_{ref})}{(V_r^{post})^*} \quad (3.13)$$

where I_r^{pre} is the pre-LoG current injection of the RES and P_{ref} and Q_{ref} are the pre-LoG active and reactive power references of the RES. The superscript “post” is used to refer to the post-LoG values. V_r^{post} is calculated using V_r^{pre} and ΔV_r , which are the pre-LoG and superimposed voltages at the RES terminal. The superimposed current of the non-monitored RES can be obtained by subtracting (3.12) from (3.13) as below

$$\Delta I_r^{n,RES} = (P_{ref} - jQ_{ref}) \left(\frac{1}{V_r^{pre} + \Delta V_r} - \frac{1}{V_r^{pre}} \right)^* \quad (3.14)$$

Now, the superimposed nodal currents of non-monitored RESs are included in the vector \mathbf{m} in (3.4) as virtual measurements. Accordingly, the rows related to such superimposed currents are added to the coefficient matrix. As explained, including such a row in the coefficient matrix will increase its rank by one. This eliminates the concerns over the solvability of (3.4) and enables updating the estimation of $\widehat{\Delta I}_c$ by solving (3.6) for every candidate location.

3.3.3 Algorithm for the implementation of the proposed method

The superimposed nodal currents of the tripped generation and non-monitored RESs are estimated and updated through an iterative algorithm to improve the accuracy of the modified set of equations. The convergence of the proposed method requires a minimum of two independent synchrophasors. The termination criterion is defined by the condition that the norm of the difference between the actual estimation of unknowns and the previous estimation must be less than a specified tolerance $\epsilon = 1 \times 10^{-4}$. The flowchart shown in Figure 3.2 can be used for the near real-time implementation of the proposed method. The algorithm represented by this flowchart to identify the LoG location and size is detailed below

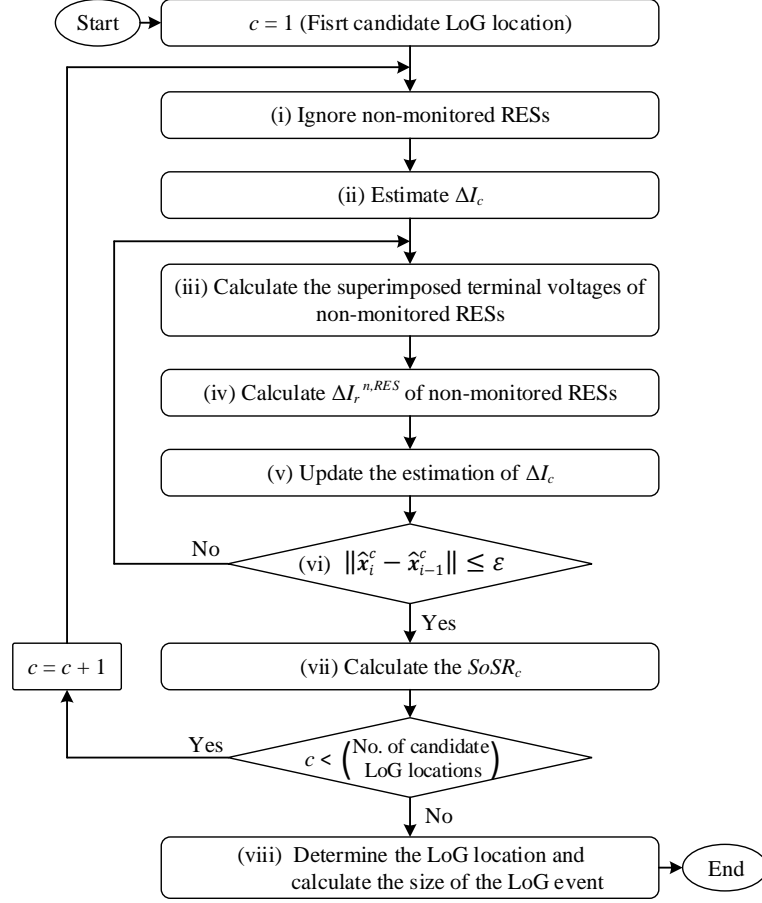


Figure 3.2: Flow chart of the proposed method [90].

- i. All non-monitored RESs are first excluded from the superimposed circuit. This gives rise to (3.10), eliminating the concerns over the solvability of (3.4).
- ii. The solution of (3.10) using (3.11) provides a starting point for the estimation of the superimposed nodal current at the candidate location, i.e., $\widehat{\Delta I}_c$.
- iii. The superimposed voltages at the terminals of non-monitored RESs are obtained from (3.1). In the first iteration, $\widehat{\Delta I}_c$ used for this calculation is taken from step (ii). In the next iterations, $\widehat{\Delta I}_c$ estimated in step (v) of the previous iteration will be utilised.
- iv. The superimposed nodal currents of non-monitored RESs, $\Delta I_r^{n,RES}$, are com-

puted using (3.14). These currents are included in the measurements vector in (3.4) as virtual measurements. Accordingly, the rows representing the equations of type (3.3) for such virtual measurements are added to the coefficient matrix. The superimposed nodal currents of monitored RESs, $\Delta I_r^{m,RES}$, are provided by the corresponding PMU measurement.

- v. The resulting set of equations is solved by (3.6) for the candidate LoG location to update $\widehat{\Delta I}_c$. This calculation accounts for the superimposed nodal currents of all monitored and non-monitored RESs.
- vi. The algorithm goes back to step (iii) to update the superimposed voltages and currents of non-monitored RESs through another iteration. To terminate the process, the most recent estimation of the vector of unknowns, i.e., $\widehat{\mathbf{x}}_i^c$ including all $\Delta I_r^{n,RES}$ and $\widehat{\Delta I}_c$, are compared to that of the previous one, i.e., $\widehat{\mathbf{x}}_{i-1}^c$. If the norm of the difference between $\widehat{\mathbf{x}}_i^c$ and $\widehat{\mathbf{x}}_{i-1}^c$ is less than the specified tolerance, $\epsilon = 1 \times 10^{-4}$, the iteration is terminated and the algorithm goes to step (vii).
- vii. The *SoSR* of the candidate LoG location is computed. Steps (ii) to (vii) are conducted for every candidate location.
- viii. The LoG location is determined using (3.7). Finally, the amounts of the lost active and reactive power are calculated from (3.9), and the algorithm is terminated.

3.4 Study cases

The performance of the proposed method is evaluated in this section using extensive simulations conducted on the IEEE 39-bus test system [94]. First, a general performance evaluation is presented to show the ability of the method to identify the size and location of LoG events considering RESs with different control settings. The outages of both SGs and RESs under different loading conditions are studied. Then, the accuracy of the estimated nodal current injections representing non-monitored RESs during different LoG events is examined. The control settings and locations of RESs summarised in Table 3.1 are considered in subsections 3.4.1, 3.4.2, 3.4.3, and 3.4.4. Next, a comparison study is conducted between the proposed and the existing methods from different viewpoints. The method's sensitivity to measurement, parameter, and topology errors is also investigated. Then, the minimum LoG size the method can detect is scrutinised.

Table 3.1: Settings and Locations of RESs [90].

Location (Bus No.)	Control Settings
1,5,7,9,12,14,15,17,24,26	$S_n = 150\text{MVA}$ $P_{\text{ref}} = 0.9\text{pu}, Q_{\text{ref}} = 0.1\text{pu}$
3,4,8,11,13,16,18,21,27,28	$S_n = 200\text{MVA}$ $P_{\text{ref}} = 0.85\text{pu}, Q_{\text{ref}} = 0.15\text{pu}$

Twelve PMUs are placed at buses 3, 5, 8, 11, 14, 16, 19, 23, 25, 27, 29, and 39 [95]. The impact of different numbers and locations of PMUs on the LoG size estimation is also scrutinised in subsection 3.4.4. Finally, the impact of the RESs penetration is assessed by maintaining the total active power generation of the system while changing the share, location, and control settings of RESs. Note that the method's performance is not impacted by the nature of the load, as it solely identifies changes in the nodal current injection at generation buses.

Extensive time domain simulations are conducted using DIgSILENT PowerFactory. An anti-aliasing Butterworth filter with a cut-off frequency of 400 Hz is used to filter the recorded current and voltage waveforms, which are sampled at a frequency of 2 kHz. Then, the discrete Fourier transform is applied to estimate the phasors of these waveforms. The LoG size is reported as the average of its estimation over one power-frequency cycle. This calculation is performed after a full data window length from the LoG onset to account for the transient response of the phasor estimation process, over which the estimated phasor is not accurate [12].

3.4.1 General evaluation of the proposed method

As listed in Table 3.1, a set of 20 RESs with different settings are connected at random locations in the IEEE 39-bus test system. To demonstrate the performance of the proposed method, two arbitrary outages are examined. The first LoG event is the outage of the SGs connected to bus 33, resulting in the loss of 320 MW active power. The second LoG event is the outage of the RES connected to bus 24, with 135 MW active power injection prior to the event. Figure 3.3 and Figure 3.4 show the *SoSR* of

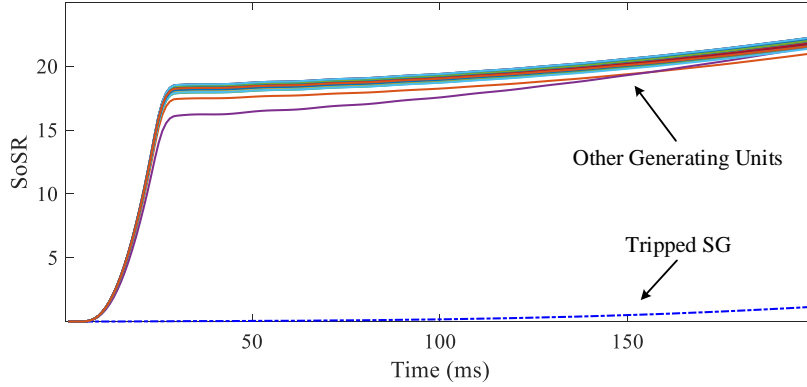


Figure 3.3: $SoSR$ of all candidate LoG locations after the SG outage at bus 33 [90].

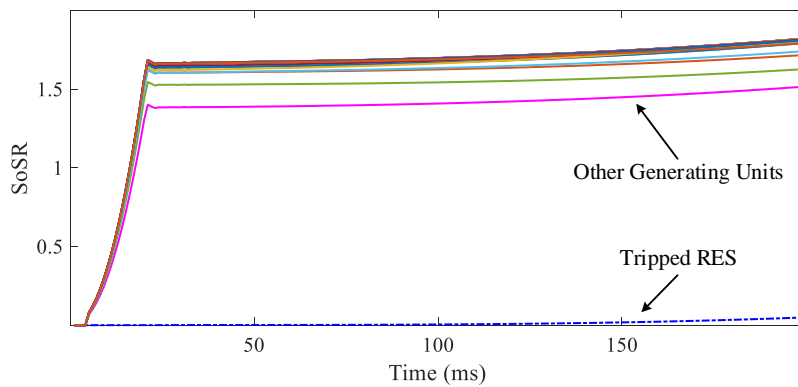


Figure 3.4: $SoSR$ of all candidate LoG locations after the RES outage at bus 24 [90].

all candidate LoG locations for the SGs outage and RES outage, respectively, for up to 200 ms following the LoG event.

In both cases, the $SoSR$ of the tripped generation is the least $SoSR$ amongst the $SoSR$ s calculated for all candidate LoG locations. This confirms the ability of the proposed method to correctly identify the LoG location regardless of whether it is the outage of SGs or RES. Simulation results show that the $SoSR$ index remains valid for identifying the LoG location accurately for up to one second.

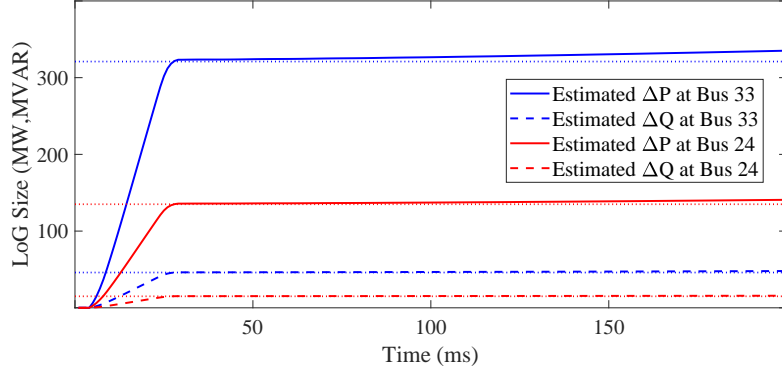


Figure 3.5: LoG size estimation following outages at buses 24 and 33 [90].

Table 3.2: TVE in (%) of the Estimated Superimposed Current of RESs [90].

LoG Event	RESs Location (Bus No.)									
	4	7	12	13	15	17	18	21	26	28
LoG1*	14.2	14.6	14.1	14.9	13.0	13.9	14	13.05	14.8	14.37
LoG2**	12.5	12.1	12.7	12.6	14.0	14.1	14.4	14.4	12.9	12.3

*Outage of SGs connected to bus 33. **Outage of RES connected to bus 24.

Figure 3.5 shows the estimated LoG sizes, i.e., changes in active and reactive power injections, over time for LoG events at the foregoing locations. In this figure, the actual values of ΔP and ΔQ are indicated by dotted lines. It is evident that accurate LoG size estimations can be achieved after one power-frequency cycle from the LoG onset.

Existing methods do not account for the presence of RESs in the system. As expected, these methods become less reliable as the share of RESs increases. The proposed method incorporates the RESs into the formulation by directly adding the superimposed currents of monitored RESs and estimating those of the non-monitored RESs. To show this, the total vector errors (TVEs) between the estimated superimposed currents of the non-monitored RESs and their corresponding true values are reported in percentage in Table 3.2. The TVE index is used to quantify the error between two phasors, which combines the amplitude and phase-angle errors between them [96]. While existing methods disregard the presence of RESs, the maximum TVE for the estimated superimposed currents of RESs with the proposed method is less than 15%. This means the proposed method incorporates the contribution of RESs into the formulation with

Table 3.3: LoG Size Estimation Errors in (%) for SG Outages [90].

Scenario	LoG Location (Bus No.)									
	30	31	32	33	34	35	36	37	38	39
Base-case	0.64	1.52	0.15	1.4	0.06	0.08	0.25	0.01	0.84	0.56
Light-load	0.32	0.11	0.08	1.51	0.07	0.07	0.28	0.01	0.26	0.17
Heavy-load	0.72	1.52	0.14	1.28	0.04	0.16	0.20	0.02	1.12	0.92

Table 3.4: LoG Size Estimation Errors in (%) for RES Outages [90].

Scenario	LoG Location (Bus No.)									
	4	7	12	13	15	17	18	21	26	28
Base-case	0.07	0.68	1.01	1.63	0.01	0.25	0.19	1.50	0.15	0.66
Light-load	0.09	0.63	0.97	1.62	0.02	0.18	0.10	1.61	0.29	0.62
Heavy-load	0.09	0.68	1.03	1.60	0.01	0.35	0.30	1.39	0.03	0.68

an accuracy of more than 85%. As will be shown, estimating the contributions of RESs is quite advantageous for the main objectives of the method, i.e., accurate LoG location and size estimation.

To test the method under different loading conditions, light-load and heavy-load scenarios are created by applying a uniform 50% increase/decrease to all loads/generations in the base case scenario. Table 3.3 and Table 3.4 summarise the percentage errors of the size estimations for LoG events at 30 ms after the LoG onset. It can be seen that the size of the LoG event is accurately estimated in all cases, with errors up to 1.52% and 1.63% for SG and RES outages, respectively. This indicates that the proposed method can accurately estimate the size of LoG events regardless of the loading condition. The estimated LoG size is more accurate if it is performed in the first few cycles following the LoG event instant.

The proposed method can quickly identify the LoG location using a limited number of arithmetic operations. For a linear system of equations of the form (3.4), the vector of measurement residuals r is defined as follows [97]

$$r = m - \hat{m} = S\mathbf{m} \quad (3.15)$$

where S is the residual sensitivity matrix defined as [97]

$$S = I - H(H^*H)^{-1}H^* \quad (3.16)$$

Therefore, the $SoSR$ index expressed by (3.7) can be computed as

$$SoSR = \mathbf{m}^* S^* S \mathbf{m} \quad (3.17)$$

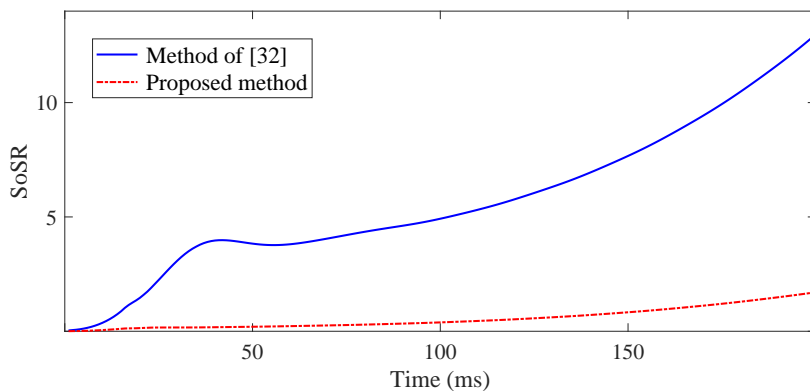
The product S^*S can be calculated and saved in memory offline. The real-time calculation of the $SoSR$ index for each candidate LoG location requires only $p(p+1)$ multiplications and $(p+1)(p-1)$ additions per iteration, where p is the size of the measurements vector. According to the extensive simulations conducted, the average number of iterations taken by the proposed method is 4.5. For the IEEE 39-bus test system with 10 SGs and 20 RESs, the overall computation time amounts to less than 20 ms on a 2.8 GHz processor with 8 GB of RAM. It should be pointed out that the calculations of $SoSR$ s are completely independent of each other. Therefore, in a system with very large numbers of candidate LoG locations, the computational burden can be reduced to the calculation of one $SoSR$ if the calculations are carried out on parallel processors. On the other hand, the effective technique proposed by the authors in [88] can also be used to limit the calculations to the disturbed area only.

3.4.2 Comparison with existing methods

The proposed method's performance is compared with that of other methods in this subsection. The superiority of the proposed method can be seen from Table 3.5, which is not a surprise as the existing methods do not account for the presence of RESs. Furthermore, the majority of existing methods demand full network observability, which requires the reception of a specific set of PMU data to make a decision. The methods that divide the power system into several zones and need extensive offline studies impose a high computational burden. According to Table 3.5, the method presented in [32] has a better performance than the other LoG size/location estimation methods. Therefore, the performance comparison is carried out only between the proposed method and the method of [32].

Table 3.5: Comparison of the Proposed Method with Existing Methods [90].

Reference	[27]	[28]	[30]	[31]	[32]	Prop.
Consider the impact of RESs?	No	No	No	No	No	Yes
Need offline studies?	Yes	Yes	No	No	No	No
Specific sensor locations?	Yes	Yes	Yes	Yes	No	No
Tolerate sensor losses?	No	Yes	No	Yes	Yes	Yes
Estimate both size and location?	No	No	No	Yes	Yes	Yes
Computationally expensive?	Yes	Yes	No	Yes	No	No

Figure 3.6: $SoSR$ of the tripped generation at bus 36 using different methods [90].

As explained, the true LoG location is determined based on the minimum $SoSR$ obtained. Ignoring the presence of RESs by the existing methods introduces inaccuracies into the system model, which results in a higher value for the $SoSR$ of the tripped generation. Simulations show that locating the LoG event by the method of [32] fails in up to 10% of cases with a high penetration of RESs, while the proposed method is 100% successful. This is illustrated by the $SoSR$ s obtained for an arbitrary LoG event at bus 36 with the method of [32] and the proposed method. As shown in Figure 3.6, the $SoSR$ for the true LoG location is noticeably reduced by the proposed method. As shown in Table 3.6, considering the impact of the RESs penetration can also improve the accuracy of LoG size estimation by up to 15%. Furthermore, in contrast to the existing method, the proposed method is able to locate and estimate the size of tripped RESs, which is quite important in modern power systems with high penetration of renewables.

Table 3.6: General Performance of the Proposed Method [90].

LoG Event	Size Estimation Error (%)			
	Proposed method		[32]	
	Ave.	Max.	Ave.	Max.
LoG of SGs	0.55	1.52	7.98	16.81
LoG of RESs	0.33	1.63	N/A	N/A

3.4.3 Sensitivity to measurement, parameter, and topology errors

In this subsection, the proposed method's performance is assessed for a wide range of errors in measurements, generator/transmission line parameters, and topology. The sources of errors considered in measurements are measurement noises, instrument equipment errors, and phasor estimation errors [98]. The errors are assumed to have normal distributions with mean zero. Table 3.7 reports the average and maximum LoG size estimation errors for up to $\pm 5\%$ measurement errors. The variation ranges of errors are reported regarding the three-sigma criterion [88]. In this study, each simulated case is repeated 500 times. With up to 5% errors in the measurements, the size estimation remains highly accurate, with a mean and maximum error of 0.79% and 4.9%, respectively. Besides, the LoG event is successfully located in all simulated cases.

The impact of noise on the method's performance is also studied. In doing so, white Gaussian noise with different signal-to-noise ratios (SNRs) is added to the time domain waveforms. Table 3.8 summarises the results in terms of the average and maximum LoG size estimation error. As can be seen, noise does not have a considerable impact on the robustness of the proposed method. The main reason is that noise is added onto the time domain waveforms, and its impact is significantly reduced through the phasor estimation process, thanks to the antialiasing low-pass filter used and the DFT itself [99]. The promising results obtained can also be partly attributed to the redundancy of the equations and the power of the least-squares method in minimising the overall effect of measurement errors. The results obtained with errors in generator and transmission line parameters are summarised in Table 3.9. Again, each simulated

Table 3.7: Sensitivity to Measurement Errors [90].

Results	Variation Range for Measurement Errors (%)				
	± 1	± 2	± 3	± 4	± 5
Ave. Error (%)	0.46	0.53	0.64	0.71	0.79
Max. Error (%)	1.91	2.38	3.20	4.18	4.90

Table 3.8: Sensitivity to Measurement Noise.

Results	Signal to Noise Ratio (SNR)		
	40 dB	30 dB	20 dB
Ave. Error (%)	0.48	0.69	0.81
Max. Error (%)	1.56	2.98	4.33

case is repeated 500 times. It can be concluded that the method is quite robust to line and generator parameters errors, given the success in LoG location for all cases. As expected, the size estimation accuracy decreases as the parameter errors increase.

The proposed method can function with any given topology so long as the control centre constantly updates the network topology for the correct functioning of the EMS applications [97]. This is to ensure possible changes in the system topology will not adversely impact the method's performance. Nevertheless, if changes in the system topology remain unreported to the control centre, this might lower the method's success rate. In what follows, the method's performance is evaluated against topology errors. Table 3.10 summarises simulation results and demonstrates the impact of topology errors on LoG location and size estimations following LoG events at different locations in the system. It can be seen that the average success rate for the studied cases is 96.6%, while the average size estimation error is around 6.54%. As expected, the topology error (which may, for example, arise due to misreading of the status of an element) reduces the success rate of the LoG location. In this sense, the proposed method is vulnerable to unreliable inputs similar to any other wide-area monitoring, protection, and control methods.

Table 3.9: Sensitivity to Generator/Line Parameter Errors [90].

Variation Range of Errors (%)		± 1	± 2	± 3	± 4	± 5
Error in Gen. Parameters	Ave. Error (%)	0.45	0.45	0.46	0.46	0.47
	Max. Error (%)	1.66	1.70	1.75	1.78	1.83
Error in Line Parameters	Ave. Error (%)	0.45	0.57	0.68	0.84	0.99
	Max. Error (%)	3.28	6.71	7.36	8.73	13.68

Table 3.10: LoG Location and Size Estimation Sensitivity to Topology Errors [90].

Transmission Line/Transformer Index	Success Rate of LoG Location (%)		Ave. Size Estimation Error (%)	
	Not Considered while in service	Considered while not in service	Not Considered while in service	Considered while not in service
5-8	93.01	99.01	9.46	2.83
11-12	96.52	99.21	2.21	4.96
17-18	93.01	98.65	12.89	6.86

System operators can hugely benefit from reliable identification of large LoG events. Therefore, it is also reasonable to define a threshold for the minimum LoG size to be detected by the method. A sensitivity analysis is performed here to evaluate the minimum detectable LoG size at 20 generation buses by considering random measurement errors of 1% and 5% magnitudes, based on the three-sigma criterion [88]. The size of the LoG event is reduced in 2% steps at each certain location, and each simulation case is repeated 500 times to account for the probabilistic nature of errors. The minimum detectable LoG sizes that are successfully located by the proposed method are reported in Figure 3.7.

The proposed method takes advantage of the redundancy of PMU data and the least-squares method to minimise the overall effect of errors. Indeed, the availability of more input measurements improves the method's accuracy [100]. Larger numbers of PMUs will help reduce the minimum detectable LoG size. The minimum detectable LoG sizes are reported in Figure 3.8 for two arbitrary buses 26 and 34. These are obtained for different numbers of PMUs, while measurements are assumed to have up to 1% errors.

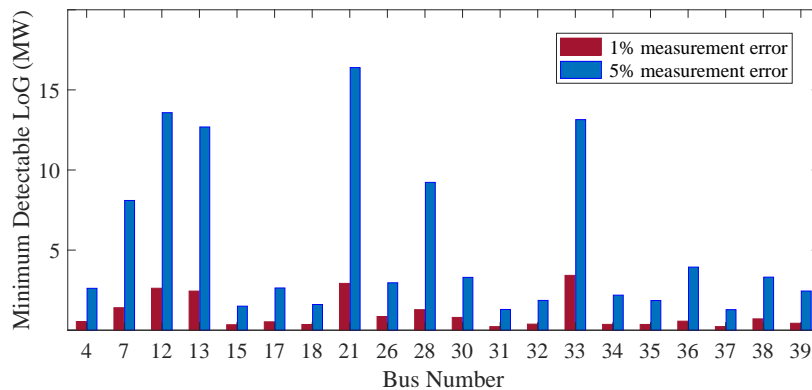


Figure 3.7: Impact of measurement errors on the minimum detectable LoG size [90].

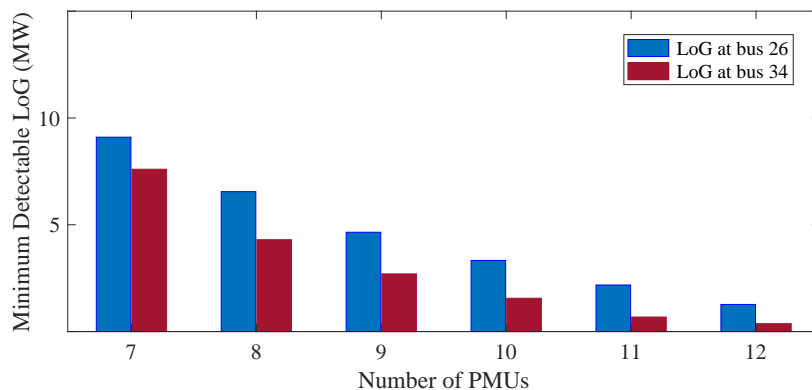


Figure 3.8: Impact of the number of PMUs on the minimum detectable LoG size [90].

3.4.4 Observability and PMU coverage

The proposed method is able to locate and accurately estimate the size of LoG events using a limited number of PMUs. The method does not rely upon a fixed set of PMUs, which means its performance will not be necessarily impacted if some PMU data are lost. Nonetheless, the more the number of input measurements, the more accurate the method becomes [100]. To show this, the proposed method is tested with a different number of PMUs. For each scenario, 100 different PMU placements are considered such that each placement leads to a solvable system of equations with a unique solution. As summarised in Table 3.11, the LoG size is accurately estimated in

Table 3.11: Sensitivity to the Number of PMUs [90].

Results	Number of PMUs				
	12	11	10	9	8
Ave. Error (%)	0.60	0.66	0.70	0.81	0.80

all scenarios. This confirms that the PMU placement does not remarkably affect the method's performance.

3.4.5 Sensitivity to the number and locations of RESs

The proposed method can easily be applied to power systems with different locations and penetration levels of RESs. To demonstrate this, four different penetration levels are considered. The penetration level of RESs in the first column of Table 3.12 is obtained by modifying the control settings reported in Table 3.1. In doing so, the nominal powers of RESs are changed to obtain different injections of active power. For each penetration level, the simulation is repeated 20 times with different numbers and locations of RESs. To comply with this requirement, the different numbers of RESs reported in Table 3.12 are connected to the system at random locations each of the 20 times. All possible RESs locations for each scenario are shown in Figure 3.9. As can be seen, RESs can be connected to any of the 29 buses without SGs. The results presented in Table 3.12 show that the proposed method provides acceptable LoG size estimation regardless of the penetration level, number, and locations of RESs. Increased penetration of RESs adversely affects the existing methods in estimating the LoG size, while this is not the case with the proposed method.

3.4.6 Practical application: Under-frequency load shedding

The proposed method could be incorporated into a centralised UFLS scheme as it can promptly identify the location and size of LoG events. Timely identification of LoG events is advantageous to preserving the power system's stability. This enables the disconnection of loads from the vicinity of the LoG location as early as possible. Here, we compare the performance of a conventional UFLS scheme with that of a centralised

Table 3.12: Sensitivity to Settings, Number, and Locations of RESs [90].

Share of RESs from Generation	Number of RESs	24	20	16	12
40 %	Ave. Size Estimation Error (%)	0.38	0.38	0.40	0.40
50 %		0.39	0.40	0.41	0.44
60 %		0.41	0.45	0.43	0.52
70 %		0.42	0.49	0.45	0.56

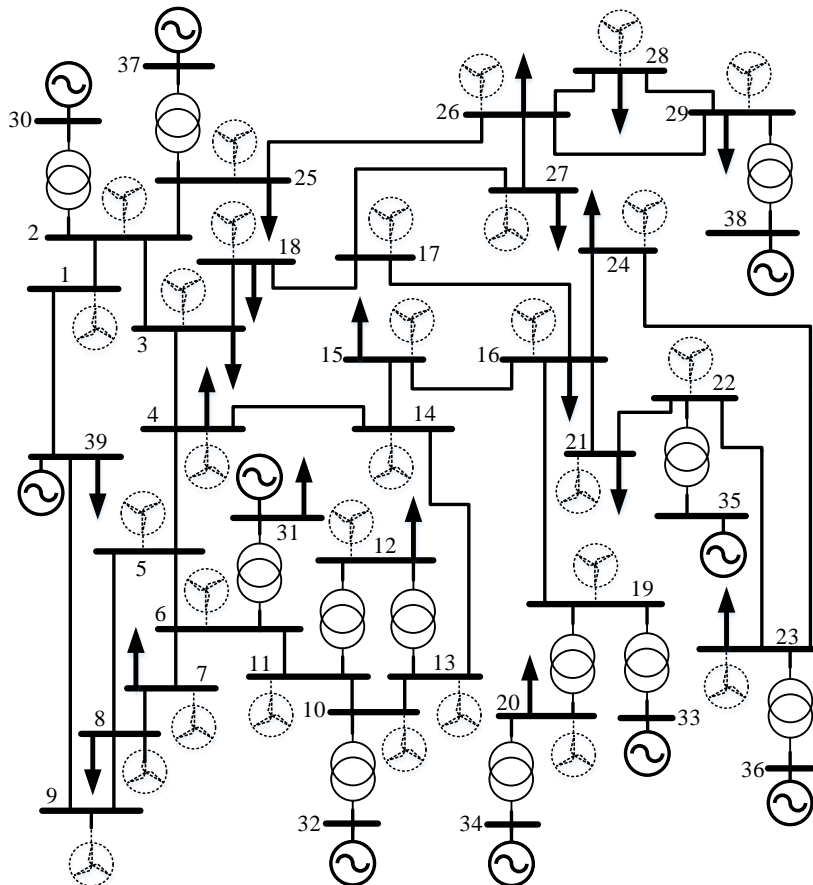


Figure 3.9: Possible RESs locations in the IEEE 39-bus test system.

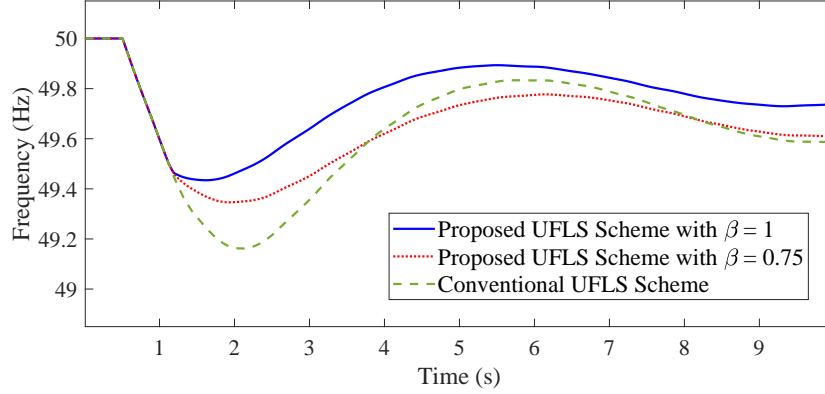


Figure 3.10: Frequency response following UFLS based on different schemes [90].

UFLS scheme by taking advantage of the proposed method. As an example, the LoG event is considered to be the outage of 1200 MW active power. In this example, the RES penetration level is 40%, while the total system inertia is 2.7 seconds. The conventional UFLS scheme is set to shed up to 30% of the total load through 4 steps of 7.5% each. Load shedding is initiated at 49.5 Hz, and the frequency thresholds for each step are set 0.3 Hz apart. Figure 3.10 illustrates the frequency response of the centre of inertia of the system following the LoG event. Thanks to the LoG size estimated, the centralised UFLS scheme can trip a total amount of load equal to the amount of generation lost, i.e., $\beta = 1$ pu. This is accomplished by shedding loads from the vicinity of the LoG event, i.e., buses 3, 4, 7, 8, 15, 20, and 39. It can be seen that the frequency nadir is enhanced by 0.28 Hz compared to the conventional UFLS. By setting $\beta = 0.75$ pu, the proposed scheme sheds the same amount of load as is shed by the conventional scheme. This increases the frequency nadir by 0.2 Hz compared to the latter. These results demonstrate the improvement in the frequency response achieved by the centralised UFLS scheme. Moreover, load shedding from the vicinity of the LoG event could be highly advantageous against combinational voltage and frequency instabilities [68].

3.5 Chapter conclusions

An effective wide-area generation outage monitoring method must be able to reliably identify the size and location of LoG events in a short period of time. The formulation set forth in this chapter is based on the substitution theorem in circuit

theory to enable the modelling of RESs as unknown current sources with no underlying assumptions. The resulting algebraic equations, along with the fact that the sum of squared residuals for a pertinent system of equations must be zero, make it possible to identify both the location and size of LoG events. This is achieved in a short period of time without resorting to differential swing equations. In this context, the salient features of the proposed method and its advantages over existing ones can be summarised as follows

- Addressing the presence of RESs regardless of their penetration level and locations
- Fast decision-making thanks to the independence from frequency/RoCoF measurements
- Accurate estimation of LoG location and size
- Placing no rigid limitations on the PMU number and locations
- Robustness against measurement, parameter, and topology errors

The proposed method might be able to detect the perturbation of sudden load connections if the loads in the system are also replaced by nodal current sources.

CHAPTER 4

Optimal fast frequency containment

4.1 Overview

The increasing penetration of RESs into power systems is reducing the effectiveness of operation, control, and protection schemes traditionally employed to preserve frequency stability. The decoupling of RESs' kinetic energy from the rest of the system and, thus, the variability of system inertia pose a critical challenge to maintaining frequency stability. In this chapter, a new paradigm is set forth for optimal fast frequency containment (OFFC) through a short yet targeted active power injection. This concept builds upon the innovative idea of decomposing frequency response into transient and steady-state deviations. The core aim of OFFC is to reduce or completely remove the transient frequency deviation without unnecessarily changing the settling frequency. This minimises the time and efforts required to restore the frequency within statutory limits while avoiding unnecessary expenditure of turbines' lifetime. Only after allocating enough resources for removing the transient deviation, system operators may utilise the remaining power resources (if any) to reduce the steady-state deviation. The SFR model, technical and operational constraints of RESs, and the loss of generation size are needed as input to formulate the shape, time, and volume of the targeted injection required. This is readily accomplished by applying the inverse SFR model to the frequency correction required. Extensive simulations conducted on the IEEE 39-bus test system verify the effectiveness and reliability of the proposed method for OFFC.

4.2 A new paradigm for optimal fast frequency containment

In this section, the frequency response following an LoG event is decomposed into transient and steady-state frequency deviations. This decomposition is the basis for OFFC, which results in the optimal frequency response with the highest frequency nadir. In doing so, the SFR model [12] is used to establish a link between the available fast-acting injections from RESs and the fraction of the transient frequency deviation that such injections can counteract. It is important to note that the SFR model, derived through CoI calculations, effectively represents the overall frequency dynamics, including RESs. Parameters from SGs not present in RESs do not contribute to the CoI calculation, whereas those available in both SGs and RESs do. This also means that a different SFR model should be derived if the loading/operating conditions change. If

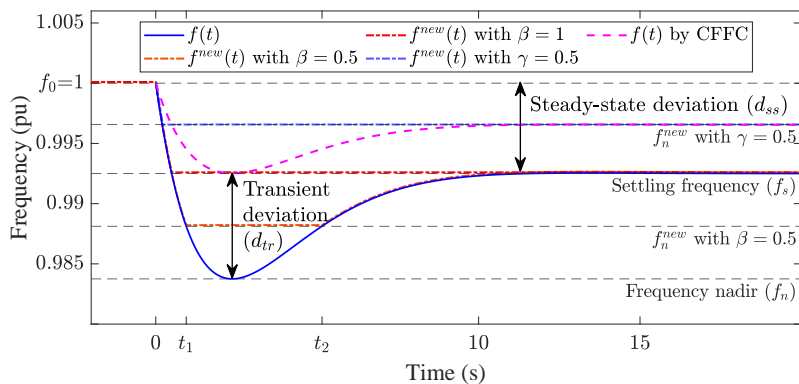


Figure 4.1: Frequency containment by decomposing frequency response into transient and steady-state deviations [101].

appropriately implemented, OFFC ensures that the frequency of the CoI will remain constant for a few seconds and then begin to ascend to the settling frequency. It is assumed that available fast-acting injections from RESs are obtained from different providers, e.g., batteries, HVDC links, synthetic inertia, droop control, de-loading control from wind turbines, etc.

4.2.1 Decomposition of the frequency response

Following an LoG event, the CoI frequency begins and continues to decrease unless the power generation and consumption in the system match again. This equilibrium of power, as described by the swing equation, results in a RoCoF of zero. This is when the frequency response reaches its nadir. On the other hand, the response of turbine governors of SGs increases their power injection. The increase in power generation by SGs helps frequency recover its settling value, which is ideally within statutory limits, as shown in Figure 4.1.

The depth of the frequency deviation can be attributed to the superposition of the depths caused by transient and steady-state components, which are short-lived and permanent, respectively. This decomposition is based on the SFR model, which is a second-order minimum-phase transfer function in its simplified form. Figure 4.1 shows the decomposition of a typical frequency response following an LoG event. Separating transient and steady-state frequency deviations is key to optimal frequency contain-

ment using fast-acting power resources.

The steady-state frequency deviation is defined as the difference between the nominal and settling frequencies. This quantity is determined by the LoG size and the settings of the turbine governors of the remaining SGs [12]. The depth of the transient deviation measures the distance between the settling frequency and the frequency nadir. Failure to promptly mitigate the transient frequency deviation and violating the statutory limits increase the gradual accumulation of irreversible damage in steam turbines. Depending on the extent and duration of the under-frequency condition, the UFLS scheme may also be triggered to arrest the excessive frequency decline and avert the risk of a blackout.

It will be shown in this section that a targeted short-term compensation of the generation deficit will be far more effective/useful in containing system frequency than any constant deployment of available resources of extra power. Indeed, the entire transient frequency deviation can be effectively mitigated when sufficient extra power is delivered by RESs for a short period of time. In cases where the available extra power is not large enough, it can be optimally deployed so as to reduce the depth of the transient frequency deviation as much as possible. This approach results in the highest frequency nadir for any available extra power.

4.2.2 Optimality of the flattened frequency response

The blue curve $f(t)$ in Figure 4.1 is a generic curve demonstrating how the CoI frequency responds to an LoG event and begins to deviate from its nominal value of f_0 . In its trajectory, $f(t)$ drops to a nadir of f_n and then recovers to the settling frequency f_s . In this figure, the depths of transient and steady-state frequency deviations are marked by d_{tr} and d_{ss} and are equal to $f_s - f_n$ and $f_0 - f_s$, respectively. Now, let us assume some extra power is injected such that the desired frequency response $f^{new}(t)$ becomes flattened in part (or from one instance onwards), examples of which are shown by dash-dotted curves in Figure 4.1. Let us define the transient correction β as a real number (between 0 and 1) indicating the portion of the depth of transient frequency deviation that is to be removed by OFFFC. It follows that $\beta = 0$ for the

original frequency response, i.e., frequency response without any correction. The enhanced frequency responses shown in dash-dotted orange and red curves are associated with $\beta = 0.5$ and $\beta = 1$, respectively.

Without loss of generality, the desired frequency response is assumed to be flattened for $t_1 \leq t \leq t_2$ and to coincide with the original frequency response elsewhere. $\Delta p(t)$ is the extra active power injection resulting in the enhanced frequency response whose nadir is denoted by f_n^{new} . Therefore, $E = \int_0^\infty \Delta p(t) dt$ is the net energy required to achieve this enhanced frequency response. It is shown that the energy needed to achieve any frequency response lying above the flattened frequency response (with the same or higher nadirs) is certainly greater than E . The flattened frequency response is considered optimal in the sense that reaching a frequency nadir higher than f_n^{new} requires a larger amount of energy to be injected.

The power system is supposed to be a linear time-invariant system in terms of power-frequency relationship. This is a convenient way of representing the differential equations governing the system frequency dynamics. The average course of the CoI frequency response to changes in generation/load can be approximated by a second-order model that retains enough details without losing essential dynamic characteristics [52]. The LoG size is assumed to be known to the control centre within 0.5 seconds following the LoG inception [32, 90]. Let us use $F(s)$, $P(s)$ and $G_{SFR}(s)$ to denote the frequency response, power disturbance, and SFR transfer function in the Laplace domain, respectively. With these, the frequency can be written as

$$F(s) = P(s) \times G_{SFR}(s) \quad (4.1)$$

where the SFR transfer function can be approximated as [52]

$$G_{SFR}(s) = \left(\frac{R\omega_n^2}{DR + K_m} \right) \left(\frac{1 + T_R s}{s^2 + 2\zeta\omega_n s + \omega_n^2} \right) \quad (4.2)$$

where parameters R , D , K_m , T_R , ζ , and ω_n respectively represent the effects of the governor droop, frequency dependence of load, mechanical gain factor, reheat time constant, damping factor, and natural frequency of the system.

Let $f(t)$, $p(t)$, and $g_{SFR}(t)$ be the time domain functions of the frequency response, power disturbance, and SFR model, respectively. In the time domain, the convolution of the input power and SFR transfer function describes the output frequency as below [102]

$$f(t) = (p * g_{SFR})(t) = f_0 + \int_0^\infty p(\tau)g_{SFR}(t - \tau)d\tau \quad (4.3)$$

where the symbol $*$ represents the convolution operation of two functions and can be seen as a measure expressing how the course of one function is modified by the other one. The convolution of two functions in the time domain is equivalent to the inverse Laplace transform of the product of the Laplace transforms of the two functions [102].

Writing a similar equation as (4.3) for the enhanced frequency $f^{new}(t)$ and subtracting the two equations gives

$$\overbrace{f^{new}(t) - f(t)}^{\Delta f(t)} = \int_0^\infty \overbrace{(p^{new}(\tau) - p(\tau))}^{\Delta p(\tau)} g_{SFR}(t - \tau)d\tau \quad (4.4)$$

where $\Delta f(t)$ is the frequency correction needed to achieve $f^{new}(t)$.

Based on Fubini's theorem and convolution properties, the integral of the convolution of two functions on the whole space is equal to the product of their integrals (each over the whole space) [102, 103]. The original integral limits span from negative to positive infinity. However, the lower limit can be adjusted to 0, knowing that the power system is a causal system in which there cannot be a response prior to the input. Hence,

$$\overbrace{\int_0^\infty \Delta f(t)dt}^{\text{Extent of recovered deviation}} = \overbrace{\int_0^\infty \Delta p(t)dt}^{\text{Injected energy}} \overbrace{\int_0^\infty g_{SFR}(\tau)d\tau}^{R/(DR+K_m)} \quad (4.5)$$

Since $\Delta f(t)$ takes non-zero values only between t_1 and t_2 and is zero otherwise, the lower and upper integral limits in (4.5) can be changed to t_1 and t_2 , respectively. The

left-hand side of (4.5) is the area between the original and enhanced frequency responses. The first integral on the right-hand side of (4.5) represents the energy injected to ensure the intended frequency response. The second integral represents the area under the impulse response of the system. Equation (4.5) is general and can be extended to the removal of all or a portion of the steady-state deviation once the entire d_{tr} is removed. The steady-state correction extent is shown by γ and takes a real value between 0 and 1. A steady-state correction of γ means that γd_{ss} is removed from the steady-state deviation.

4.3 Targeted active power injection

In this section, the extra injection profile is obtained as a function of the LoG size, correction extent, and SFR model. It is shown that this injection is not a step-function but almost triangular, contrary to the LoG event, which is a step reduction in generation. The LoG size is assumed to be available in the control centre by directly monitoring the generator's circuit breakers. Otherwise, it can be estimated using the PMU data received from the wide-area monitoring system [90].

4.3.1 Extra power injection profile

Let us assume the LoG event in per unit can be modelled as a negative step-function with magnitude P . Given the SFR transfer function (4.2), the system frequency in the time domain is obtained to be [12]

$$f(t) = f_0 - \frac{RP}{DR + K_m} \left[1 + \alpha e^{-\zeta \omega_n t} \sin(\omega_r t + \phi) \right] \quad (4.6)$$

where α, ω_r , and ϕ are constants determined based on the SFR model parameters as detailed in [52]. The first two terms on the right-hand side of (4.6) define the settling frequency f_s as below

$$f_s = f_0 - \frac{RP}{DR + K_m} \quad (4.7)$$

The original frequency nadir is obtained by evaluating (4.6) when the frequency derivative becomes zero for the first time at [52]

$$t_n = \frac{1}{\omega_r} \tan^{-1} \left(\frac{\omega_r T_R}{\zeta \omega_n T_R - 1} \right) \quad (4.8)$$

which means $f_n = f(t_n)$. Let us assume that β portion of this transient deviation is to be removed. This means the new frequency nadir is $f_n^{new} = \beta d_{tr} + f_n$, and the enhanced frequency response can be expressed as

$$f^{new}(t) = \begin{cases} f(t) & t < t_1 \text{ and } t_2 < t \\ \beta d_{tr} + f_n & t_1 \leq t \leq t_2 \end{cases} \quad (4.9)$$

This enhanced frequency response is flattened from t_1 to t_2 and coincides with the original frequency response elsewhere. From (4.9), one can easily conclude that t_1 and t_2 are the first and second positive roots of the equation below

$$f(t) - (\beta d_{tr} + f_n) = 0 \quad (4.10)$$

Let $u(t)$ be the unit-step-function occurring at $t = 0$. With the definitions just put forward and based on (4.9), the frequency correction needed is

$$\Delta f(t) = (f_n^{new} - f(t)) (u(t - t_1) - u(t - t_2)) \quad (4.11)$$

The next step is to obtain the extra injection to ensure $f^{new}(t)$ from $\Delta P(s) = \Delta F(s)/G_{SFR}(s)$. By computing the inverse Laplace transform of $\Delta P(s)$, one can easily derive $\Delta p(t)$. Figure 4.2 shows the $\Delta p(t)$ needed for removing 20%, 50%, and 80% of the depth of transient deviation of the frequency response shown in Figure 4.1. It can be easily demonstrated that, in general, the extra injection needed can be approximated with two triangles, regardless of the value of β . For simplicity, the second triangle, which is much smaller, is dropped as this does not significantly impact the enhanced frequency response, as demonstrated in Fig 4.3.

Only when the sum of available resources is sufficient for a complete transient compensation ($\beta = 1$); the remaining power could also be appropriately injected to remove part of the steady-state deviation. In doing so, a similar formulation can be

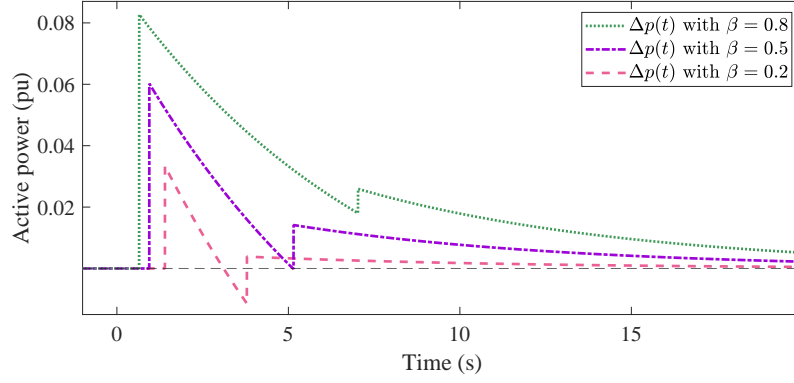
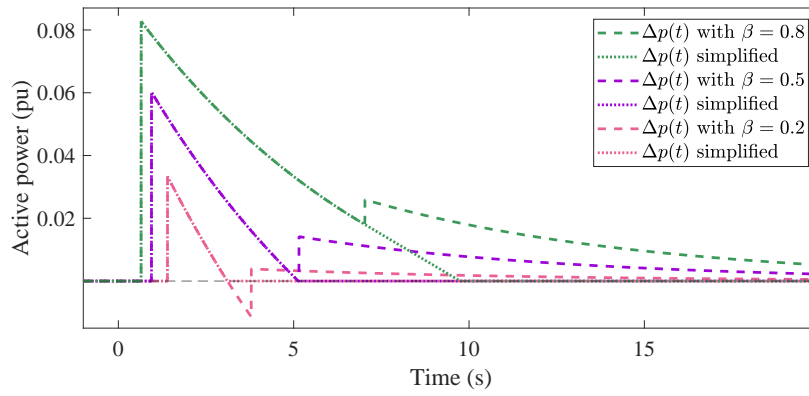
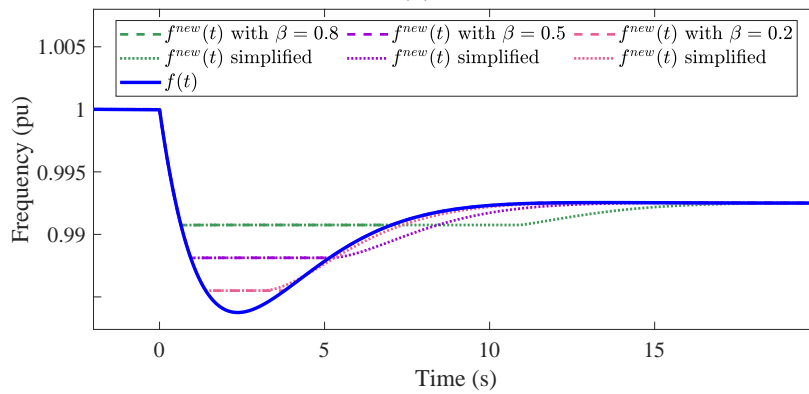


Figure 4.2: Extra injection needed for removing transient frequency deviation [101].



(a)



(b)

Figure 4.3: Impact of (a) Simplified injections on the (b) Correction extent of the frequency response.

derived to correct a fraction of the steady-state frequency deviation depth. As mentioned, γ denotes the portion of the steady-state frequency deviation to be removed after the complete removal of the transient deviation. Since the new frequency nadir is $f_n^{new} = f_s + \gamma d_{ss}$, the enhanced frequency response is

$$f^{new}(t) = \begin{cases} f(t) & t < t_1 \\ f_s + \gamma d_{ss} & t \geq t_1 \end{cases} \quad (4.12)$$

One may desire to flatten the frequency response from t_1 onward if the available resources from RESs exceed the amount needed to recover the entire transient frequency deviation. In these cases, the time to start injecting power is the positive root of the equation below

$$f(t) - (f_s + \gamma d_{ss}) = 0 \quad (4.13)$$

Then, the frequency correction needed is calculated from

$$\Delta f(t) = (f_n^{new} - f(t)) u(t - t_1) \quad (4.14)$$

Again, the extra injection to ensure $f^{new}(t)$ is obtained from $\Delta P(s) = \Delta F(s)/G_{SFR}(s)$. By computing the inverse Laplace transform of $\Delta P(s)$, one can easily derive $\Delta p(t)$.

4.3.2 Individual RESs contribution to the injection profile

The simplified extra injection profile shown in Figure 4.3a, hereafter referred to as the SFR injection profile, produces the highest frequency nadir for a given LoG event. In order to replicate this injection profile in a real power system, various technical characteristics and operational constraints of each RES must be taken into consideration, such as ramp-up and ramp-down rates, pre-LoG active power setpoint P_{ref}^{pre} , and maximum active power setpoint P_{ref}^{max} . For the sake of simplicity, all RES injections are assumed to follow a triangular-shaped pattern. This specific injection pattern can seamlessly align with the ramp rate characteristics of RESs, thereby facilitating and expediting the utilisation of readily available fast-acting resources. The desired injection profile can be achieved through the optimal deployment of RES injections as outlined

below

$$\min \frac{1}{N} \sum_{k=t_1}^{k=t_2} \left(\Delta p(t_k) - \sum_{j \in \mathbf{R}} \Delta p_j^{RES}(t_k) \right)^2 \quad (4.15)$$

subjected to

$$\sum_{j \in \mathbf{R}} \Delta p_j^{RES}(t) \leq |\mathbf{R}| \quad (4.16)$$

$$E - \sum_{j \in \mathbf{R}} \frac{b_j \Delta p_j^{\max}(t)}{2} = 0 \quad (4.17)$$

$$b_j \leq t_2 - t_1 \quad \forall j = 1, \dots, |\mathbf{R}| \quad (4.18)$$

$$P_{\text{ref } j}^{\text{pre}} \leq P_{\text{ref } j} \leq P_{\text{ref } j}^{\max} \quad \forall j = 1, \dots, |\mathbf{R}| \quad (4.19)$$

$$\text{ramp}_j^{\text{up}} \geq 500 \text{ ms} \quad \forall j = 1, \dots, |\mathbf{R}| \quad (4.20)$$

$$\text{ramp}_j^{\text{down}} \geq 500 \text{ ms} \quad \forall j = 1, \dots, |\mathbf{R}| \quad (4.21)$$

where N represents the total number of time samples from t_1 to t_2 , and \mathbf{R} denotes the set of RESs capable of injecting extra active power. The objective function (4.15) seeks to minimise the error between the SFR injection profile and the cumulative extra injection delivered by all participating RESs, denoted as $\Delta p_j^{RES}(t)$ for each individual RES. To ensure the effectiveness and feasibility of the fast-acting power deployment, a set of constraints (4.16) to (4.21) is imposed. Constraint (4.16) guarantees that the total number of extra injections does not surpass the cardinality of the set \mathbf{R} , indicating the maximum number of RESs allowed to participate in frequency containment, represented by $|\mathbf{R}|$. The shape of the extra injections is guided by constraints (4.17) and (4.18), which ensure that the total energy supplied by all triangular injections matches that of the SFR injection profile and that the base (b_j) of each triangular injection remains within the boundaries of the SFR injection profile, respectively. Additionally, technical limitations imposed by the RESs are accounted for through constraints (4.19) to (4.21), which capture the maximum allowable injection and ramp rates of each individual RES.

By formulating the optimisation problem with the objective function and constraints described above, the proposed method seeks to effectively coordinate the contributions of multiple RESs, ensuring that the SFR injection profile is attained while respecting technical and operational limits. The solution to this optimisation problem enables the deployment of fast-acting resources in a manner that efficiently supports the frequency stability of the power system during LoG events.

4.4 Optimal fast frequency containment strategy

In this section, the operational approach for the OFFC strategy is put forward. Following an LoG event, fast-acting resources from RESs can be either optimally allocated, as proposed in previous subsections of this chapter, or deployed according to the guidelines outlined in the Grid Code for the dynamic containment service [53]. This decision relies on how low the new frequency nadir could be for the maximum feasible correction of the frequency deviation. Given the increasing integration of RESs into modern power systems, particularly those with grid-forming operational modes, there is an anticipation of having a sufficient pool of fast-acting resources to mitigate most frequency variations caused by LoG events successfully.

In exceptional cases where the maximum feasible frequency correction leads to a frequency nadir below the frequency threshold to initiate load shedding, LS_{th1} , available fast-acting resources are deployed in alignment with the Grid Code regulations. This deployment serves to contain the frequency within statutory limits. All RESs participating in the dynamic containment service are required to possess the capacity to provide a linear delivery of up to 5% of their total reserve capacity for frequency variations of ± 0.2 Hz considering a dead-band of ± 0.015 Hz from the nominal frequency and up to 100% delivery of their reserves for frequency variations beyond ± 0.2 Hz up to ± 0.5 Hz [53].

The operational strategy of the proposed OFFC presented in Figure 4.4 has the potential to reduce the load shedding measures. By leveraging the swift response of RESs and aligning with Grid Code regulations, this strategy seeks to enhance the stability and reliability of power systems in the face of dynamic frequency challenges.

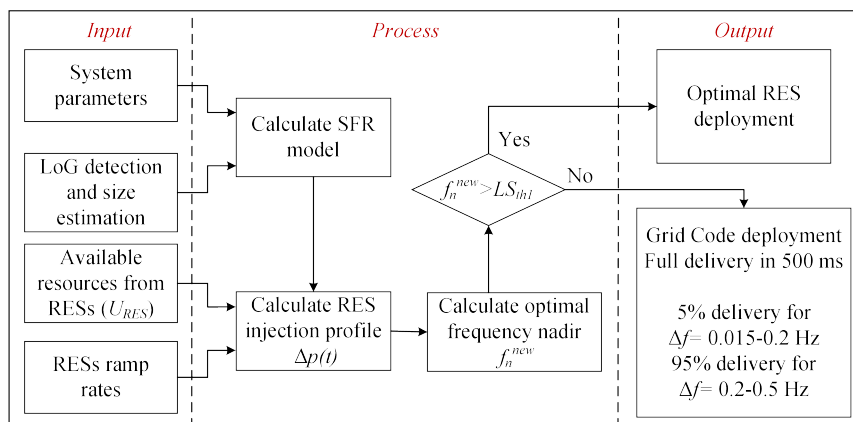


Figure 4.4: Conceptual diagram of the proposed OFFC strategy.

4.5 Study cases

In this section, the effectiveness of the proposed method is evaluated by conducting an extensive number of simulations on the IEEE 39-bus test system in DIgSILENT PowerFactory. A general performance evaluation demonstrates the method's capability to provide OFFC against LoG events considering various control settings for RESs. Then, the effectiveness of the extra injections in maximising the frequency nadir is studied under different loading conditions. Finally, a comparative analysis is conducted between the proposed OFFC and the CFFC methods.

4.5.1 System frequency response model derivation

To evaluate the method's performance, the SFR model of the IEEE 39-bus test system is required. To obtain the SFR model, an offline study is carried out by tripping SGs while RESs are operated in constant power mode. The CoI frequency is then computed for each LoG event, and the Curve Fitting Toolbox of MATLAB is employed to estimate the parameters of (4.2). The average of estimates for each parameter is utilised to derive the representative SFR model of the IEEE 39-bus test system. The SFR model is developed for three different loading conditions. To create each scenario, a 50% increase and decrease are uniformly applied to the load/generation of the base case

Table 4.1: SFR Models for the IEEE 39-Bus Test System [101].

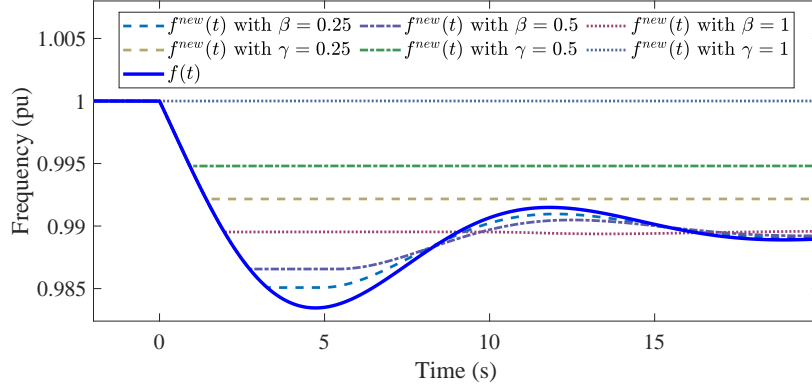
Base case	Light-load	Heavy-load
$\left(\frac{0.015(1+2.15s)}{s^2+0.3s+0.46^2}\right)$	$\left(\frac{0.019(1+1.88s)}{s^2+0.29s+0.49^2}\right)$	$\left(\frac{0.018(1+3.39s)}{s^2+0.38s+0.44^2}\right)$

system. This allows for examining the system’s response under light-load and heavy-load conditions. The SFR models of these scenarios are summarised in Table 4.1.

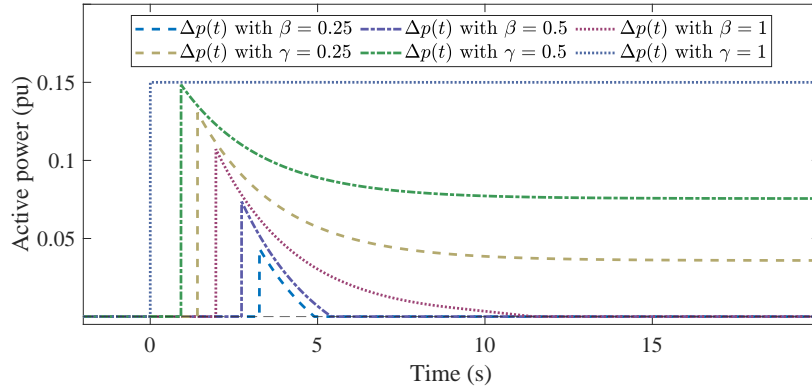
4.5.2 General performance analysis

Twenty randomly distributed RESs are added to the IEEE 39-bus test system. Without loss of generality, all RESs share identical characteristics, including a nominal power rating of 250 MVA, active power setpoint of $P_{ref} = 0.68$ pu, and reactive power setpoint of $Q_{ref} = 0.076$ pu. These settings represent a 50% RES penetration level and serve as the base case. To assess the effectiveness of the proposed method, a 930 MW outage scenario is examined using the base case SFR model reported in Table 4.1. Figure 4.5a shows the enhanced frequency responses where the transient and steady-state frequency deviations are removed to different extents. The corresponding extra injections required to achieve these frequency responses are illustrated in Figure 4.5b. As can be seen, achieving the maximum frequency nadir requires injecting a smaller amount of active power than the size of the LoG event. The targeted injection does not resemble a step-function contrary to the LoG event. The extra injections with non-zero γ consist of two components. The first component is a so-called triangle-shaped injection aimed at removing the entire transient deviation. This is essentially a short-lived energy injection. The second component is a sustained power injection for correcting the corresponding portion of the steady-state deviation.

In compliance with [53], the maximum ramp-up and ramp-down rates of RESs are assumed to be 500 ms. The effect of this on OFFC is evaluated for a 700 MW LoG event. Figure 4.6 shows the frequency response for two different extents of frequency deviation removal. The thick red curve represents the complete removal of the transient deviation, whereas the thick green curve corresponds to the removal of half of the steady-state deviation. The thin curves depict local frequency responses, whose fre-



(a)



(b)

Figure 4.5: Impact of different correction extents on (a) Enhanced frequency response achieved, and (b) Extra power injections required for a 930 MW LoG event [101].

quency nadirs might be slightly lower than that of the CoI frequency. This is because local and inter-area oscillations are averaged out in the CoI frequency. Nevertheless, the CoI frequency is regarded as a valuable tool, for it provides a holistic picture of system frequency behaviour following an LoG event. According to (4.15) to (4.21), Figure 4.7 shows in dotted curves the optimal deployment of single triangular injections from RESs for the complete removal of the transient frequency deviation shown in Figure 4.6, i.e., for $\beta = 1$. The dashed pink curve represents the summation of all dotted curves over the whole period, which matches the SFR injection profile.

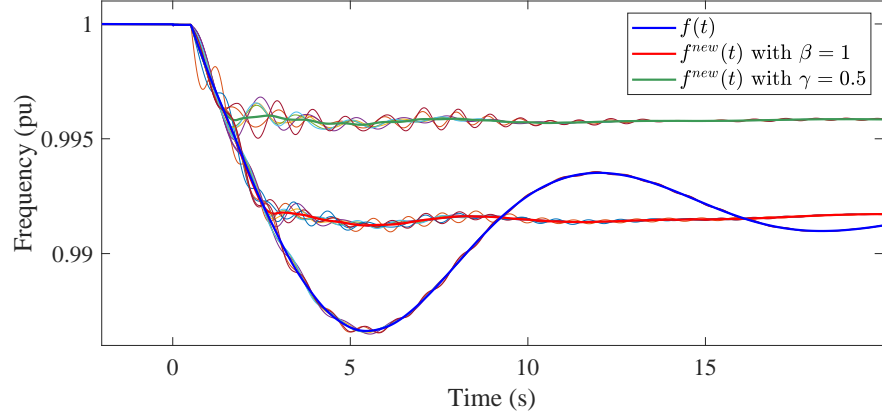


Figure 4.6: Frequency containment following an LoG event of 700 MW [101].

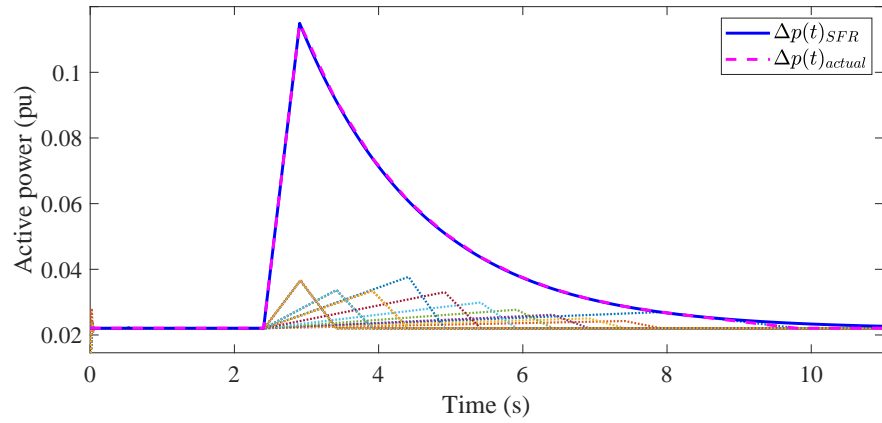


Figure 4.7: Optimal deployment of RES resources for the complete removal of the transient frequency deviation of a 700 MW LoG event.

The proposed method's robustness is assessed by varying RESs numbers, locations, and control settings within a wide range. The increase in RES generation is proportionally deducted from SGs to maintain the total system generation constant. By randomly changing the RES locations, each scenario is simulated 100 times, and the obtained results are averaged. Table 4.2 summarises the CoI frequency nadir for a 600 MW LoG event under different RES penetration levels. The RES injections are targeted at completely removing the transient frequency deviation. As can be seen, the fast-acting contribution of RESs contains the frequency nadir within statutory limits regardless of the penetration level and location of RESs.

Table 4.2: Sensitivity of Frequency Nadir to Settings, Number, and Locations of RESs Following a 600 MW LoG Event [101].

RES Penetration Level	12 RESs	15 RESs	20 RESs	25 RESs
	CoI Frequency Nadir (Hz)			
50%	49.55	49.53	49.57	49.63
60%	49.55	49.59	49.59	49.61
70%	49.51	49.6	49.58	49.62

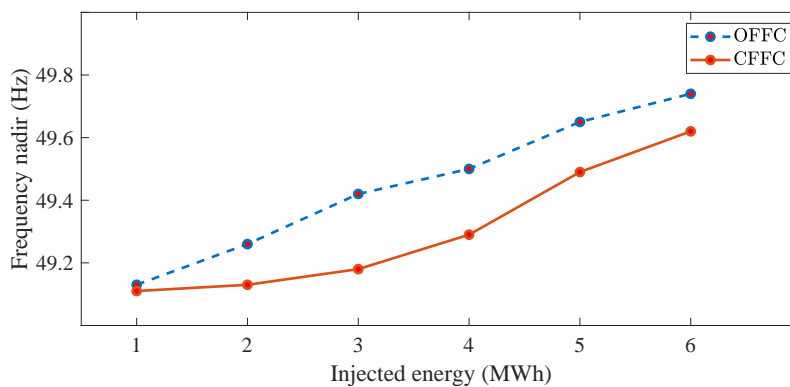


Figure 4.8: Frequency nadir for different injections following a 1000 MW LoG [101].

4.5.3 Comparison of the proposed OFFC with CFFC

In this subsection, the performances of OFFC and CFFC (step power injection) are compared. Figure 4.8 shows the frequency nadir as a function of the total energy injected for a 1000 MW LoG event. As expected, OFFC results in higher frequency nadirs, regardless of the amount of energy injected. Table 4.3 presents the energy required to contain the frequency nadir within statutory limits for 20 seconds. This is carried out for different LoG events, with an RES penetration level of 50%. The results confirm that in comparison with CFFC, OFFC requires significantly less energy to maintain frequency within statutory limits.

Table 4.3: Energy Needed to Contain Frequency within Statutory Limits [101].

LoG Size (MW)	Energy Required (MWh)	
	CFFC	OFFC
600	0.25	0.04
800	1.34	0.29
1000	2.42	1.15
1200	3.51	2.22

4.6 Chapter conclusions

This chapter shows that a step-function active power injection for CFFC is not an optimal solution, for it does not lead to the highest frequency nadir. It is shown that CFFC may even unnecessarily increase the duration required for the frequency to return within statutory limits. A core contribution of this chapter is to highlight the significance of and the need for ensuring the treatment of the transient frequency deviation before focusing on the steady-state frequency deviation. The chapter proposes OFFC as a technique for targeting the extra power injections at delivering the highest possible frequency nadir. OFFC maximises the effectiveness of available resources, as is justified mathematically and verified using extensive simulations. Contrary to common belief in the power systems community, this extra injection should not resemble a step-function and is not even expected to be maintained permanently. Rather it is injected in a specific shape and at a particular time, for it is targeted at removing the transient deviation. OFFC reduces the time to return the frequency within statutory limits without any unrealistic assumptions on the technology readiness or capability of available resources. By capitalising on the fast reaction of RESs and adhering to the stipulations of the Grid Code, the proposed operational strategy for OFFC aims to improve the stability and reliability of power systems with volatile inertia.

CHAPTER 5

Conclusions and final remarks for future work

5.1 Overview

This chapter summarises the contributions of the presented research to the field of electrical power engineering and gives general conclusions and suggestions for future work. Through a comprehensive exploration of frequency stability, loss of generation (LoG) event detection, and optimal fast frequency containment (OFFC), this research lays the foundation for a resilient, adaptable, and efficient power system landscape. As we delve into the conclusions and final remarks, the different layers of understanding and innovation are highlighted, poised to reshape the trajectory of energy systems in the era of exponentially renewable energy deployment.

5.2 Research conclusions

In the pursuit of a global transition towards net-zero power generation, the integration of renewable energy sources (RESs) has introduced a number of operational complexities, arising from their inherent intermittency. These complexities have propelled this research, aimed at solving the critical implications of the high penetration of RESs on frequency stability.

The vulnerability of frequency stability is attributed to the inherent lack of inertia in these generation sources. As RESs introduce limited or negligible inertia to the system, the resultant system inertia becomes remarkably volatile, oscillating across a wide spectrum and manifesting a markedly reduced lower boundary. This, in turn, induces fast frequency dynamics, thereby rendering traditional frequency protection and control practices obsolete.

At the heart of the matter lies the marked increase in the unpredictability and frequency fluctuations following active power imbalances, such as LoG events, rendering traditional assumptions and methodologies progressively invalid. This evolution has the downstream effect of compressing the temporal window available for responding to these critical events. Consequently, the time window for counteracting such incidents has been drastically curtailed, emphasising the urgency of developing novel strategies to restore the active power balance swiftly and effectively.

In light of these exigencies, this research has pioneered a novel method for estimating both the size and location of LoG events in power systems characterised by extensive RESs integration. Distinct from prevailing methods reliant on frequency measurements or the knowledge of system inertia, the proposed method takes advantage of the superimposed circuit methodology, leveraging available PMU data. The elegance of the proposed method lies in its reliance solely on fundamental Kirchhoff's voltage and current laws, rendering it swifter and more accurate than existing alternatives. By deftly manipulating a system of linear equations, the proposed method effectively considers the contributions of RESs, accounting for their impact in scenarios where traditional methods fail. Importantly, the proposed method showcases exceptional accuracy regardless of the penetration and location of RESs, which makes this method a versatile and robust solution for real-world applications.

An equally notable contribution of this research lies in its innovative proposition of a novel paradigm for OFFC. This novel framework decomposes the frequency response into two distinct categories: transient and steady-state frequency deviations. Based on this frequency decomposition, a refined method emerges for determining the optimal size, shape, and timing of additional power injections to maximise the frequency nadir following LoG events. The key point of this method is the targeted allocation of extra power injections. Contrary to conventional wisdom, which endorses step-function injections to counteract events, the research reveals that such an approach is optimal only when the available power resources match the magnitude of the LoG event. The maximum frequency nadir is achieved by targeting initial injections at the elimination of the transient frequency deviation. This manoeuvre optimally employs available energy resources to effect rapid correction of the frequency trajectory. Subsequent allocation of resources towards mitigating steady-state deviations after eliminating transient deviations emerges as a pivotal tactic, bringing the frequency back within the statutory limits with minimal efforts while safeguarding the longevity of steam turbines.

This research also introduces a strategic framework for coordinating the optimal deployment of fast-acting resources from RESs with load shedding. This strategy is aligned with the guidelines stipulated in the Grid Code and aims to maximise the fre-

quency nadir while concurrently reducing load shedding where possible. By precisely managing the extra power injection from RESs, this strategy provides a potential solution to enhance frequency control mechanisms and seeks to enhance the resilience of the power system and mitigate the need for extensive load shedding measures.

This research's revelations extend beyond mere theoretical insights. It gives rise to a profound reconfiguration of our understanding of the interplay between RESs incorporation, frequency stability, and the dynamics of LoG events. Introducing innovative methodologies and challenging conventional assumptions not only advances the theoretical reinforcements of power grid management but also catalyses the evolution of pragmatic methodologies. These methodologies, ready to navigate the complexities of the modern power landscape, bear implications for ensuring the resilience and efficiency of power systems in an era defined by exponentially renewable energy deployment.

5.3 Remarks for future work

Ongoing and future research directions to expand the line of research presented in this thesis are

- To extend the scope of this research, a promising avenue for future exploration involves obtaining analogous outcomes through a decentralised approach. By embracing decentralisation, the study could be expanded to encompass a more distributed framework, thereby offering a comprehensive analysis of the results achieved herein from a distinct point of view.
- To advance the frontiers of research in this domain, a compelling avenue for future investigation is the integration and coordination of both centralised and decentralised approaches in the pursuit of a resilient frequency protection system. By fusing the strengths of these two approaches, an innovative framework could be forged, capable of withstanding challenges such as communication system failures. This holistic exploration holds the promise of developing a comprehensive and adaptive frequency protection system that remains steadfast even in the face of disruptions.

- To pave the way for further advancements, a promising trajectory for future research involves the incorporation of demand-side response (DSR) mechanisms within the optimal fast frequency containment strategy. By assimilating DSR strategies into the framework, the potential arises to align the ideal step injection precisely with the mitigation of transient frequency deviations. This synergistic integration offers an avenue to take advantage of the flexibility of demand-side resources, thereby optimising the efficacy of frequency containment efforts and contributing to the seamless restoration of system equilibrium.
- As the landscape of energy systems continues to evolve, an imperative avenue for future research lies in the integration of cybersecurity considerations. Incorporating cybersecurity measures into the scope of this study would offer a pioneering exploration into the interplay between resilience, stability, and security within modern power grids. Investigating the complex dynamics that arise at the intersection of renewable energy integration and cybersecurity would provide invaluable insights into fortifying power systems against emerging threats and ensuring the longevity of the energy transition.

5.4 Chapter conclusions

This chapter delineates the conclusions drawn from the current research endeavour. It accentuates three significant contributions to the field of electrical power engineering. Firstly, the study addresses the detection, location, and size estimation of LoG events. Secondly, a novel paradigm for OFFC is proposed, aiming to maximise the frequency nadir. Lastly, a strategy is introduced for coordinating the optimal deployment of fast-acting resources from RESs with load shedding, adhering to the guidelines stipulated in the Grid Code. The chapter also outlines research directions for future investigations.

APPENDIX A

Worked example for LoG detection, location and size estimation on the IEEE 9-bus test system

A.1 Overview

This appendix presents a worked example for LoG detection on the IEEE 9-bus test system to help the reader understand how the method works.

A.2 System under study and initial assumptions

The presented worked example is conducted on the IEEE 9-bus test system shown in Figure A.1. As can be seen, the power system is equipped with two PMUs at buses 5 and 9, and two RESs connected to buses 5 and 6. To enable the application of the superimposed circuit methodology, let us assume the bus impedance matrix of the power system, PMU data at buses 5 and 9, and active and reactive power setpoints of the RESs are known. It is crucial to acknowledge that the bus impedance matrix is presumed to remain constant both before and after the LoG event. Additionally, the occurrence of the LoG event does not induce any RES to enter the LVRT operation mode. Consequently, post-LoG event, none of the RES terminal voltages experience a reduction exceeding 10%.

A.3 Identification, location, and size estimation of the LoG event

Let us consider an LoG event occurs at bus 1. The superimposed circuit for this event is shown in Figure A.2. As can be seen, the tripped generation has been replaced by a nodal current source, as well as every RES in the power system. The other SGs are safely replaced by their sub-transient impedance within the time frame of interest, and voltage and current measurements from available PMUs are marked in red. The superimposed nodal currents of the tripped generation (marked in blue) and non-monitored RES at bus 6 are unknown.

Following the algorithm outlined in Section 3.3.3, a specific procedure is adopted for each candidate LoG location to identify and pinpoint the LoG event. This means that the entire procedure is repeated for all SGs and RESs in the system. However, in this

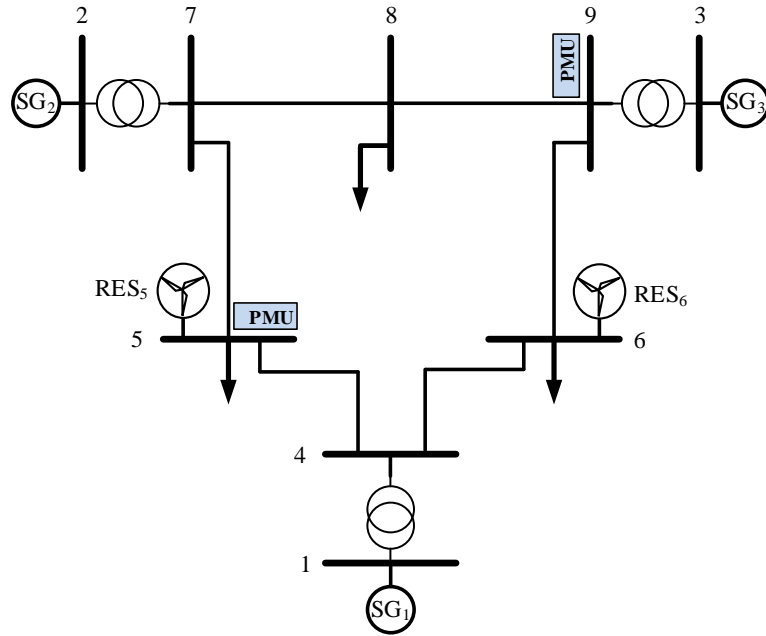


Figure A.1: IEEE 9-bus test system with RES penetration.

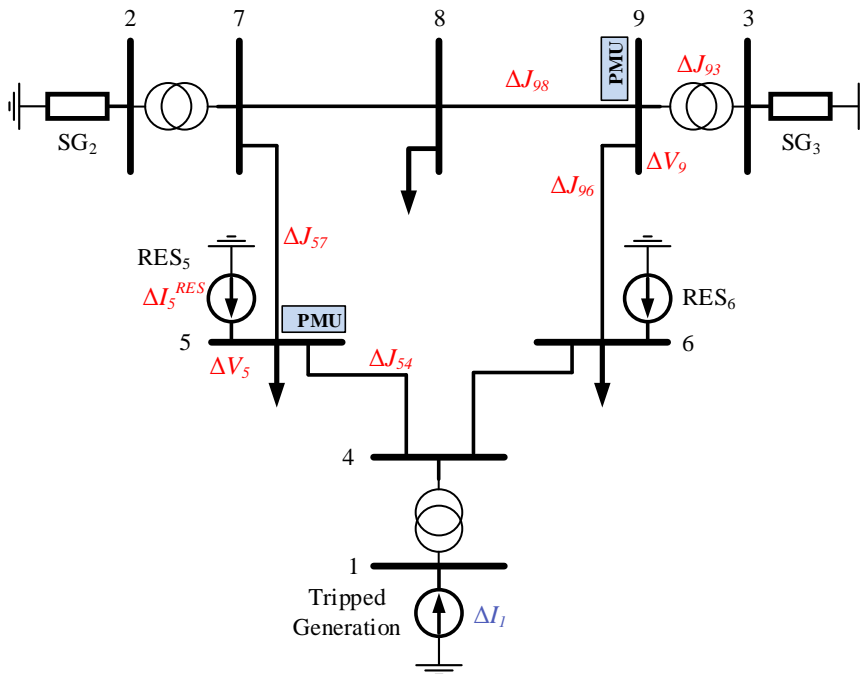


Figure A.2: Superimposed circuit for an LoG event at bus 1.

example, only the procedure for the correct candidate LoG location is illustrated since the purpose is to demonstrate how the LoG event is identified and located. The *SoSR* index for the incorrect candidates will be much larger than zero, while the *SoSR* for the correct candidate should ideally be zero. However, in reality, it remains close to zero due to measurement errors. The procedure for each candidate LoG location is as follows

- i. All non-monitored RESs are first excluded from the superimposed circuit. This gives rise to (A.1), eliminating the concerns over the solvability of (3.4).

$$\underbrace{\begin{bmatrix} \Delta V_5^m \\ \Delta V_9^m \\ \Delta J_{54}^m \\ \Delta J_{57}^m \\ \Delta J_{93}^m \\ \Delta J_{96}^m \\ \Delta J_{98}^m \\ \Delta I_5^{m,RES} \end{bmatrix}}_m = \underbrace{\begin{bmatrix} Z_{5,5} & Z_{5,1} \\ Z_{9,5} & Z_{9,1} \\ C_{54,5} & C_{54,1} \\ C_{57,5} & C_{57,1} \\ C_{93,5} & C_{93,1} \\ C_{96,5} & C_{96,1} \\ C_{98,5} & C_{98,1} \\ 1 & 0 \end{bmatrix}}_{H^{c'}} \underbrace{\begin{bmatrix} \Delta I_5^{RES} \\ \Delta I_1 \end{bmatrix}}_{x^{c'}} + \underbrace{\begin{bmatrix} e_5 \\ e_9 \\ e_{54} \\ e_{57} \\ e_{93} \\ e_{96} \\ e_{98} \\ e_5 \end{bmatrix}}_e \quad (\text{A.1})$$

Note the representation ΔJ_{uw} , which denotes the current at the sending end of the transmission line between terminals u and w . The coefficient C is determined using the distributed-parameter line model, incorporating the line's length, characteristic impedance, propagation constant, and superimposed voltages at the terminals. For a detailed derivation of coefficient C , please refer to [88].

- ii. The solution of (A.1) using (A.2) provides a starting point for the estimation of the superimposed nodal current at the candidate location, i.e., $\widehat{\Delta I}_1$.

$$\widehat{x}^{c'} = \left(\begin{bmatrix} \begin{bmatrix} Z_{5,5} & Z_{5,1} \\ Z_{9,5} & Z_{9,1} \\ C_{54,5} & C_{54,1} \\ C_{57,5} & C_{57,1} \\ C_{93,5} & C_{93,1} \\ C_{96,5} & C_{96,1} \\ C_{98,5} & C_{98,1} \\ 1 & 0 \end{bmatrix}^* \begin{bmatrix} Z_{5,5} & Z_{5,1} \\ Z_{9,5} & Z_{9,1} \\ C_{54,5} & C_{54,1} \\ C_{57,5} & C_{57,1} \\ C_{93,5} & C_{93,1} \\ C_{96,5} & C_{96,1} \\ C_{98,5} & C_{98,1} \\ 1 & 0 \end{bmatrix} \end{bmatrix}^{-1} \begin{bmatrix} Z_{5,5} & Z_{5,1} \\ Z_{9,5} & Z_{9,1} \\ C_{54,5} & C_{54,1} \\ C_{57,5} & C_{57,1} \\ C_{93,5} & C_{93,1} \\ C_{96,5} & C_{96,1} \\ C_{98,5} & C_{98,1} \\ 1 & 0 \end{bmatrix}^* \right) m \quad (\text{A.2})$$

Bear in mind that $\widehat{\Delta I}_1$ is contained in $\widehat{\mathbf{x}}^{c'}$.

- iii. The superimposed voltages at the terminals of non-monitored RESs are obtained from (A.3). In the first iteration, $\widehat{\Delta I}_1$ used for this calculation is taken from step (ii). In the next iterations, $\widehat{\Delta I}_1$ estimated in step (v) of the previous iteration will be utilised. As this is the first iteration, $\widehat{\Delta I}_1$ just calculated in the previous step is employed.

$$\Delta V_6 = Z_{6,5}\Delta I_5^{RES} + Z_{6,1}\widehat{\Delta I}_1 \quad (\text{A.3})$$

- iv. The superimposed nodal currents of non-monitored RESs, $\Delta I_6^{n,RES}$, are computed using (A.4). These currents are included in the measurements vector in (A.5) as virtual measurements. Accordingly, the rows representing the equations of type (3.3) for such virtual measurements are added to the coefficient matrix. The superimposed nodal currents of monitored RESs, $\Delta I_r^{m,RES}$, are provided by the corresponding PMU measurement.

$$\Delta I_6^{n,RES} = (P_{\text{ref}} - jQ_{\text{ref}}) \left(\frac{1}{V_6^{\text{pre}} + \Delta V_6} - \frac{1}{V_6^{\text{pre}}} \right)^* \quad (\text{A.4})$$

$$\underbrace{\begin{bmatrix} \Delta V_5^m \\ \Delta V_9^m \\ \Delta J_{54}^m \\ \Delta J_{57}^m \\ \Delta J_{93}^m \\ \Delta J_{96}^m \\ \Delta J_{98}^m \\ \Delta I_5^{m,RES} \\ \Delta I_6^{n,RES} \end{bmatrix}}_m = \underbrace{\begin{bmatrix} Z_{5,5} & 0 & Z_{5,1} \\ Z_{9,5} & 0 & Z_{9,1} \\ C_{54,5} & 0 & C_{54,1} \\ C_{57,5} & 0 & C_{57,1} \\ C_{93,5} & 0 & C_{93,1} \\ C_{96,5} & 0 & C_{96,1} \\ C_{98,5} & 0 & C_{98,1} \\ 1 & 0 & 0 \\ 0 & 1 & 0 \end{bmatrix}}_{H^c} \underbrace{\begin{bmatrix} \Delta I_5^{RES} \\ \Delta I_6^{RES} \\ \Delta I_1 \end{bmatrix}}_{x^c} + \underbrace{\begin{bmatrix} e_5 \\ e_9 \\ e_{54} \\ e_{57} \\ e_{93} \\ e_{96} \\ e_{98} \\ e_5 \\ 0 \end{bmatrix}}_e \quad (\text{A.5})$$

- v. The resulting set of equations is solved by (A.6) for the candidate LoG location to update $\widehat{\Delta I}_1$. This calculation accounts for the superimposed nodal currents of

all monitored and non-monitored RESs.

$$\hat{\mathbf{x}}^c = \left(\begin{bmatrix} \mathbf{Z}_{5,5} & \mathbf{0} & \mathbf{Z}_{5,1} \\ \mathbf{Z}_{9,5} & \mathbf{0} & \mathbf{Z}_{9,1} \\ \mathbf{C}_{54,5} & \mathbf{0} & \mathbf{C}_{54,1} \\ \mathbf{C}_{57,5} & \mathbf{0} & \mathbf{C}_{57,1} \\ \mathbf{C}_{93,5} & \mathbf{0} & \mathbf{C}_{93,1} \\ \mathbf{C}_{96,5} & \mathbf{0} & \mathbf{C}_{96,1} \\ \mathbf{C}_{98,5} & \mathbf{0} & \mathbf{C}_{98,1} \\ 1 & 0 & 0 \\ 0 & 1 & 0 \end{bmatrix}^* \begin{bmatrix} \mathbf{Z}_{5,5} & \mathbf{0} & \mathbf{Z}_{5,1} \\ \mathbf{Z}_{9,5} & \mathbf{0} & \mathbf{Z}_{9,1} \\ \mathbf{C}_{54,5} & \mathbf{0} & \mathbf{C}_{54,1} \\ \mathbf{C}_{57,5} & \mathbf{0} & \mathbf{C}_{57,1} \\ \mathbf{C}_{93,5} & \mathbf{0} & \mathbf{C}_{93,1} \\ \mathbf{C}_{96,5} & \mathbf{0} & \mathbf{C}_{96,1} \\ \mathbf{C}_{98,5} & \mathbf{0} & \mathbf{C}_{98,1} \\ 1 & 0 & 0 \\ 0 & 1 & 0 \end{bmatrix} \right)^{-1} \begin{bmatrix} \mathbf{Z}_{5,5} & \mathbf{0} & \mathbf{Z}_{5,1} \\ \mathbf{Z}_{9,5} & \mathbf{0} & \mathbf{Z}_{9,1} \\ \mathbf{C}_{54,5} & \mathbf{0} & \mathbf{C}_{54,1} \\ \mathbf{C}_{57,5} & \mathbf{0} & \mathbf{C}_{57,1} \\ \mathbf{C}_{93,5} & \mathbf{0} & \mathbf{C}_{93,1} \\ \mathbf{C}_{96,5} & \mathbf{0} & \mathbf{C}_{96,1} \\ \mathbf{C}_{98,5} & \mathbf{0} & \mathbf{C}_{98,1} \\ 1 & 0 & 0 \\ 0 & 1 & 0 \end{bmatrix}^* \mathbf{m} \quad (\text{A.6})$$

The solution of (A.6) provides an updated value for $\widehat{\Delta I}_1$.

- vi. The algorithm goes back to step (iii) to update the superimposed voltages and currents of non-monitored RESs through another iteration, i.e., it recalculates from (A.3) to (A.6) using the last estimated value of $\widehat{\Delta I}_1$ to obtain an updated and more accurate value for $\widehat{\Delta I}_1$. This process is maintained until the most recent estimation of the vector of unknowns, i.e., $\hat{\mathbf{x}}_i^c$ including all $\Delta I_6^{n,RES}$ and $\widehat{\Delta I}_1$, is compared to that of the previous one, i.e., $\hat{\mathbf{x}}_{i-1}^c$. If the norm of the difference between $\hat{\mathbf{x}}_i^c$ and $\hat{\mathbf{x}}_{i-1}^c$ is less than the specified tolerance, $\epsilon = 1 \times 10^{-4}$, the iteration is terminated and the algorithm goes to step (vii). Let us say that for the worked example, the termination criterion is satisfied after a couple of iterations.
- vii. The *SoSR* of the candidate LoG location is computed. Steps (ii) to (vii) are conducted for every candidate location. For the worked example, it is only shown the process for the correct candidate LoG location. For the other candidates, the procedure is identical as the one shown in this example. Once all candidates have been evaluated, the *SoSR* index is computed for each one of them. This means that there will be as many *SoSR* indices as candidate LoG locations.
- viii. The LoG location is determined using (A.7).

$$k = \text{Arg} \left\{ \min_{\forall c \in \mathbf{G}} \text{SoSR}_c = [\mathbf{m} - \mathbf{H}^c \hat{\mathbf{x}}^c]^* [\mathbf{m} - \mathbf{H}^c \hat{\mathbf{x}}^c] \right\} \quad (\text{A.7})$$

The *SoSR* of the of the correct candidate LoG location is ideally zero since all the equations hold true with respect to the measurements. In practice, however,

the *SoSR* is almost zero due to measurement errors. On the other hand, all other *SoSR* will take non-negligible values.

- ix. Finally, the amounts of the lost active and reactive power are calculated from (A.8), and the algorithm is terminated.

$$\Delta S_1 = V_1^{\text{pre}} \Delta I_1^* + \Delta V_1 \left(|I_1^{\text{pre}}| e^{-j\varphi} + \Delta I_1^* \right) \quad (\text{A.8})$$

Appendix A. Worked example for LoG detection, location and size estimation on the IEEE 9-bus test system

APPENDIX B

RES modelling

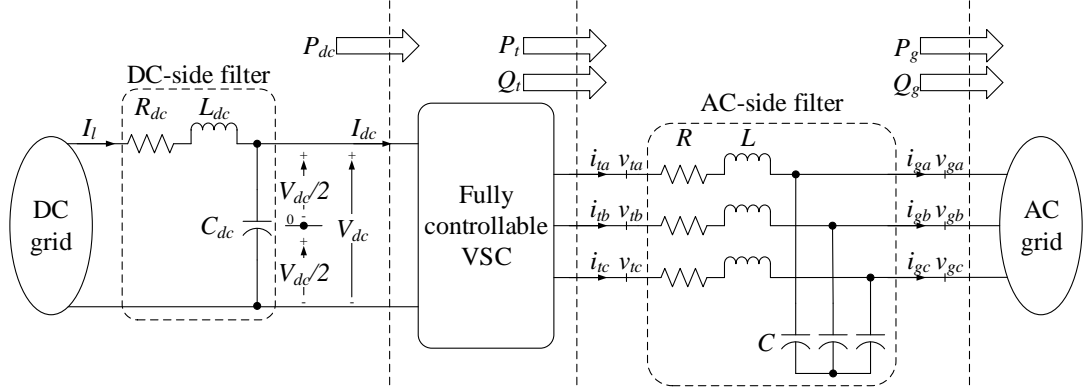


Figure B.1: Generic model for the RES [104].

B.1 Overview

The purpose of this appendix is to provide a clear explanation of how the RES model used in this project works. The model was developed by a colleague from the WAMPAC research group at the University of Leeds. This model has been modified to account for optimal fast frequency containment. Modifications to the model concerning OFFC have been carried out by the author of the present research work.

B.2 Voltage source converter

In this research work, the type of RES is not of interest as its particular behaviour is not relevant to the purpose of this project. Regardless of whether it is a solar panel, wind turbine, battery energy storage system, etc., this project focuses on the availability of fast-acting resources to support the frequency response during under-frequency excursions. For this reason, it is feasible to model RESs by fully controllable voltage source converters (VSCs). A VSC is connected to a DC grid at one end and to an AC grid at the other end, as shown in Figure B.1. This enables a bidirectional transfer of energy from the renewable power source to the DC-to-AC converter connected to the grid. The switching functionalities of the VSC are performed through PE-based devices. This allows fast switching strategies compared to SGs, which permit faster control of the power output of RESs.

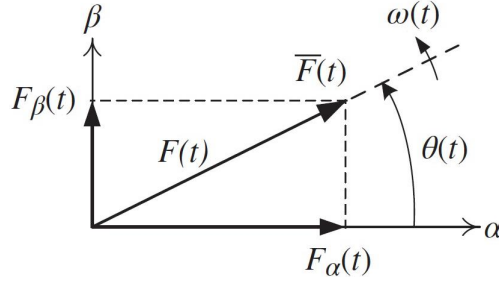


Figure B.2: Space phasor in the stationary dq-frame [104].

VSCs are primarily managed by manipulating the active and reactive power (P_g and Q_g) of the AC grid. This manipulation is achieved through control strategies, which can be either voltage-mode or current-mode approaches. Among these, the current-mode control strategy is often favoured due to its ability to protect the VSC from over-currents by limiting the current ($i_{t,abc}$). This approach relies on measurements of grid voltage ($v_{g,abc}$) and terminal current ($i_{t,abc}$) to regulate P_g and Q_g . Specifically, the current ($i_{t,abc}$) is adjusted based on the terminal voltage of the VSC ($v_{g,abc}$). Notably, the internal control mechanism of switching devices is not examined here, as their response time is significantly faster than those studied in this project.

B.3 dq-frame transformation

In a two-axis stationary frame, the spatial representation of three arbitrary waveform signals denoted as $f_a(t)$, $f_b(t)$, $f_c(t)$, all possessing a zero-sum characteristic, can be expressed in the following manner

$$\bar{F}(t) = F_\alpha(t) + jF_\beta(t) \quad (\text{B.1})$$

where

$$\begin{bmatrix} F_\alpha(t) \\ F_\beta(t) \end{bmatrix} = \frac{2}{3} \begin{bmatrix} 1 & -\frac{1}{2} & -\frac{1}{2} \\ 0 & \frac{\sqrt{3}}{2} & -\frac{\sqrt{3}}{2} \end{bmatrix} \begin{bmatrix} F_a(t) \\ F_b(t) \\ F_c(t) \end{bmatrix} \quad (\text{B.2})$$

Equation (B.2) can be visually represented in a complex stationary plane, as depicted in Figure B.2.

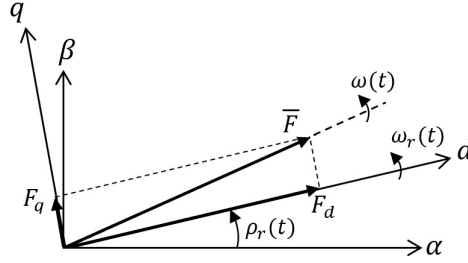


Figure B.3: Space phasor in the rotatory dq-frame [104].

where $\theta(t)$, $\omega(t)$, and $F(t)$ refer to the instantaneous phase angle, frequency, and magnitude of the three-phase signals, respectively [104]. The space phasor of a balanced three-phase sinusoidal signal undergoes rotation at an instantaneous angular velocity of $\omega(t)$ in the $\alpha\beta$ frame while maintaining a constant magnitude. Consequently, its projections on the α and β axes exhibit oscillations over time. Figure B.3 introduces a Cartesian frame rotating at the instantaneous angular velocity, $\omega_r(t)$. Setting $\omega_r(t)$ equal to the instantaneous angular velocity of $\bar{F}(t)$ ensures that the projections of the phasor on the orthogonal axes of the rotating dq-frame remain time-invariant.

The benefit of the two-dimensional dq-frame lies in its efficacy for transforming the challenge of controlling three sinusoidal waveforms into the task of regulating two DC signals. In this context, the connection between the projection of $\bar{F}(t)$ onto the orthogonal axes of both stationary and rotating reference frames in the positive sequence network is shown through the Park transformation, as below

$$\begin{bmatrix} F_d^p \\ F_q^p \end{bmatrix} = \begin{bmatrix} \cos(\rho_r(t)) & \sin(\rho_r(t)) \\ -\sin(\rho_r(t)) & \cos(\rho_r(t)) \end{bmatrix} \begin{bmatrix} F_\alpha^p(t) \\ F_\beta^p(t) \end{bmatrix} \quad (\text{B.3})$$

In addressing the negative sequence network, we introduce an additional rotating reference frame that rotates clockwise at the identical angular velocity, $\omega_r(t)$. The correlation between the projection of $\bar{F}(t)$ in the negative sequence network and its alignment with the orthogonal axes of both stationary and rotating reference frames can be expressed as follows

$$\begin{bmatrix} F_d^n \\ F_q^n \end{bmatrix} = \begin{bmatrix} \cos(\rho_r(t)) & -\sin(\rho_r(t)) \\ \sin(\rho_r(t)) & \cos(\rho_r(t)) \end{bmatrix} \begin{bmatrix} F_\alpha^n(t) \\ F_\beta^n(t) \end{bmatrix} \quad (\text{B.4})$$

This research explores the dynamic characteristics of PE-based RESs with a focus on protective functionalities. To achieve this objective, terminal voltage and current phasors are analysed in both positive and negative sequence dq-frames. This approach facilitates the establishment of decoupled control loops for active and reactive power, allowing for effective control under various grid conditions. The expressions for active and reactive powers in the dq rotating frame of a balanced three-phase system are derived as follows [104]

$$P = \frac{3}{2} (V_d I_d + V_q I_q) \quad (\text{B.5})$$

$$Q = \frac{3}{2} (-V_d I_q + V_q I_d) \quad (\text{B.6})$$

By manipulating the AC-side current components, I_d and I_q , P and Q of the RES can be regulated based on the grid voltage components, V_d and V_q . However, it is noteworthy that V_q becomes zero when the d-axis of the rotating dq-frame is aligned with the voltage waveform of phase A. As a result, equations (B.5) and (B.6) can be simplified as follows

$$P = \frac{3}{2} V_d I_d \quad (\text{B.7})$$

$$Q = -\frac{3}{2} V_d I_q \quad (\text{B.8})$$

To obtain a fundamental understanding of the decoupled control strategies, let us assume that V_d is 1 pu. Consequently, by referring to equations (B.5) and (B.6), the active and reactive powers of an RES can be independently regulated. This is achieved by adjusting the injected I_d and I_q at the point of common coupling (PCC). Initially, the current and voltage waveforms in the stationary $\alpha\beta$ frame are decoupled into positive and negative sequence components, as illustrated in Figure B.4. The entire process of decomposing a time-domain three-phase signal into positive and negative sequence d- and q-components, as outlined in equations (B.3) and (B.4), is shown in Figure B.5 [105].

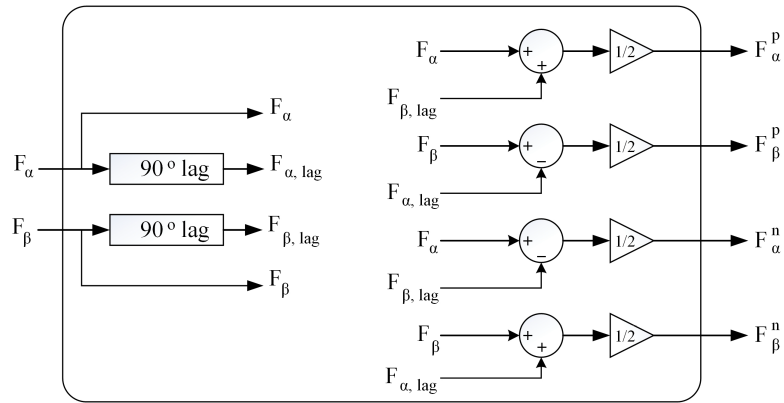


Figure B.4: Decomposition of positive and negative sequences [104].

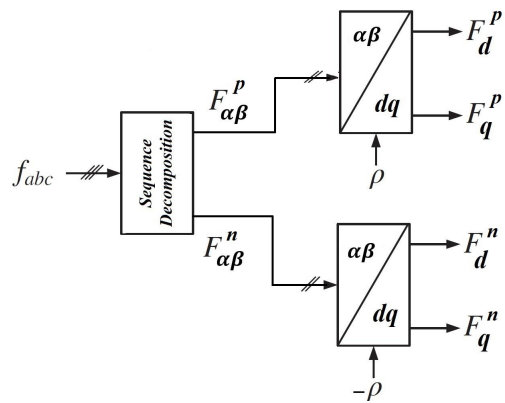


Figure B.5: Decomposition of a time domain three-phase signal into positive and negative sequence d- and q-component [106].

B.4 Inner current control

To develop a robust inner current controller for the RES in the dq-frame, it is essential to initially derive the control plant that characterises the dynamics of the AC-side current in this frame. The expression for the AC-side of the system in the dq-frame for each positive and negative sequence network in Figure B.1 is obtained as follows [104]

$$L \frac{dI_{td}}{dt} = -RI_{td} + L\omega I_{tq} + V_{td} - V_{gd} \quad (\text{B.9})$$

$$L \frac{dI_{tq}}{dt} = -RI_{tq} + L\omega I_{td} + V_{tq} - V_{gq} \quad (\text{B.10})$$

As shown in Figure B.6, equations (B.9) and (B.10) delineate a dynamic system where V_{td} and V_{tq} serve as inputs, V_{gd} and V_{gq} act as disturbance inputs, and I_{td} and I_{tq} function as outputs. The control inputs, V_{td} and V_{tq} are generated through a switching strategy involving two other control variables, m_d and m_q .

In the control systems of RESs, the manipulation of terminal voltage is indirectly achieved by controlling over d- and q-axis terminal current. In simpler terms, setpoint currents I_{td}^* and I_{tq}^* are computed to ensure the desired voltage is achieved at the VSC terminal. However, as indicated in (B.9) and (B.10), cross-terms such as $L\omega I_{tq}$ for I_d and $L\omega I_{td}$ for I_q can introduce interdependencies between the control schemes of the d- and q-axes. To address this, Figure B.7 presents a block diagram of a control scheme for the control plant depicted in Figure B.6, aiming to mitigate this dependency.

The inner control system comprises distinct d- and q-axis controllers. For the d-axis controller, a compensator $K_I(s)$ processes the error signal $e_d = I_{td}^* - I_{td}$, generating the control signal u_d . Subsequently, the desired value of the d-axis terminal voltage V_{td}^* is produced by incorporating two additional signals: $-I_{tq}\omega$ and V_{gd} into u_d . The signal $-I_{tq}\omega$ decouples I_{td} from I_{tq} , and the signal V_{gd} alleviates the dependency of I_{td} on V_{gd} , as shown in Figure B.6. The q-axis controller follows a similar strategy. Consequently, the injected currents at the VSC terminal precisely track their corresponding setpoints. These setpoints for the inner current controllers, I_{td}^* and I_{tq}^* , are defined by an additional controller referred to as the “outer controller”, which will be elaborated upon later.

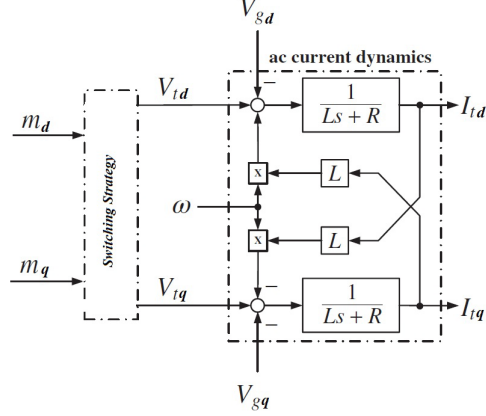


Figure B.6: Block diagram of the control plant describing the dynamics of the AC-side current in a dq-frame [104].

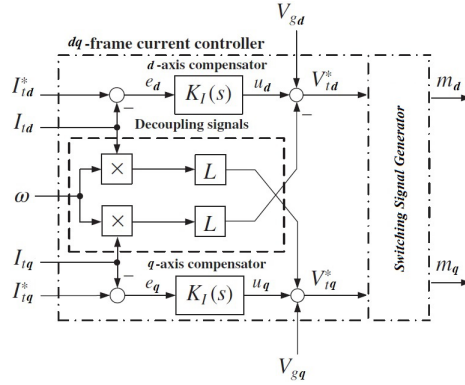


Figure B.7: Block diagram of the inner current controller for control plant of Figure B.6 [104].

It is important to note, as depicted in Figure B.5, that the control scheme in Figure B.7 applies to each sequence network individually. In the context of decoupled control on dq components in each sequence network and the control plant of Figure B.6, the entire current control process is depicted in Figure B.8. The overall setpoint currents in the d- and q-axes can be determined as follows

$$\begin{bmatrix} I_{td}^* \\ I_{tq}^* \end{bmatrix} = \begin{bmatrix} I_{td}^{p*} \\ I_{tq}^{p*} \end{bmatrix} + \begin{bmatrix} \cos(2\rho_r) & \sin(2\rho_r) \\ -\sin(2\rho_r) & \cos(2\rho_r) \end{bmatrix} \begin{bmatrix} I_{td}^{n*} \\ I_{tq}^{n*} \end{bmatrix} \quad (\text{B.11})$$

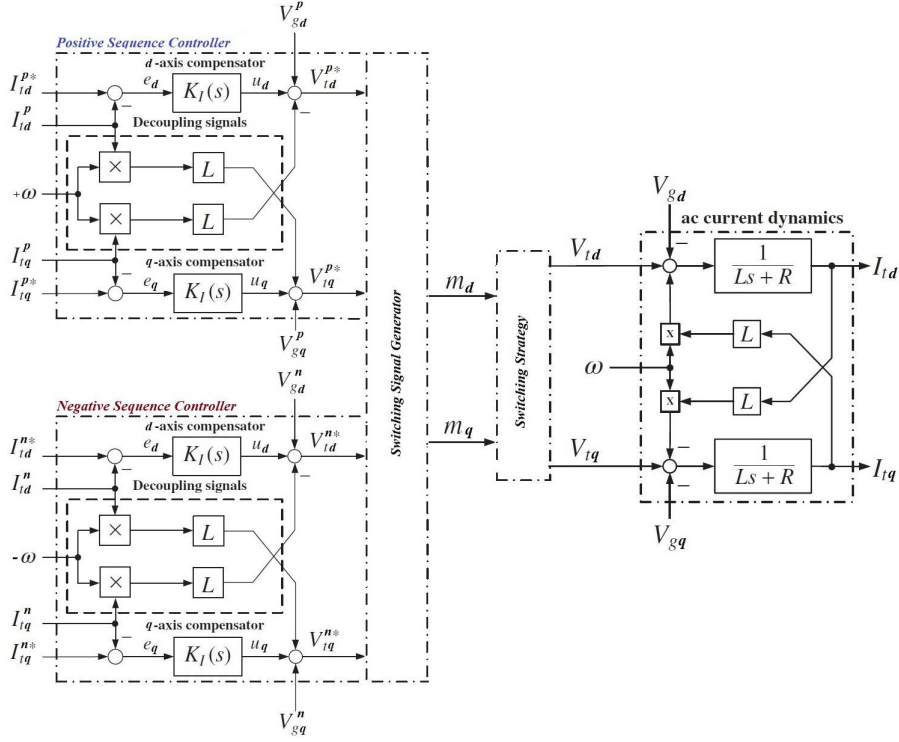


Figure B.8: The whole inner current control process in the dq-frame [106].

When examining the setpoints I_{td}^* and I_{tq}^* , it becomes evident that the control process resembles two distinct and independent control loops, as depicted in Figure B.9. One loop is dedicated to regulating I_{td} at the setpoint I_{td}^* , while the other loop focuses on adjusting I_{tq} at I_{tq}^* . Additionally, it can be inferred that the model of the control plant is analogous in both control loops. Consequently, the transfer function of the compensators will be identical, denoted as $K_I(s)$, as previously illustrated in Figure B.7.

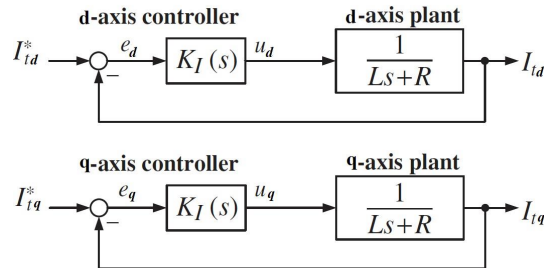


Figure B.9: Equivalent decoupled d- and q-axis current control loops [104].

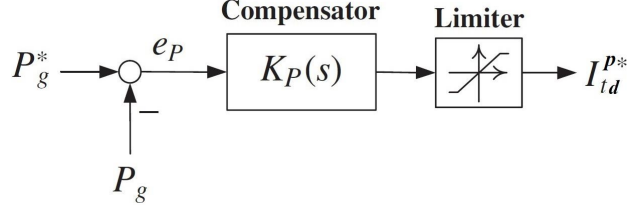


Figure B.10: Active power regulator [104].

B.5 Outer current control

The outer controller is in charge of regulating the setpoints of the inner current controllers, I_{td}^* and I_{tq}^* , under both steady-state and transient conditions. Several control strategies are available for implementation into the outer controller. Regardless of the chosen control schemes, maintaining the voltage of the DC link within an acceptable range requires at least one controller. However, it is pertinent to note that, in this investigation, our focus lies exclusively on the dynamics of RESs at the PCC, with no emphasis on the control loop for the DC link voltage.

Diverse control strategies are employed to regulate the system frequency and AC voltage level, achieved by appropriately setting the setpoints for active and reactive powers, respectively. The selection of control signals aligns with the pre-defined plans of system operators. Irrespective of the specific control strategies implemented, the setpoints are interpreted according to the current setpoints, I_{td}^* and I_{tq}^* . Ensuring the stability of the control system mandates that the time constants of the inner current controller be significantly smaller than those of the outer controller loops.

B.5.1 Positive sequence outer control in steady-state conditions

In the decoupled strategy for the d- and q-axes during steady-state conditions, the setpoint I_{td}^{p*} can be controlled through the active power supplied at the PCC, as illustrated in Figure B.10. Consequently, the active power from the RES, denoted as P_g , is adjusted to match the specified setpoint P_g^* . To address safety considerations, particularly in abnormal conditions, a limiter block is employed to ensure that the current setpoint remains within an acceptable range.

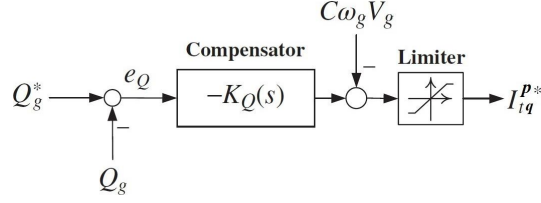


Figure B.11: Reactive power regulator [104].

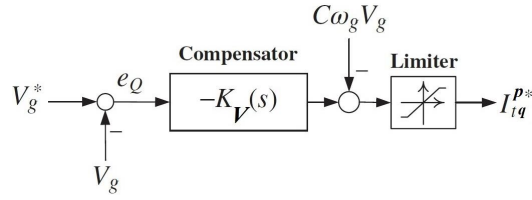


Figure B.12: AC voltage regulator [104].

As depicted in Figure B.11 and Figure B.12, the steady-state setpoint I_{tq}^{p*} can be controlled either through reactive power or grid voltage. This implies that, for load flow analyses in steady-state conditions, the PCC busbar can be treated as either a PQ or PV busbar, respectively. Consequently, the RES active power is adjusted to meet the specified setpoint Q_g^* , or the AC voltage at PCC is tuned to V_g^* . In these figures, the feed-forward signal $C\omega_g V_g$ serves to compensate for the reactive power generated by the capacitors in the AC filter in Figure B.1, denoted as Q_C , and the current limiter block ensures that I_{tq}^{p*} remains within an acceptable range.

B.5.2 Negative sequence outer control in steady-state conditions

During steady-state conditions, only the positive sequence current is desirable. In the absence of a predefined control strategy for the negative sequence current in a PE-based RES under steady-state conditions, the RES would essentially function as a short-circuited element in the negative sequence network. This scenario exposes the RES to potential damage, even in the case of slight unavoidable imbalances in the power system during normal operation. Consequently, to mitigate such risks, the set-points for negative sequence currents, I_{td}^{n*} and I_{tq}^{n*} , should be configured to zero during steady-state conditions.

B.5.3 Positive sequence outer control in transient conditions

After a contingency event, PE-based RESs are required to adhere to the stipulations outlined in grid codes. The LVRT profile specifies that the RES must remain connected to the grid and maintain stable operation in the event of a fault. The expected behaviour of RESs, generating positive sequence active and reactive power during transient conditions, is articulated in grid codes. Specifically, the current setpoints I_{td}^{p*} and I_{tq}^{p*} for transient conditions are determined based on steady-state setpoints and Grid Code regulations. Different countries follow various grid codes, such as the “GB Grid Code” and “Tennet Grid Code,” each tailored to specific engineering judgments and operational requirements.

As per the “GB Grid Code”, in the event of a contingency where the voltage drops by more than 10%, the RES should generate active power proportionally to the retained positive sequence voltage at the PCC. In this scenario, the RES is expected to supply the maximum permissible reactive current to produce as much reactive power as feasible.

According to the “Tennet Grid Code”, the reactive current is initially determined based on the voltage control characteristic depicted in Figure B.13. Subsequently, the active current is set according to the available current capacity of the RES, aiming to contribute as much active power as possible to the grid. Notably, a dead-band of 10% is established to prevent unwanted control operations. Consequently, PE-based RESs should be capable of injecting a minimum of 1.0 pu reactive current when the voltage falls below 50%.

B.5.4 Negative sequence outer control in transient conditions

During transient conditions, where negative sequence currents and voltages are present in the system, the expressions for active and reactive powers encompass a constant term along with two sinusoidal components at a frequency of 2ω , as below

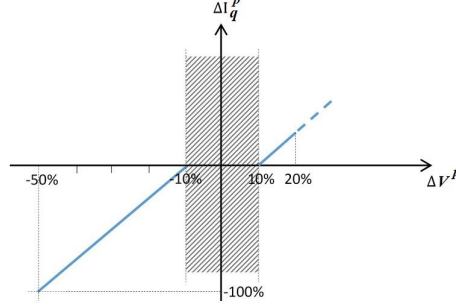


Figure B.13: Increment of the reactive current defined by the Tennet Grid Code [93].

$$P = P0 + P1 * \cos(2\omega t) + P2 * \sin(2\omega t) \quad (\text{B.12})$$

$$Q = Q0 + Q1 * \cos(2\omega t) + Q2 * \sin(2\omega t) \quad (\text{B.13})$$

The components of active and reactive powers, denoted as $P0, P1, P2, Q0, Q1, Q2$, can be expressed in the dq-frame by utilising positive and negative sequence voltages and currents in the following manner [107]

$$\begin{bmatrix} P0 \\ Q0 \\ P1 \\ P2 \\ Q1 \\ Q2 \end{bmatrix} = \frac{3}{2} \begin{bmatrix} V_d^P & V_q^P & V_d^n & V_q^n \\ V_q^P & -V_d^P & V_q^n & -V_d^n \\ V_d^n & V_q^n & V_d^P & V_q^P \\ V_q^n & -V_d^n & -V_q^P & V_d^P \\ V_q^P & -V_d^P & V_q^n & -V_d^n \\ -V_d^n & -V_q^n & V_d^P & V_q^P \end{bmatrix} \begin{bmatrix} I_d^P \\ I_q^P \\ I_d^n \\ I_q^n \end{bmatrix} \quad (\text{B.14})$$

This set of equations involves four current variables, yet the right-hand side encompasses six terms. This implies that all six power terms can be regulated through these four current variables. In steady-state conditions or symmetrical faults, the negative sequence components vanish, and the sinusoidal terms only manifest in the presence of negative sequence voltages and currents in the system. During asymmetrical transient conditions, the negative sequence components exert a significant influence on the overall active and reactive powers.

By the time of writing this thesis, the GB and Tennet grid codes solely prescribe regulations for the positive sequence active and reactive power of PE-based RESs [54, 93].

This means that modifications for transient conditions are limited to the current setpoints I_{td}^{p*} and I_{tq}^{p*} . In the absence of a predetermined control strategy for the negative sequence current in a PE-based RES during unbalanced faults, the RES would act as a short-circuited element in the negative sequence network, exposing it to considerable damage. However, significant benefits can be realised by controlling negative sequence current setpoints, I_{td}^{n*} and I_{tq}^{n*} . Various strategies can be employed to establish a more sophisticated control of active and reactive powers, and some of these are outlined below.

B.6 Suppress negative sequence current

A straightforward approach to controlling negative sequence current involves its suppression. While the positive sequence setpoints, I_{td}^{p*} and I_{tq}^{p*} , are adjusted in accordance with the Grid Code, the corresponding negative sequence setpoints, I_{td}^{n*} and I_{tq}^{n*} , are set to zero. Consequently, only the positive sequence current is injected during both symmetrical and asymmetrical faults. This strategy, for instance, aligns with the Tennet Grid Code, where, following the determination of the appropriate reactive current based on the voltage drop in Figure B.13, the RES utilises its remaining current capacity to deliver maximum active power to the grid.

B.7 Imitate synchronous machine behaviour in the negative sequence

When the negative sequence current is configured in proportion to the negative sequence voltage, the behaviour of the RES mimics that of a synchronous machine within the negative sequence network during a fault. Consequently, in equations (B.12) and (B.13), distinct constant power terms for the negative sequence network can be discerned. As a result of the independence between positive sequence voltages and currents and negative sequence counterparts, the constant terms of active and reactive power (P_0 and Q_0) can be decomposed into two components, as outlined below

$$P_0 = P_0^p + P_0^n \quad (\text{B.15})$$

$$Q_0 = Q_0^p + Q_0^n \quad (\text{B.16})$$

According to (B.14) to (B.16), the following equation can be derived

$$\begin{bmatrix} P_0^p \\ Q_0^p \\ P_0^n \\ Q_0^n \end{bmatrix} = \frac{3}{2} \begin{bmatrix} V_d^p & V_q^p & 0 & 0 \\ V_q^p & -V_d^p & 0 & 0 \\ 0 & 0 & V_d^n & V_q^n \\ 0 & 0 & V_q^n & -V_d^n \end{bmatrix} \begin{bmatrix} I_d^p \\ I_q^p \\ I_d^n \\ I_q^n \end{bmatrix} \quad (\text{B.17})$$

Finally, negative sequence setpoint currents can be calculated as

$$\begin{bmatrix} I_d^n \\ I_q^n \end{bmatrix} = \frac{2}{3} \begin{bmatrix} V_d^n & V_q^n \\ V_q^n & -V_d^n \end{bmatrix}^{-1} \begin{bmatrix} P_0^n \\ Q_0^n \end{bmatrix} \quad (\text{B.18})$$

The power terms P_0^n and Q_0^n need to be determined in a manner that results in a constant complex number, such as impedance denoted by Z^n , which signifies the relationship between I^n and V^n in the following manner

$$V^n = Z^n I^n \quad (\text{B.19})$$

To achieve this, the following methodology is employed

- The negative sequence impedance is represented in its polar form as $|K|\angle\theta$. Consequently, the selection of K and θ becomes crucial as control setpoints.
- The negative sequence dq-frame voltage, denoted as V_d^n and V_q^n , is computed according to the illustration in Figure B.5. Subsequently, the magnitude of the negative sequence voltage, $|V^n|$, is determined by $\sqrt{V_d^{n2} + V_q^{n2}}$.
- The magnitude of the negative sequence current, $|I^n|$, is calculated using K and $|V^n|$ in equation (B.19).
- Once $|I^n|$ and $|V^n|$ are determined, the apparent power of the negative sequence network, $|S^n|$, can be readily computed. Subsequently, the negative sequence active and reactive power, P_0^n and Q_0^n , are obtained as follows

$$\begin{cases} P_0^n = |S^n| \cos(\theta) \\ Q_0^n = |S^n| \sin(\theta) \end{cases} \quad (\text{B.20})$$

It is important to emphasize that the magnitude $|I^n|$ is constrained by the maximum negative sequence current capacity of the RES, a parameter set by the operator. Consequently, the linear relationship between V^n and I^n , wherein the RES emulates synchronous machine behaviour based on the value of K , is applicable only within a restricted range of V^n .

B.8 RES model in DIgSILENT PowerFactory

Diverse control strategies for RESs, addressing both positive and negative sequences, have been simulated using the DSL tools available in DIgSILENT PowerFactory software. The complete control model is depicted in Figure B.14, encompassing the following components [106]

- **Measurement:** In this module, the time domain values of RES terminal voltage, grid voltage, and RES terminal current undergo decomposition into real and imaginary components in the stationary frame $\alpha\beta$ via Clark transformation. Additionally, Phase Locked Loop (PLL) blocks compute the values of $\sin(\rho_r(t))$ and $\cos(\rho_r(t))$ in (B.3).
- **Positive/Negative Decomposition:** Within this module, the current and voltage waveforms in the stationary frame $\alpha\beta$ are decomposed into positive and negative sequence components, as depicted in Figure B.4.
- **$\alpha\beta$ to dq Transformation:** This module involves the calculation of d- and q-axis components of currents and voltages using (B.3) and (B.4) alongside PLL signals ($\sin(\rho_r(t))$ and $\cos(\rho_r(t))$), illustrated in Figure B.5.
- **P/Q Calculation:** Active and reactive power for the RES in positive and negative sequence networks are computed separately in this part. These signals play a role in the control loops for steady-state conditions, as illustrated in Figure B.10 and Figure B.11.

- **Fault Detection:** Here, the system detects transient (fault) conditions by monitoring the positive sequence voltage of the grid. For instance, following the GB Grid Code, the RES control system transitions into transient control mode when the positive sequence voltage drops more than 10%.
- **Frequency Excursion Detection:** This section involves the identification of low-frequency excursions by monitoring local frequencies. As per the GB Grid Code, if the local frequency falls up to 0.2 Hz from the nominal value, an under-frequency excursion is detected, leading to the deployment of up to 5% of fast-acting resources for frequency support. Complete activation of fast-acting resources occurs if the frequency drops below 0.2 Hz up to 0.5 Hz from the nominal value.
- **Outer Controller:** Implementing the control schemes described in section B.5, this section comprises the outer controller determining current setpoints for the inner controller based on both steady-state and transient conditions. Figure B.15 provides a detailed diagram of the DSL-built outer controller.
- **Inner Controller:** Application of the inner control loops for the RES control system occurs in this part, following the control diagram presented in Figure B.8 and Figure B.9.
- **Static Generator:** In this project, focusing on the behaviour of RESs during under-frequency excursion conditions for power system protection, the internal control mechanisms of switching devices are not investigated due to their significantly shorter response times (e.g., a few microseconds) compared to the time-scales relevant for FFC schemes (e.g., a few power frequency cycles). From the perspective of FFC applications, an RES can be modelled as a static generator in DIgSILENT PowerFactory, capable of adjusting its active and reactive power contributions to the grid. The dynamics of internal components of the RES, such as the DC link and rectifier converter, are disregarded.

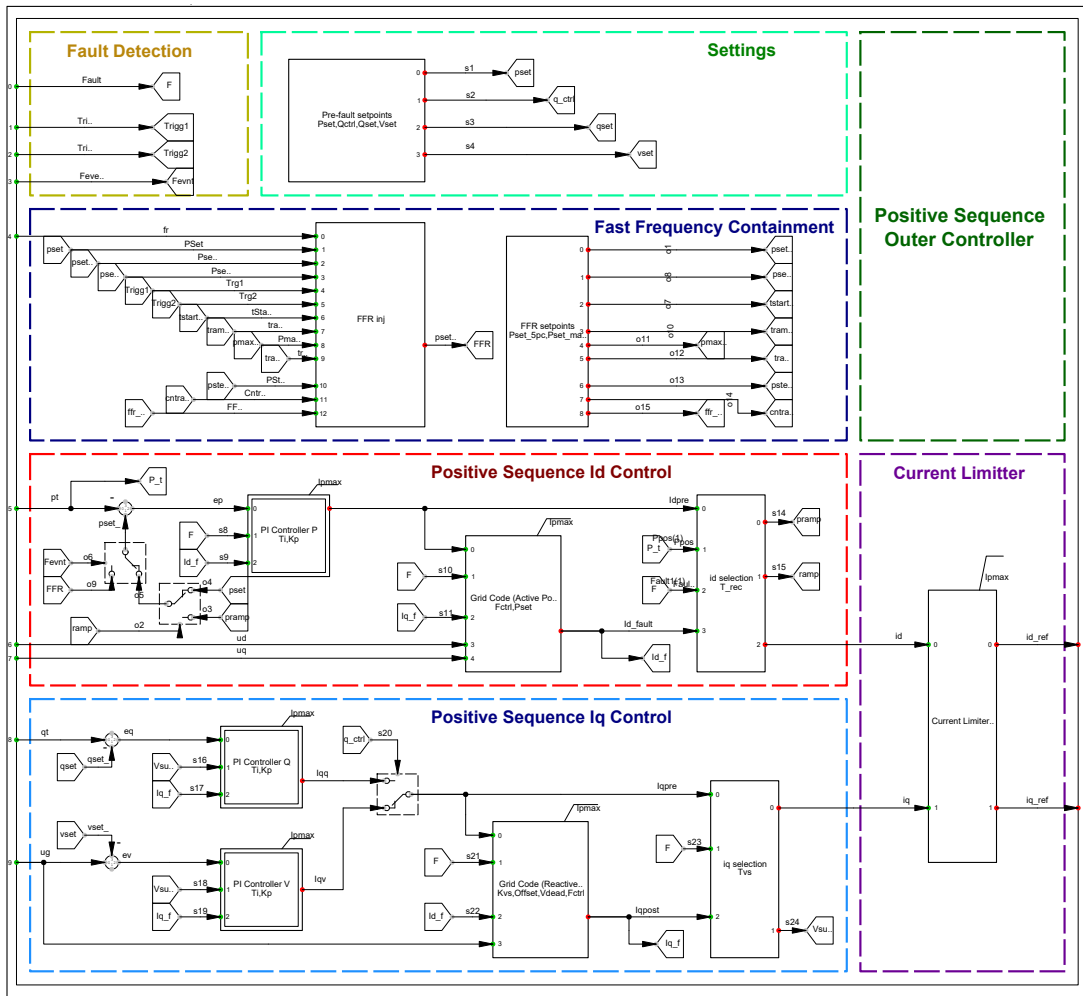


Figure B.15: Positive sequence outer controller (Modified from [106]).

BIBLIOGRAPHY

- [1] H. Kirkham, W. Dickerson, and A. Phadke, “Defining power system frequency,” in *2018 IEEE Power Energy Society General Meeting (PESGM)*, 2018, pp. 1–5.
- [2] P. Kundur, J. Paserba, V. Ajjarapu, G. Andersson, A. Bose, C. Canizares, N. Hatziaargyriou, D. Hill, A. Stankovic, C. Taylor, T. Van Cutsem, and V. Vittal, “Definition and classification of power system stability ieeecigre joint task force on stability terms and definitions,” *IEEE Transactions on Power Systems*, vol. 19, no. 3, pp. 1387–1401, 2004.
- [3] O. Elgerd, “Control of electric power systems,” *IEEE Control Systems Magazine*, vol. 1, no. 2, pp. 4–16, 1981.
- [4] A. Gomez-Exposito, A. J. Conejo, and C. Cañizares, *Electric energy systems: analysis and operation*. CRC press, 2018.
- [5] F. Milano, F. Dörfler, G. Hug, D. J. Hill, and G. VerbiÄ, “Foundations and challenges of low-inertia systems (invited paper),” in *2018 Power Systems Computation Conference (PSCC)*, 2018, pp. 1–25.
- [6] D. Zografos and M. Ghandhari, “Power system inertia estimation by approaching load power change after a disturbance,” in *2017 IEEE Power & Energy Society General Meeting*. IEEE, 2017, pp. 1–5.
- [7] N. G. ESO, “The enhanced frequency control capability (EFCC) project, closing down report,” 2019.
- [8] MIGRATE, “Development and tests of new protection solutions when reaching 100pe penetration,” Dec 2018.

- [9] P. Kundur, *Power System Stability and Control*. McGraw-Hill, 1994.
- [10] ENTSO-E, “Future system inertia,” Feb 2018.
- [11] Y. Zhang, P. Markham, T. Xia, L. Chen, Y. Ye, Z. Wu, Z. Yuan, L. Wang, J. Bank, J. Burgett *et al.*, “Wide-area frequency monitoring network (fnet) architecture and applications,” *IEEE Transactions on smart grid*, vol. 1, no. 2, pp. 159–167, 2010.
- [12] P. M. Anderson, *Power system protection*. John Wiley & Sons IEEE Press, 1999.
- [13] V. V. Terzija, “Adaptive underfrequency load shedding based on the magnitude of the disturbance estimation,” *IEEE Transactions on Power Systems*, vol. 21, no. 3, pp. 1260–1266, 2006.
- [14] P. Tielens and D. Van Hertem, “The relevance of inertia in power systems,” *Renewable and sustainable energy reviews*, vol. 55, pp. 999–1009, 2016.
- [15] M. Sun, G. Liu, M. Popov, V. Terzija, and S. Azizi, “Underfrequency load shedding using locally estimated rocof of the center of inertia,” *IEEE Transactions on Power Systems*, vol. 36, no. 5, pp. 4212–4222, 2021.
- [16] J. Dong, J. Zuo, L. Wang, K. S. Kook, I.-Y. Chung, Y. Liu, S. Affare, B. Rogers, and M. Ingram, “Analysis of power system disturbances based on wide-area frequency measurements,” in *2007 IEEE Power Engineering Society General Meeting*. IEEE, 2007, pp. 1–8.
- [17] A. Bykhovsky and J. H. Chow, “Power system disturbance identification from recorded dynamic data at the northfield substation,” *International journal of electrical power & energy systems*, vol. 25, no. 10, pp. 787–795, 2003.
- [18] J. Bank *et al.*, “Generator trip identification using wide-area measurements and historical data analysis, psce 2006,” 2006.
- [19] W. Li, J. Tang, J. Ma, and Y. Liu, “Online detection of start time and location for hypocenter in north america power grid,” *IEEE Transactions on Smart Grid*, vol. 1, no. 3, pp. 253–260, 2010.

- [20] K. Mei, S. M. Rovnyak, and C.-M. Ong, "Clustering-based dynamic event location using wide-area phasor measurements," *IEEE Transactions on Power Systems*, vol. 23, no. 2, pp. 673–679, 2008.
- [21] J. S. Thorp, C. E. Seyler, and A. G. Phadke, "Electromechanical wave propagation in large electric power systems," *IEEE Transactions on Circuits and Systems I: Fundamental Theory and Applications*, vol. 45, no. 6, pp. 614–622, 1998.
- [22] T. Xia, H. Zhang, R. Gardner, J. Bank, J. Dong, J. Zuo, Y. Liu, L. Beard, P. Hirsch, G. Zhang *et al.*, "Wide-area frequency based event location estimation," in *2007 IEEE Power Engineering Society General Meeting*. IEEE, 2007, pp. 1–7.
- [23] G. Zheng, Y. Liu, and G. Radman, "Wide area frequency based generation trip event location estimation," in *2012 IEEE Power and Energy Society General Meeting*. IEEE, 2012, pp. 1–6.
- [24] W.-T. Li, C.-K. Wen, J.-C. Chen, K.-K. Wong, J.-H. Teng, and C. Yuen, "Location identification of power line outages using pmu measurements with bad data," *IEEE Transactions on Power Systems*, vol. 31, no. 5, pp. 3624–3635, 2015.
- [25] G. Frigo, A. Derviškadić, Y. Zuo, and M. Paolone, "Pmu-based rocof measurements: Uncertainty limits and metrological significance in power system applications," *IEEE Transactions on Instrumentation and Measurement*, vol. 68, no. 10, pp. 3810–3822, 2019.
- [26] U. Rudez and R. Mihalic, "Analysis of underfrequency load shedding using a frequency gradient," *IEEE transactions on power delivery*, vol. 26, no. 2, pp. 565–575, 2009.
- [27] H. Zhang, F. Shi, Y. Liu, and V. Terzija, "Adaptive online disturbance location considering anisotropy of frequency propagation speeds," *IEEE Transactions on Power Systems*, vol. 31, no. 2, pp. 931–941, 2015.
- [28] D.-I. Kim, A. White, and Y.-J. Shin, "Pmu-based event localization technique for wide-area power system," *IEEE Transactions on Power Systems*, vol. 33, no. 6, pp. 5875–5883, 2018.

- [29] S. M. Rovnyak and K. Mei, “Dynamic event detection and location using wide area phasor measurements,” *European Transactions on Electrical Power*, vol. 21, no. 4, pp. 1589–1599, 2011.
- [30] R. Azizipanah-Abarghooee, M. Malekpour, M. Paolone, and V. Terzija, “A new approach to the online estimation of the loss of generation size in power systems,” *IEEE Transactions on Power Systems*, vol. 34, no. 3, pp. 2103–2113, 2018.
- [31] N. Shams, P. Wall, and V. Terzija, “Active power imbalance detection, size and location estimation using limited pmu measurements,” *IEEE Transactions on Power Systems*, vol. 34, no. 2, pp. 1362–1372, 2018.
- [32] S. Azizi, M. R. Jegarluei, A. S. Dobakhshari, G. Liu, and V. Terzija, “Wide-area identification of the size and location of loss of generation events by sparse pmus,” *IEEE Transactions on Power Delivery*, vol. 36, no. 4, pp. 2397–2407, 2020.
- [33] G. G. Solutions, “Enhanced frequency control capability (EFCC), optimisation detailed design,” Jan 2016. [Online]. Available: <https://www.nationalgrideso.com/document/135981/download>
- [34] Y. Cheng, R. Azizipanah-Abarghooee, S. Azizi, L. Ding, and V. Terzija, “Smart frequency control in low inertia energy systems based on frequency response techniques: A review,” *Applied Energy*, vol. 279, p. 115798, 2020.
- [35] W. He, X. Yuan, and J. Hu, “Inertia provision and estimation of PLL-based dfig wind turbines,” *IEEE Transactions on power systems*, vol. 32, no. 1, pp. 510–521, 2016.
- [36] L. Harnefors, M. Schweizer, J. Kukkola, M. Routimo, M. Hinkkanen, and X. Wang, “Generic PLL-based grid-forming control,” *IEEE Transactions on Power Electronics*, vol. 37, no. 2, pp. 1201–1204, 2021.
- [37] X. Guo, D. Zhu, J. Hu, X. Zou, Y. Kang, and J. M. Guerrero, “Inertial PLL of grid-connected converter for fast frequency support,” *CSEE Journal of Power and Energy Systems*, 2022.
- [38] C. Zhang, E. Rakhshani, N. Veerakumar, J. L. R. Torres, and P. Palensky, “Modeling and optimal tuning of hybrid ESS supporting fast active power regulation of

- fully decoupled wind power generators,” *IEEE Access*, vol. 9, pp. 46 409–46 421, 2021.
- [39] J. Lee, S. Jeong, H. Kim, Y. Yoo, S. Jung, M. Yoon, and G. Jang, “Analytical approach for fast frequency response control of VSC HVDC,” *IEEE Access*, vol. 9, pp. 91 303–91 313, 2021.
- [40] M. Kabsha and Z. H. Rather, “A new control scheme for fast frequency support from HVDC connected offshore wind farm in low-inertia system,” *IEEE Transactions on Sustainable Energy*, vol. 11, no. 3, pp. 1829–1837, 2019.
- [41] K. Jose, O. Adeuyi, J. Liang, and C. E. Ugalde-Loo, “Coordination of fast frequency support from multi-terminal HVDC grids,” in *2018 IEEE international energy conference (ENERGYCON)*. IEEE, 2018, pp. 1–6.
- [42] O. Stanojev, U. Markovic, E. Vrettos, P. Aristidou, D. Callaway, and G. Hug, “Enhanced MPC for fast frequency control in inverter-dominated power systems,” in *2020 International Conference on Smart Energy Systems and Technologies (SEST)*. IEEE, 2020, pp. 1–6.
- [43] D. Yang, L. Hua, and X. Zhang, “Fast frequency support of a DFIG based on over-speed de-loaded curve,” in *2021 IEEE/IAS Industrial and Commercial Power System Asia (I&CPS Asia)*. IEEE, 2021, pp. 1314–1318.
- [44] M. Kheshti, S. Lin, X. Zhao, L. Ding, M. Yin, and V. Terzija, “Gaussian distribution-based inertial control of wind turbine generators for fast frequency response in low inertia systems,” *IEEE Transactions on Sustainable Energy*, vol. 13, no. 3, pp. 1641–1653, 2022.
- [45] X. Zhao, Y. Xue, and X.-P. Zhang, “Fast frequency support from wind turbine systems by arresting frequency nadir close to settling frequency,” *IEEE Open Access Journal of Power and Energy*, vol. 7, pp. 191–202, 2020.
- [46] G. Xu, L. Xu, and J. Morrow, “System frequency support using wind turbine kinetic energy and energy storage system,” in *2nd IET Renewable Power Generation Conference (RPG 2013)*. IET, 2013.
- [47] K. Sun, K.-J. Li, W. Bao, Z. Liu, M. Wang, W.-J. Lee *et al.*, “Frequency compensation control strategy of energy storage in the wind-energy storage hybrid

- system for improving frequency response performance,” in *2019 IEEE Industry Applications Society Annual Meeting*. IEEE, 2019, pp. 1–8.
- [48] W. Liu, G. Geng, Q. Jiang, H. Fan, and J. Yu, “Model-free fast frequency control support with energy storage system,” *IEEE Transactions on Power Systems*, vol. 35, no. 4, pp. 3078–3086, 2019.
- [49] Y. Yoo, S. Jung, and G. Jang, “Dynamic inertia response support by energy storage system with renewable energy integration substation,” *Journal of Modern Power Systems and Clean Energy*, vol. 8, no. 2, pp. 260–266, 2019.
- [50] W. Bao, L. Ding, Z. Liu, G. Zhu, M. Kheshti, Q. Wu, and V. Terzija, “Analytically derived fixed termination time for stepwise inertial control of wind turbines-part i: Analytical derivation,” *International Journal of Electrical Power & Energy Systems*, vol. 121, p. 106120, 2020.
- [51] Y. Guo, W. Bao, L. Ding, Z. Liu, M. Kheshti, Q. Wu, and V. Terzija, “Analytically derived fixed termination time for stepwise inertial control of wind turbines-part ii: Application strategy,” *International Journal of Electrical Power & Energy Systems*, vol. 121, p. 106106, 2020.
- [52] P. Anderson and M. Mirheydar, “A low-order system frequency response model,” *IEEE Transactions on Power Systems*, vol. 5, no. 3, pp. 720–729, 1990.
- [53] N. G. ESO, “Dynamic containment response balancing service, test guidance for providers,” Jun 2022.
- [54] —, *The grid code, Issue 6, Revision 16*. Great Britain, 2023.
- [55] J. J. Grainger and W. D. Stevenson Jr, *Power system analysis*. McGraw-Hill series in electrical and computer engineering, 1994.
- [56] W. C. New and W. C. New, *Load shedding, load restoration and generator protection using solid-state and electromechanical underfrequency relays*. General Electric Company, Power Systems Management, 1974.
- [57] J. D. Glover, M. S. Sarma, and T. Overbye, *Power system analysis & design, SI version*. Cengage Learning, 2012.

- [58] A. Ulbig, T. S. Borsche, and G. Andersson, “Impact of low rotational inertia on power system stability and operation,” *IFAC Proceedings Volumes*, vol. 47, no. 3, pp. 7290–7297, 2014.
- [59] U. Rudez and R. Mihalic, “Wams-based underfrequency load shedding with short-term frequency prediction,” *IEEE Transactions on Power Delivery*, vol. 31, no. 4, pp. 1912–1920, 2015.
- [60] S. Azizi, M. Sun, G. Liu, and V. Terzija, “Local frequency-based estimation of the rate of change of frequency of the center of inertia,” *IEEE Transactions on Power Systems*, vol. 35, no. 6, pp. 4948–4951, 2020.
- [61] J. S. Cortés and D. R. Romero, “Esquemas dinámicos de tiro de carga por baja frecuencia mediante lógica difusa,” in *27 Reunión Internacional de Verano de Potencia, Aplicaciones Industriales y Exposición Industrial (RVP-AI)*. IEEE, 2014, pp. 1–8 SIS–17, PON–89.
- [62] P. Warren, “A review of demand-side management policy in the UK,” *Renewable and Sustainable Energy Reviews*, vol. 29, pp. 941–951, 2014.
- [63] H. Bevrani, *Robust power system frequency control*. Springer, 2014, vol. 4.
- [64] A. J. Wood, B. F. Wollenberg, and G. B. Sheblé, *Power generation, operation, and control*. John Wiley & Sons, 2013.
- [65] C. Rowland, D. Smaha, and J. Pope, “Coordination of load conservation with turbine-generator underfrequency protection,” *IEEE Transactions on Power Apparatus and Systems*, no. 3, pp. 1137–1150, 1980.
- [66] Y. Omar, I. Abidin, S. Yusof, H. Hashim, and H. A. Rashid, “Under frequency load shedding (ufls): Principles and implementation,” in *2010 IEEE International Conference on Power and Energy*. IEEE, 2010, pp. 414–419.
- [67] J. Sánchez Cortés, “Diseño de esquemas de tiro de carga por baja frecuencia utilizando técnicas inteligentes,” *MSc thesis*, 2014.
- [68] M. Abedini, M. Sanaye-Pasand, and S. Azizi, “Adaptive load shedding scheme to preserve the power system stability following large disturbances,” *IET Generation, Transmission & Distribution*, vol. 8, no. 12, pp. 2124–2133, 2014.

- [69] RielloUPS, “The blackout report: what happens when there is no power?” 2019.
- [70] T. S. Borsche, T. Liu, and D. J. Hill, “Effects of rotational inertia on power system damping and frequency transients,” in *2015 54th IEEE conference on decision and control (CDC)*. IEEE, 2015, pp. 5940–5946.
- [71] I. P. P. S. R. Committee *et al.*, “Ieee guide for abnormal frequency protection for power generating plants,” *IEEE Std C37. 106-2003 (Revision of ANSI/IEEE C37. 106-1987)*, pp. 0.1–34, 2004.
- [72] J. Berdy, P. Brown, and L. Goff, “Protection of steam turbine generators during abnormal frequency conditions,” *General Electric Company, Schenectady, New York*, 1974.
- [73] R. Warner, T. Dillman, and M. Baldwin, “Off-frequency turbine-generator unit operation,” in *Proc. Am. Power Conf.:(United States)*, vol. 38, 1976.
- [74] P. K. Pathak and A. R. Gupta, “Battery energy storage system,” in *2018 4th International Conference on Computational Intelligence & Communication Technology (CICT)*. IEEE, 2018, pp. 1–9.
- [75] M. Kheshti, L. Ding, W. Bao, M. Yin, Q. Wu, and V. Terzija, “Toward intelligent inertial frequency participation of wind farms for the grid frequency control,” *IEEE Transactions on Industrial Informatics*, vol. 16, no. 11, pp. 6772–6786, 2019.
- [76] L. Ruttledge, N. W. Miller, J. O’Sullivan, and D. Flynn, “Frequency response of power systems with variable speed wind turbines,” *IEEE transactions on Sustainable Energy*, vol. 3, no. 4, pp. 683–691, 2012.
- [77] M. Garmroodi, G. Verbič, and D. J. Hill, “Frequency support from wind turbine generators with a time-variable droop characteristic,” *IEEE Transactions on Sustainable Energy*, vol. 9, no. 2, pp. 676–684, 2017.
- [78] F. Díaz-González, M. Hau, A. Sumper, and O. Gomis-Bellmunt, “Participation of wind power plants in system frequency control: Review of grid code requirements and control methods,” *Renewable and Sustainable Energy Reviews*, vol. 34, pp. 551–564, 2014.

- [79] J. Van de Vyver, J. D. De Kooning, B. Meersman, L. Vandeveldel, and T. L. Vandoorn, “Droop control as an alternative inertial response strategy for the synthetic inertia on wind turbines,” *IEEE Transactions on Power Systems*, vol. 31, no. 2, pp. 1129–1138, 2015.
- [80] X. Zhang, X. Zha, S. Yue, and Y. Chen, “A frequency regulation strategy for wind power based on limited over-speed de-loading curve partitioning,” *IEEE Access*, vol. 6, pp. 22 938–22 951, 2018.
- [81] W. Bao, Q. Wu, L. Ding, S. Huang, F. Teng, and V. Terzija, “Synthetic inertial control of wind farm with bess based on model predictive control,” *IET Renewable Power Generation*, vol. 14, no. 13, pp. 2447–2455, 2020.
- [82] M. Dreidy, H. Mokhlis, and S. Mekhilef, “Inertia response and frequency control techniques for renewable energy sources: A review,” *Renewable and sustainable energy reviews*, vol. 69, pp. 144–155, 2017.
- [83] C. Rahmann, J. Jara, and M. Salles, “Effects of inertia emulation in modern wind parks on isolated power systems,” in *2015 IEEE Power & Energy Society General Meeting*. IEEE, 2015, pp. 1–5.
- [84] W. Bao, L. Ding, S. Yin, K. Wang, and V. Terzija, “Active rotor speed protection for dfig synthetic inertia control,” 2016.
- [85] R. Eriksson, N. Modig, and K. Elkington, “Synthetic inertia versus fast frequency response: a definition,” *IET renewable power generation*, vol. 12, no. 5, pp. 507–514, 2018.
- [86] U. Energy, “Pathways for the gb electricity sector to 2030,” *Full Report*, 2016.
- [87] N. Mendis, K. M. Muttaqi, and S. Perera, “Management of battery-supercapacitor hybrid energy storage and synchronous condenser for isolated operation of pmsg based variable-speed wind turbine generating systems,” *IEEE Transactions on smart grid*, vol. 5, no. 2, pp. 944–953, 2014.
- [88] S. Azizi and M. Sanaye-Pasand, “From available synchrophasor data to short-circuit fault identity: Formulation and feasibility analysis,” *IEEE Transactions on Power Systems*, vol. 32, no. 3, pp. 2062–2071, 2016.

- [89] K. Jia, Z. Yang, Y. Fang, T. Bi, and M. Sumner, “Influence of inverter-interfaced renewable energy generators on directional relay and an improved scheme,” *IEEE Transactions on Power Electronics*, vol. 34, no. 12, pp. 11 843–11 855, 2019.
- [90] J. S. Cortés, M. R. Jegarluei, P. Aristidou, K. Li, and S. Azizi, “Size/location estimation for loss of generation events in power systems with high penetration of renewables,” *Electric Power Systems Research*, vol. 219, p. 109242, 2023.
- [91] A. S. Dobakhshari, S. Azizi, M. Paolone, and V. Terzija, “Ultra fast linear state estimation utilizing scada measurements,” *IEEE Transactions on Power Systems*, vol. 34, no. 4, pp. 2622–2631, 2019.
- [92] C. D. Meyer, *Matrix analysis and applied linear algebra*. SIAM, 2000.
- [93] T. T. GmbH, *Grid code-High and extra high voltage*, 2017.
- [94] R. D. Zimmerman, C. E. Murillo-Sánchez, and D. Gan, *MATPOWER: A MATLAB power system simulation package*. Manual, Power Systems Engineering Research Center, Ithaca NY, 2007, vol. 3.2.
- [95] S. Azizi, A. S. Dobakhshari, S. A. N. Sarmadi, and A. M. Ranjbar, “Optimal PMU placement by an equivalent linear formulation for exhaustive search,” *IEEE Transactions on Smart Grid*, vol. 3, no. 1, pp. 174–182, 2012.
- [96] S. M. for Power Systems Working Group *et al.*, “IEEE standard for synchrophasor measurements for power systems,” *IEEE Std C*, vol. 37, pp. 1–61.
- [97] A. Abur and A. G. Exposito, *Power system state estimation: theory and implementation*. CRC press, 2004.
- [98] S. Sarri, M. Pignati, P. Romano, L. Zanni, and M. Paolone, “A hardware-in-the-loop test platform for the performance assessment of a PMU-based real-time state estimator for active distribution networks,” in *2015 IEEE Eindhoven PowerTech*. IEEE, 2015, pp. 1–6.
- [99] A. G. Phadke and J. S. Thorp, *Computer relaying for power systems*. John Wiley & Sons, 2009.

- [100] F. C. Schweppe and J. Wildes, “Power system static-state estimation, part I: Exact model,” *IEEE Transactions on Power Apparatus and Systems*, vol. PAS-89, no. 1, pp. 120–125, 1970.
- [101] J. Sánchez Cortés, M. Rezaei Jegarluei, and S. Azizi, “Targeted fast frequency response by decomposing frequency into transient and steady-state deviations,” in *2023 International Conference on Energy Technologies for Future Grids (ETFEG)*. IEEE, 2023.
- [102] R. Bracewell, *The Fourier transform and its applications*. McGraw-Hill, 1986.
- [103] A. Aksoy and M. Martelli, “Mixed partial derivatives and Fubini’s theorem,” *The College Mathematics Journal*, vol. 33, no. 2, pp. 126–130, 2002.
- [104] N. Chaudhuri, B. Chaudhuri, R. Majumder, and A. Yazdani, *Multi-terminal direct-current grids: Modeling, analysis, and control*. John Wiley & Sons, 2014.
- [105] P. Rodríguez, J. Pou, J. Bergas, J. I. Candela, R. P. Burgos, and D. Boroyevich, “Decoupled double synchronous reference frame PLL for power converters control,” *IEEE Transactions on Power Electronics*, vol. 22, no. 2, pp. 584–592, 2007.
- [106] M. R. Jegarluei, P. Aristidou, and S. Azizi, “Wide-area backup protection against asymmetrical faults in the presence of renewable energy sources,” *International Journal of Electrical Power & Energy Systems*, vol. 144, p. 108528, 2023.
- [107] K. Ma, W. Chen, M. Liserre, and F. Blaabjerg, “Power controllability of a three-phase converter with an unbalanced ac source,” *IEEE Transactions on Power Electronics*, vol. 30, no. 3, pp. 1591–1604, 2014.